

CONTROLLING DEFECTS IN NEMATIC AND SMECTIC LIQUID CRYSTALS
THROUGH BOUNDARY GEOMETRY

Daniel A. Beller

A DISSERTATION

in

Physics and Astronomy

Presented to the Faculties of the University of Pennsylvania

in

Partial Fulfillment of the Requirements for the

Degree of Doctor of Philosophy

2014

Supervisor of Dissertation

Randall D. Kamien

Professor of Physics and Astronomy

Graduate Group Chairperson

Randall D. Kamien, Professor of Physics and Astronomy

Dissertation Committee

Tom C. Lubensky, Professor of Physics and Astronomy

Kathleen J. Stebe, Professor of Chemical and Biomolecular Engineering

Alison M. Sweeney, Assistant Professor of Physics and Astronomy

Shu Yang, Professor of Materials Science and Engineering

CONTROLLING DEFECTS IN NEMATIC AND SMECTIC LIQUID CRYSTALS
THROUGH BOUNDARY GEOMETRY

COPYRIGHT

2014

Daniel Aaron Beller

Dedication

In memory of my grandfather, Bernard Korenblit, and my aunt, Rachel Korenblit.

Acknowledgements

This dissertation owes much to all that I've learned from my advisor, Randall Kamien, and I thank him sincerely for his guidance, encouragement, and support over these last few years, as well as for the many wonderful opportunities he has provided me to engage with the soft matter community both within and outside of the University of Pennsylvania. I have also learned a great deal from Ricardo Mosna and Simon Čopar, and am thankful for the opportunity to collaborate with them on some of the work presented here. I have been immensely fortunate in having the chance to undertake several fruitful and enjoyable collaborations with Mohamed Gharbi, Apiradee Honglawan, Marcello Cavallaro Jr., Shu Yang, and Kathleen Stebe; their experimental results accompany much of the theoretical and numerical work in this dissertation. Also, it is a pleasure to acknowledge inspiring conversations with Carl Goodrich, Bryan Chen, Elisabetta Matsumoto, Gareth Alexander, and Carl Modes. Carl Goodrich in particular is thanked for his technical advice on numerical energy minimization, and Gareth Alexander helped me greatly in introducing me to Landau-de Gennes numerical modeling of nematic liquid crystals. Visualizations of numerical results in Chapter 2 were made using Simon Čopar's POV-Ray scene file generator *rayplot*, which he has kindly shared with me.

In addition, my work has benefited from the advice and mentorship of Tom Lubensky and Andrea Liu, and from interactions with a number of other liquid crystals scientists, including Matthew Lohr, Zoey Davidson, Joonwoo Jeong, Yu Xia, Daniel Sussman, Francesca Serra, Louis Kang, Arjun Yodh, and Peter Collings. I am also grateful for the hospitality of the University of Ljubljana Faculty of Mathematics and Physics during a visit in 2013, and especially for the opportunity to interact with Primož Ziherl, Slobodan Žumer, Miha Ravnik, David Seč, and Tine Porenta.

Finally, and most importantly, the continual love and support of my family has been invaluable to me, and so I thank my parents, Barbara and David, my brother, Joel, and my grandmothers, Sonya and Evelyn.

ABSTRACT

CONTROLLING DEFECTS IN NEMATIC AND SMECTIC LIQUID CRYSTALS THROUGH BOUNDARY GEOMETRY

Daniel A. Beller

Randall D. Kamien

Liquid crystals (LCs), presently the basis of the dominant electronics display technology, also hold immense potential for the design of new self-assembling, self-healing, and “smart” responsive materials. Essential to many of these novel materials are liquid crystalline defects, places where the liquid crystalline order is forced to break down, replacing the LC locally with a higher-symmetry phase. Despite the energetic cost of this local melting, defects are often present at equilibrium when boundary conditions frustrate the material order. These defects provide micron-scale tools for organizing colloids, focusing light, and generating micropatterned materials. Manipulating the shapes of the boundaries thus offers a route to obtaining new and desirable self-assembly outcomes in LCs, but each added degree of complexity in the boundary geometry increases the complexity of the liquid crystal’s response. Therefore, conceptually minimal changes to boundary geometry are investigated for their effects on the self-assembled defect arrangements that result in nematic and smectic-A LCs in three dimensions as well as two-dimensional smectic LCs on curved substrates. In nematic LCs, disclination loops are studied in micropost confining environments and in the presence of sharp-edged colloidal inclusions, using both numerical modeling and topological reasoning. In both scenarios, sharp edges add new possibilities for the shape or placement of disclinations, permitting new types of colloidal self-assembly beyond simple chains and hexagonal lattices. Two-dimensional smectic LCs on curved substrates are examined in the special cases where the substrate curvature is confined

to points or curves, providing an analytically tractable route to demonstrate how Gaussian curvature is associated with disclinations and grain boundaries, as well as these defects' likely experimental manifestations. In three-dimensional smectic-A LCs, novel self-assembled arrangements of focal conic domains (FCDs) are shown to arise from geometric patterning or curvature in boundaries exhibiting so-called hybrid anchoring. These new arrangements allow control over both the packing of the FCDs and their eccentricities. In general, defect self-assembly behavior in LCs is shown to depend sensitively on the shapes of confining boundaries, colloidal inclusions, and substrates, and several broad, new geometrical principles for directing the assembly of nontrivial defect configurations are presented.

Contents

1	Introduction	1
1.1	The nematic phase and disclination defects	3
1.2	Smectic-A liquid crystals and their defects	6
1.3	Outline	7
2	Disclinations in nematic liquid crystals with boundaries of complex shape	9
2.1	Introduction	9
2.2	Theory	10
2.2.1	The Q-tensor	10
2.2.2	Defects	12
2.2.3	Landau-de Gennes theory	13
2.2.4	Relation of distortion energy to Frank elasticity	14
2.2.5	Boundary terms	16
2.3	Numerical approach	19
2.3.1	Minimization algorithm	19
2.3.2	Discretizing the free energy	19
2.3.3	Nondimensionalization, material constants, and the mesh size	21
2.4	Results for sharp-edged colloidal inclusions	24
2.4.1	Background: Disclination rings around homeotropic genus-zero colloids	24

2.4.2	Evidence for realigning effects of sharp edges	26
2.4.3	Colloidal cylinders and microbullets: Shape-controlled orientation	27
2.4.4	Pair potentials for colloidal cylinders	32
2.4.5	Colloidal cubes	36
2.4.6	Summary and future work	41
2.5	Disclinations in nematic liquid crystals in micropost confining geometries	44
2.5.1	Introduction	44
2.5.2	Experimental setup and results	46
2.5.3	Landau-de Gennes numerical modeling of bulk disclination ring	48
2.5.4	Effect of bulk disclination on colloidal self-assembly at an interface	54
2.5.5	Summary	56
3	Cusps and disclinations in 2D smectics on piecewise developable surfaces	58
3.1	Introduction and summary	58
3.2	Building the layers	61
3.3	Schlieren textures	66
3.4	Smectics around edges	69
4	Focal conic domains in smectic-A liquid crystals with confining boundaries of complex shape	74
4.1	Background: Focal conic domains and the law of corresponding cones	75
4.1.1	The smectic-A phase, focal sets and Dupin cyclides	75
4.1.2	The usual parameterization	84
4.1.3	An aside: Transformations between Type I and Type II FCDs	86
4.1.4	The law of corresponding cones	89

4.2	Epitaxial directed assembly of toric focal conic domains on topographically patterned substrates	92
4.2.1	Introduction	92
4.2.2	Experimental results	95
4.2.3	Calculation of smectic free energy and critical pillar diameter .	98
4.2.4	Discussion	103
4.2.5	Conclusion	104
4.3	Hierarchical assembly of elliptic-hyperbolic focal conic domains on topographically patterned substrates	105
4.3.1	Introduction	105
4.3.2	Experimental results	107
4.3.3	Surface confinement/edge-pinning transition	110
4.3.4	Filling the smectic regions between focal conic domains	115
4.3.5	Details of calculations	121
4.3.6	Conclusion	131
4.4	Focal conic flower textures in smectic liquid crystals with curved boundaries	131
4.4.1	Introduction	131
4.4.2	Experimental results	134
4.4.3	Geometric model	139
4.4.4	Comparison and discussion of theoretical and experimental results	142
4.4.5	Conclusion	144
5	Conclusion	146
Appendix A	Relations between LdG elastic constants L_i and Frank elastic constants K_i	150

List of Figures

1.1	Illustrated examples of disclinations in 2D nematics.	5
1.2	Smectic ground state and focal conic domain.	7
2.1	Companion defects to spherical homeotropic colloids.	25
2.2	Experimental micrograph of two microbullet colloids, one with a hedgehog defect and one with a disclination line	27
2.3	Numerically modeled ellipsoidal colloid in a planar-aligned nematic cell	28
2.4	Splay and bend deformations near a right-angled edge, and supereggs with rounded edges.	30
2.5	Free energy and defect configuration for a colloidal cylinder.	33
2.6	Free energy and defect configuration of a microbullet.	34
2.7	The two mirror-image ground states of a colloidal cylinder.	36
2.8	Pair potential for two colloidal cylinders in the same one-cylinder ground state	37
2.9	Pair potential for two colloidal cylinders in mirror-image one-cylinder ground states.	38
2.10	Entangled colloidal spheres and cylinders.	39
2.11	Rotating a cubical colloid.	42
2.12	Pair potential for colloidal cubes.	43
2.13	Micropost-induced bulk defect rings: micrographs.	47
2.14	Numerical and topological evaluation of the director field.	50
2.15	The effect of surface curvature.	52

2.16	Appearance of multiple disclination rings of alternating sign around a micropost with undulating profile.	53
2.17	Elastic migration of colloidal particles induced by bulk topological defects.	55
2.18	Elastic potential experienced by colloids at the nematic-air interface .	57
3.1	Substrates with conical defects.	59
3.2	A cone is isometric to a cut planar disk with two radial lines identified	60
3.3	Cut-disk view of the cone	62
3.4	Layer structure on the 3D cone for a deficit angle $\delta = 5\pi/4$.	64
3.5	Layer structure, geodesics, and schlieren textures generated by a point defect on a conical substrate.	65
3.6	Schlieren textures for deficit angle $\delta = 3\pi/2$.	68
3.7	Substrate in the shape of a tent.	69
3.8	Smectic layers on two intersecting cones with deficit angle π .	71
3.9	Conical bump with deficit angle given by π .	71
4.1	Smectic-A ground state and anchoring conditions: schematic illustrations.	77
4.2	Focal set of an ellipse.	78
4.3	Focal set of a saddle surface.	80
4.4	Full Dupin cyclides.	81
4.5	Dupin cyclides, FCDs, and concentric spheres.	83
4.6	Complete Type I and Type II FCDs.	87
4.7	Schematic illustration of the law of corresponding cones.	90
4.8	Corresponding cones construction for Type II FCDs.	91
4.9	Thin-film smectic-A LC under hybrid boundary conditions on a featureless, planar substrate.	94

4.10	Square lattice of TFCDs on top of pillars.	96
4.11	Square lattice of TFCDs between pillars.	97
4.12	Calculated free energy ΔF of a single TFCD on a flat substrate and confined on a pillar.	102
4.13	Insensitivity of epitaxial assembly to LC thickness.	103
4.14	Hierarchically self-organized focal conic domains centered near the edges of pillars with various shapes.	109
4.15	Free energy plot and schematic illustrations showing confinement/edge-pinning transition.	112
4.16	Surface characterization of FCD formation on the circular and elliptical pillar arrays.	113
4.17	Schematic illustrations of FCDs and the edge-pinning effect.	115
4.18	Schematic illustration of ansatz for smectic layer filling between FCDs.	118
4.19	“Classical” Bragg-Sethna-Kléman-Lavrentovich model for the filling of smectic layers between FCDs.	120
4.20	Schematic diagram of the FCD arrangement assumed for the pillar topography of Fig. 4.14a.	129
4.21	Smectic flower texture of System A: experimental micrographs and measurements.	133
4.22	Smectic flower texture of System B: experimental micrographs and schematic illustrations.	135
4.23	Geometric construction of a background texture for the flower texture.	137
4.24	Corresponding cones model for the flower texture: schematic illustrations.	143

Chapter 1

Introduction

Much of what we would like to know about an ordered material—its symmetries, its material properties—is reflected in, or indeed determined by, the nature of its defects. For example, dislocation defects in the molecular lattices of metallic crystals determine the strength of the metallic solid, and deformations of a stressed metal take place through the motion of dislocations through the lattice [22]. Defects may appear not only in response to applied stress or fields but also due to thermal fluctuations, and the proliferation of defects provides the mechanism for melting into a less ordered phase [50, 72, 95]. Defects may in general be walls, lines, or points, with a small volume occupied by a defect core where the material order is destroyed in favor of a higher-symmetry phase. The symmetries of the ordered phase determine the types of defects that can arise and the ways in which those defects can interact, and in fact those symmetries are often first deduced through observations of the defects [5, 22, 23, 86].

Of both great theoretical interest and great practical importance is the fact that many commonly occurring defects are *topological* defects: The symmetries broken by the material order allow the existence of singularities that cannot be removed through any smooth deformation, except possibly by merging with another defect [86]. Analogously to an electric point charge, the presence of a defect can be detected by measuring the material order on a surface or loop enclosing the defect. Though they

can move, topological defects carry fixed topological charges, again in analogy with electric charges, and the total topological charge in a sample is typically conserved. Therefore, by appropriately choosing a material’s boundary conditions (and sometimes the topology on which the material is formed), we can ensure the existence of topological defects with a certain total topological charge. It is a more difficult task to predict the types and locations of all defects in equilibrium; some special cases are analytically tractable, while others benefit from numerical energy minimization techniques, and we will examine both types of problems here.

There are also, in certain translationally ordered media, geometrical “cusp” grain boundary singularities analogous to the caustics formed by light rays at the bottoms of swimming pools and teacups, for example. These geometrical defects, while not protected to the same degree as topological defects, would nonetheless require highly nonlocal deformations to be removed.

From a more applied perspective, defects in condensed matter systems have attracted a great deal of attention in recent years as potential tools and building blocks in self-assembly. A major goal of condensed matter science is to identify principles by which complex, functional materials could be designed to build themselves spontaneously in “bottom-up” processes from simpler materials. Inspired in part by the ubiquitous self-assembly growth processes in nature, and driven by the limitations in scale and structure of traditional “top-down” fabrication methods, materials scientists and engineers seek scenarios where maximizing entropy leads to reproducible microstructures with desired responses to light, mechanical stress, surface chemistry, etc.

Liquid crystals (LCs) are a class of materials in which defects can be observed and manipulated readily. In both their symmetries and their materials properties, liquid crystals are, as the name suggests, intermediate between solid crystals and

isotropic (disordered) liquids. Their fluidity permits reorganization of the material order in response to mechanical stresses or applied electric or magnetic fields. At the same time, their broken symmetries permit defects that are difficult or (topologically) impossible to remove without melting the sample into a higher-symmetry phase. These defects can often move through the liquid crystal and effectively exert forces, mediated by the LC’s elasticity, on one another and on embedded particles called “colloidal inclusions”—so that it is tempting (though false) to think of the defects as solid objects! In addition, because the colloidal inclusions also move through the liquid crystal to minimize elastic distortions, there is a complex interplay between colloids and defects as they seek the positions and orientations that minimize the total energy of the system.

The central theme of this dissertation is learning how to tune the properties of the boundaries, substrates, and colloidal inclusions so that liquid crystalline defects become tools guiding the self-assembly of liquid crystalline and/or colloidal micropatterns with order more complex than any of the inputs. In particular, we study the role of nontrivial boundary shape in guiding the spontaneous assembly of liquid crystalline defects into new configurations and large-scale patterns.

We focus on two LC phases, the *nematic* and *smectic-A* phases, both composed of rod-like particles with one dimension significantly larger than the other two.

1.1 The nematic phase and disclination defects

The nematic phase is translationally disordered—its particles’ positions have no long-range correlation—but orientationally ordered, meaning that the particles’ long axis orientation exhibits long-range order. This long-axis orientation, once thermal fluctuations have been averaged over, provides the order parameter of the nematic

phase, the nematic director \vec{n} . Because \vec{n} represents a direction in a system with “head-tail” symmetry, the director obeys $|\vec{n}| = 1$ and $\vec{n} = -\vec{n}$. In three-dimensional nematics, the order parameter space in which the director lives is \mathbb{RP}^2 , the unit 2-sphere with diametrically opposite points identified.

Nematic liquid crystals in two dimensions have point topological defects called *disclinations*, singularities in the director field around which the director rotates by an integer multiple of π radians on a measuring loop enclosing the disclination (see Fig 1.1a,b for examples). These defects are easily observed in polarized optical microscopy, where the LC is viewed between crossed polarizers (a “polarizer” and an “analyzer”), as the confluence of an even number of dark brushes on a bright background in what is known as a *schlieren texture* (Fig. 1.1c), from the German word for “streak”. In three dimensions, the topological defects of the nematic phase are line-like *disclinations* and point-like *hedgehogs*. Hedgehogs are defined by a topological charge counting the number of times the director field on an imaginary measuring surface around the defect wraps around the unit sphere [5]. Disclinations are defined by a topological winding number, measuring along a loop linking the disclination the number of times the director loops through \mathbb{RP}^2 . In the simplest cases where the director field lies in the plane of a cross section normal to the disclination curve’s tangent direction, the winding number is analogous to the winding number (or “index”) of point defects in 2D nematics (Fig. 1.1). However, the 3D director’s freedom to rotate into the disclination tangent direction means that the winding number is only an element of \mathbb{Z}_2 rather than \mathbb{Z} . [5, 88]. Disclination loops also carry a hedgehog charge as measured on a surface surrounding a loop.

Defects in nematic liquid crystals have attracted much attention for use in self-assembled materials, such as photonic crystals [96, 108]. A goal of recent and ongoing research is to reliably predict, and thus control, the formation of nematic defects in

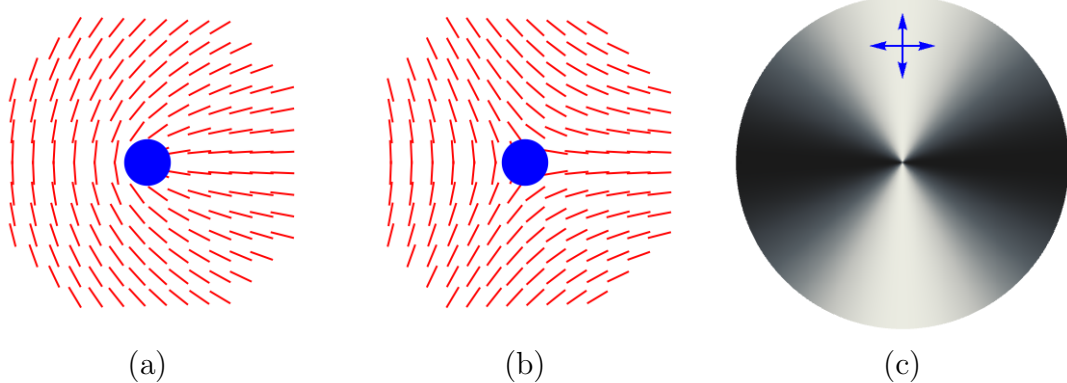


Figure 1.1: Illustrated examples of disclinations in 2D nematics, with winding number $+1/2$ (a) and $-1/2$ (b). (c) A simulated schlieren texture for both configurations (a) and (b); the blue arrows denote the directions of the polarizer and analyzer.

response to colloidal inclusions (in the bulk or at the free surface) [21, 44, 45, 47, 53, 54, 74, 94, 114, 120, 128] and to topographic features in the substrate [19]. Nontrivial boundary conditions make analytical approaches difficult, but it is important to develop a theoretical understanding of the structure of the director field near defects and of the effective interactions between colloids that result from these defects.

To this end, we have developed a computer program to numerically find energy-minimizing nematic configurations with nontrivial boundary conditions. The program employs Landau-de Gennes (LdG) numerical modeling, a tensorial approach to nematic LCs that includes defects as well as the director field among its degrees of freedom [108]. Simulating the relevant boundary conditions, we numerically evolve our modeled nematic LC toward equilibrium, providing predictions of defect type and location, as well as the relative contribution of surface, elastic, and defect core energies. Furthermore, by slowly varying the boundary conditions and comparing the free energies of the modeled equilibrium states, we extract the LC-mediated effective potential felt by colloidal inclusions.

1.2 Smectic-A liquid crystals and their defects

The smectic phase has the orientational order of the nematic phase as well as broken translational symmetry in one dimension. The rod-like molecules organize into a one-dimensional crystal of two-dimensional fluid layers, each layer one molecule in thickness. We focus in particular on the smectic-A phase, in which the nematic director aligns with the layer normal. There is a strong energetic preference for the layers to maintain equal spacing along the layer normal direction, with the spacing set by the particle length. The ground state consists of planar, evenly spaced layers separated by one particle length, with the particles oriented on average normal to the layer (see Fig. 1.2a).

The topological defects of smectics in 2D are point disclinations as in 2D nematics, as well as dislocations, points where a layer ends or begins. Only disclinations of index ≤ 1 may exist in the 2D smectic, however [23]. We will also be interested in linear, geometrical defects in 2D smectics which are “cusps” or tilt grain boundaries. In 3D smectics, the topological defects are likewise the linear disclinations and a certain type of hedgehog point defect from the 3D nematic, along with linear edge dislocations and screw dislocations. Tilt grain boundary walls are allowed two-dimensional defects in 3D smectics, although in practice such walls are often reduced to curves, a fact that is crucial to the formation of our self-assembly building block of interest in Chapter 4, the focal conic domain. In a focal conic domain, illustrated in Fig. 1.2b, smectic layers curve around two singular lines: one branch of a hyperbola, which is a cusp geometrical defect, and an ellipse, which is a disclination topological defect as well as possibly a cusp defect. The two defects together with the region of smectic layers curved around them comprises the focal conic domain, which from a self-assembly perspective we think of as a single composite defect object. The origin and properties

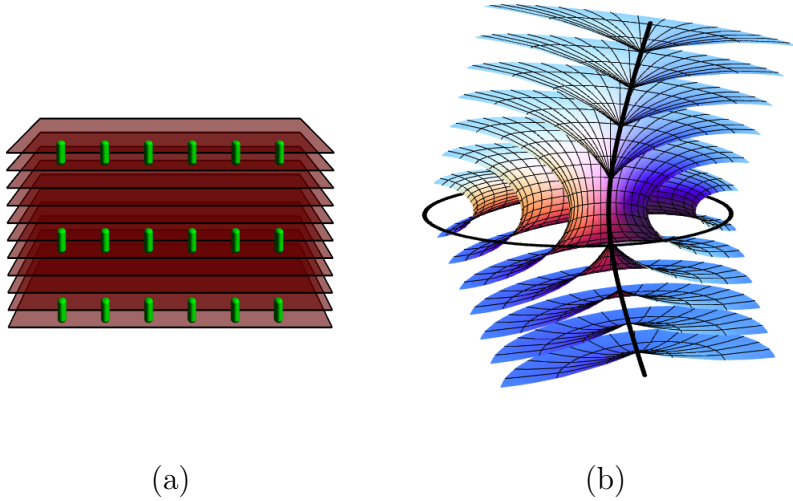


Figure 1.2: Schematically illustrated smectic-A ground state (a) with representative rodlike molecules shown in green, and (b) an illustration of a focal conic domain.

of the focal conic domain are explored in the first two sections of Chapter 4.

1.3 Outline

The remainder of this dissertation is organized as follows. In Chapter 2, we apply Landau-de Gennes numerical modeling to the study of disclinations in 3D nematic liquid crystals with boundaries of complex shape, including micropost¹ confining environments and colloidal inclusions with sharp-edges. Chapter 3 explores cusp and disclination defects that arise in 2D smectics formed on curved substrates, in the special, analytically tractable cases where the substrate's Gaussian curvature is confined to points and curves. In Chapter 4, we study the influence of curvature and topographic patterning in the boundaries on the assembly of focal conic domains in thin films of 3D smectic-A liquid crystals, using both geometrical models and computed free energy estimates. Finally, we conclude with a brief summary and outlook.

Some of the work presented here has appeared in print in the following publications

¹Throughout, we use the terms “micropost”, “micropillar”, and “pillar” interchangeably.

and has been reprinted with permission:

- A. Honglawan *et al.*, Advanced Materials **23** 5519 (2011).
- R.A. Mosna, D.A. Beller, and R.D. Kamien, Physical Review E **86** 011707 (2012).
- A. Honglawan *et al.*, Proceedings of the National Academy of Sciences **110** 34 (2013).
- M.A. Gharbi *et al.*, Liquid Crystals **40** 1619 (2013).
- M. Cavallaro *et al.*, Proceedings of the National Academy of Sciences **110** 18804 (2013).
- D.A. Beller *et al.*, Physical Review X **3** 041026 (2013).

Chapter 2

Disclinations in nematic liquid crystals with boundaries of complex shape

2.1 Introduction

We develop new principles for directed colloidal self-assembly in nematic liquid crystals through the use of Landau-de Gennes (LdG) numerical modeling [108] to study nematics with boundary conditions of complex geometry. An important and recurring theme will be the importance of shapes with sharp edges, whether in the shapes of colloidal inclusions or on a larger scale in the geometry of the confining cell. We have developed a computer program that implements LdG numerical modeling with a versatile set of options for the boundary conditions, including microposts and colloidal particles of various shapes. The code uses the “conjugate gradient” method, which is significantly faster than the gradient descent or “molecular field” update method used by other groups [108, 128], without parallelization. As well as including a versatile array of boundary conditions suitable to modeling a variety of experimental situations, the program uses a rigorous, systematic method of numerically calculating free energy components that depend on spatial gradients, to ensure downward motion

in the discretized free energy landscape at each timestep.

This chapter overviews the theoretical background and numerical setup, and then presents results for disclinations (line defects) around colloidal inclusions with sharp-edged shapes such as cylinders and cubes. Sharp edges are shown to drastically change the defect behavior compared to that seen with smooth colloid shapes like spheres and ellipsoids. Disclinations follow the sharp edges in surprising patterns, and as a result, the colloids tend to reorient relative to the background nematic director field by an angle that depends on details of the colloid shape. This has significant implications for colloidal assembly, and we explore the possibility of tuning effective colloid interaction potentials, mediated by nematic elasticity, as a function of colloid shape. In addition, we apply LdG numerical modeling to gain insights into experiments on nematics in the presence of cylindrical microposts, examining the spontaneous formation of disclination rings around microposts and their interaction with colloids at the air/liquid crystal interface.

This chapter is organized as follows. Section 2.2 reviews the Landau-de Gennes theory of nematic liquid crystals. Section 2.3 describes the numerical approach to finding free energy-minimizing nematic director fields and defect configurations. Finally, Section 2.4 presents results for disclination rings around colloidal inclusions with sharp edges, and Section 2.5 presents results for disclination rings in micropost confining geometries.

2.2 Theory

2.2.1 The Q-tensor

Uniaxial nematic liquid crystals have as their order parameter a director, \vec{n} , which is a unit vector with the identification $\vec{n} = -\vec{n}$. It has two degrees of freedom for a 3D

nematic. The liquid crystal configuration is an assignment of a director $\vec{n}(\vec{x})$ to each point \vec{x} in the nematic, i.e., a mapping from the sample space (minus any defect sets) to the order parameter space, $\mathbb{R}\mathbf{P}^d$, where \vec{n} lives (usually with d one less than the dimension of the sample space).

Here, we model nematic LCs with greater generality using instead a second-rank, traceless, symmetric tensor \mathbf{Q} called the Q-tensor. With \mathbf{Q} , one can simulate the more general case of the *biaxial* nematic, where the rotational symmetry about \vec{n} is broken, picking out a second director \vec{m} orthogonal to \vec{n} , along which one of the shorter axes of the molecules aligns. Also, because one of the Q-tensor's degrees of freedom is the nematic degree of order, defects in the nematic can arise from the evolution of the field $\mathbf{Q}(\vec{x})$ and need not be prescribed as part of the boundary conditions.

Generally, in three dimensions the components of \mathbf{Q} are given by [93]

$$Q_{\alpha\beta} = S_1 n_\alpha n_\beta + S_2 m_\alpha m_\beta - \frac{1}{3}(S_1 + S_2)\delta_{\alpha\beta}. \quad (2.1)$$

The above expression is frequently written in the equivalent form

$$Q_{\alpha\beta} = \frac{3}{2}S \left(n_\alpha n_\beta - \frac{1}{3}\delta_{\alpha\beta} \right) + \frac{1}{2}S_B (m_\alpha m_\beta - \ell_\alpha \ell_\beta)$$

where $\vec{l} = \vec{n} \times \vec{m}$.

Whereas identifying \vec{n} with $-\vec{n}$ leads to computational challenges in the presence of half-integer strength disclinations, \mathbf{Q} is well-defined because it is invariant under $\vec{n} \rightarrow -\vec{n}$. \mathbf{Q} has five degrees of freedom: two angles from \vec{n} and one from \vec{m} , along with the real numbers S_1 and S_2 . In a basis where two of the axes are given by \vec{n} and

\vec{m} , \mathbf{Q} is diagonal and reads

$$\mathbf{Q} = \frac{1}{3}\text{diag}(2S_1 - S_2, 2S_2 - S_1, -S_1 - S_2). \quad (2.2)$$

The diagonal elements are the eigenvalues. Without loss of generality, suppose that $S_1 \geq S_2$. Then $S \equiv \frac{1}{3}(2S_1 - S_2)$ is the largest eigenvalue; the second-largest is $\frac{1}{3}(2S_2 - S_1) = -\frac{1}{2}(S - S_2)$, and the smallest is $\frac{1}{3}(-S_1 - S_2) = -\frac{1}{2}(S + S_2)$.

The nematic director \vec{n} is recovered as the eigenvector of \mathbf{Q} corresponding to its largest eigenvalue, which is S . Notice that when the smaller two eigenvalues are degenerate (equal), we have $S_2 = 0$ and hence $S_1 = \frac{3}{2}S$. This is the *uniaxial limit*, where no \vec{m} is selected. Equation (2.1) then reduces to

$$Q_{\alpha\beta} = \frac{3}{2}S(n_\alpha n_\beta - \frac{1}{3}\delta_{\alpha\beta}). \quad (2.3)$$

Because S_2 goes to zero in the uniaxial phase, it is a measure of the degree of biaxial order, and is sometimes labeled S_B . S is called the *nematic degree of order*. In terms of S and S_B , Equation 2.2 reads (for a frame in which \mathbf{Q} is diagonal)

$$\mathbf{Q} = \text{diag}(S, -\frac{1}{2}(S - S_B), -\frac{1}{2}(S + S_B)). \quad (2.4)$$

2.2.2 Defects

As well as allowing biaxiality, the Q-tensor provides the advantage that, since it contains the scalar order parameters S and S_B , it can realistically simulate disclinations in the nematic by allowing degeneracy of the leading eigenvalue, corresponding to a local melting of the nematic into the isotropic phase. Wherever the largest eigenvalue is degenerate (the two largest eigenvalues are equal), \vec{n} is ill-defined and that point is

part of a defect. Degeneracy of the largest eigenvalue implies that $S_2 = S_1 = 3S$, and therefore that

$$\det(\mathbf{Q}) = \frac{1}{4}S(S^2 - S_2^2) = -2S^3, \quad (2.5)$$

$$\text{tr}(\mathbf{Q}^2) = \frac{1}{2}(3S^2 + S_2^2) = 6S^2. \quad (2.6)$$

We could therefore consider as belonging to a defect any point where the quantity

$$(\text{tr}(\mathbf{Q}^2))^3 - 54|\det(\mathbf{Q})|^2 \quad (2.7)$$

is sufficiently close to zero.

In practice, we take the simpler approach of marking any site where S falls sufficiently below its bulk equilibrium value S_0 as belonging to a defect [108]. Our program outputs the location and order parameter of all points where $S < 0.9S_0$. Further filtering of S values on a case-by-case basis is needed before we can plot the defect locations.²

2.2.3 Landau-de Gennes theory

Here we discuss a formulation for the free energy density in the bulk of the nematic in terms of \mathbf{Q} , postponing consideration of the surface energies until Subsection 2.2.5.

²A third possible method is to define as a defect any point where $\det(\mathbf{Q})$ is negative, or less than some small positive threshold value. This works because, in the uniaxial case,

$$\begin{aligned} \mathbf{Q} &= \text{diag}(S, -\frac{1}{2}S, -\frac{1}{2}S) \\ \Rightarrow \det(\mathbf{Q}) &= \frac{1}{4}S^3. \end{aligned}$$

From this result together with Equation (2.5), we see that $\det(\mathbf{Q})$ goes from positive to nonpositive in going from a uniaxial nematic to a defect. In the uniaxial limit, where the smaller two eigenvalues are equal, the defect condition that the greater two eigenvalues are equal implies that all eigenvalues are equal. Since tracelessness implies that the eigenvalues sum to zero, we must have $S = 0$ and thus $\det(\mathbf{Q}) = 0$.

The following energy goes by the name of Landau-de Gennes.

$$F_{\text{LdG}} = \int_V dV \left\{ \left[\frac{1}{2} A \text{tr}(\mathbf{Q}^2) + \frac{1}{3} B \text{tr}(\mathbf{Q}^3) + \frac{1}{4} C (\text{tr}(\mathbf{Q}^2))^2 \right] + \frac{L_1}{2} (\nabla \times \mathbf{Q} + 2q_0 \mathbf{Q})^2 + \frac{L_2}{2} (\nabla \cdot \mathbf{Q})^2 \right\}. \quad (2.8)$$

The term in square brackets is the “phase” free energy which stabilizes the nematic phase against the isotropic phase, with $A \propto T - T_{\text{NI}}^*$, where T_{NI}^* is the supercooling temperature of the isotropic phase. In the uniaxial limit, $\mathbf{Q} = \text{diag}(S, -\frac{1}{2}S, -\frac{1}{2}S)$, so

$$\begin{aligned} \text{tr}(\mathbf{Q}^2) &= \frac{3}{2}S^2 \\ \frac{1}{3}\text{tr}(\mathbf{Q}^3) &= \det(\mathbf{Q}) = \frac{1}{4}S^3 \end{aligned}$$

and the phase free energy becomes

$$f_{\text{phase}} = \frac{3}{4}AS^2 + \frac{1}{4}BS^3 + \frac{9}{16}CS^4,$$

and then f_{phase} is minimized either by $S = 0$ or by

$$S = S_0 \equiv \frac{-B + \sqrt{B^2 - 24AC}}{6C}, \quad (2.9)$$

with a first-order transition given by the condition $36AC + B(-B + \sqrt{B^2 - 24AC}) = 0$.

2.2.4 Relation of distortion energy to Frank elasticity

By equating the distortion energy in the Landau-de Gennes theory,

$$f_d = \frac{L_1}{2}(\nabla \times \mathbf{Q} + 2q_0 \mathbf{Q})^2 + \frac{L_2}{2}(\nabla \cdot \mathbf{Q})^2, \quad (2.10)$$

in the uniaxial limit where $Q_{\alpha\beta} = \frac{3}{2}S(n_\alpha n_\beta - \frac{1}{3}\delta_{\alpha\beta})$, to the free energy density of Frank elasticity,

$$f_{\text{Frank}} = \frac{K_1}{2}(\nabla \cdot \vec{n})^2 + \frac{K_2}{2}(\vec{n} \cdot (\nabla \times \vec{n}))^2 + \frac{K_3}{2}((\vec{n} \cdot \nabla)\vec{n})^2 \quad (2.11)$$

(where K_1 , K_2 , and K_3 are respectively the splay, twist, and bend elastic moduli), we find

$$K_1 = \frac{9}{4}S^2(L_1 + L_2), \quad K_2 = \frac{9}{2}S^2L_1, \quad K_3 = \frac{9}{4}S^2(L_1 + L_2). \quad (2.12)$$

The calculation can be found in Appendix A.

Unfortunately, this shows that Landau-de Gennes theory at quadratic order requires $K_1 = K_3$. It is possible to add higher-order terms that allow us to distinguish K_1 from K_3 ([3], [108], [93]), though this involves making some arbitrary choices from among many suitable higher-order terms in the free energy. Following [108], the choice we make is:

$$f_d = \frac{1}{2}L_1 \frac{\partial Q_{ij}}{\partial x_k} \frac{\partial Q_{ij}}{\partial x_k} + \frac{1}{2}L_2 \frac{\partial Q_{ij}}{\partial x_j} \frac{\partial Q_{ik}}{\partial x_k} + \frac{1}{2}L_3 Q_{ij} \frac{\partial Q_{kl}}{\partial x_i} \frac{\partial Q_{kl}}{\partial x_j} \quad (2.13)$$

where $L_1 = (2/3)(-K_1 + 3K_2 + K_3)/9S^2$, $L_2 = 4(K_1 - K_2)/9S^2$, and $L_3 = 4(K_3 - K_1)/27S^3$ (see Appendix A for calculation).

In the case where all elastic constants are equal, the distortion free energy density is simply

$$f_d = \frac{L_1}{2} \frac{\partial Q_{ij}}{\partial x_k} \frac{\partial Q_{ij}}{\partial x_k}, \quad (2.14)$$

with the correspondence $K_1 = K_2 = K_3 = \frac{9}{2}S^2L_1$ to the Frank free energy density in the case of equal elastic constants. Computation is significantly faster in the equal-constants case.

The Frank elastic energy technically also includes a saddle-splay term,

$$f_{24} = -\frac{K_{24}}{2} \nabla \cdot [\vec{n} (\nabla \cdot n) - (\vec{n} \cdot \nabla) \vec{n}] \quad (2.15)$$

As this term is a total divergence, it can be integrated to a surface term. It becomes important when \vec{n} is allowed to vary at the boundaries, or when the energies of different boundary configurations are being compared. As K_{24} is notoriously difficult to measure, this term is often excluded, and we do not compute it in our numerical approach. However, the term in square brackets in Equation 2.15 can be rewritten in terms of the Q-tensor (in the uniaxial limit) as [122]

$$[\vec{n} (\nabla \cdot n) - (\vec{n} \cdot \nabla) \vec{n}]_i = \left(\frac{3S}{2} \right)^{-2} [Q_{ij} \partial_k Q_{jk} - Q_{jk} \partial_k Q_{ij}]. \quad (2.16)$$

We may therefore call the divergence of the right-hand side of Equation 2.16 “the saddle-splay” in the LdG approach.

2.2.5 Boundary terms

In the numerical approach discussed in the next section, every simulated point on the simulation lattice contributes to the Landau-de Gennes free energy (2.8). Points adjacent to a boundary surface (e.g. substrate, air, post, colloid) contribute an additional energy per unit area f_s associated with the local deviation of \vec{n} from a locally preferred alignment direction or set of directions, referred to as *anchoring*. For most boundary surfaces, we allow for two cases: homeotropic and degenerate planar anchoring. For homeotropic anchoring, the preferred direction is along the unit normal $\hat{\nu}^s$ to the interface s , and we use the Rapini-Papoulier (or Nobili-Durand) anchoring

potential,

$$\Phi_{s,H} = W_0^s \int_s dA \operatorname{tr} ((\mathbf{Q} - \mathbf{Q}^s)^2) = W_0^s \int_s dA (Q_{\alpha\beta} - Q_{\alpha\beta}^s) (Q_{\beta\alpha} - Q_{\beta\alpha}^s) \quad (2.17)$$

Here, W_0^s is the anchoring strength of the surface s , the integration is carried out over that surface, and \mathbf{Q}^s is the locally preferred Q-tensor, which we take to be

$$Q_{\alpha\beta}^s = \frac{3}{2} S_0 (\nu_\alpha^s \nu_\beta^s - \frac{1}{3} \delta_{\alpha\beta}) \quad (2.18)$$

with S_0 as defined in Equation (2.9). This anchoring is easily adapted to unidirectional planar anchoring simply by changing the definition of $\hat{\nu}^s$ to the locally preferred director (“easy axis” or “rubbing direction”), an approach that we will use to study colloidal particles in thin-cell nematics in Section 2.4. In terms of \vec{n} , the Rapini-Papoulier potential is often written

$$\Phi_{s,H} = \frac{W}{2} [1 - (\vec{n} \cdot \hat{\nu}^2)], \quad (2.19)$$

which in a uniaxial limit is the same as Equation 2.18 with the identification $W = 9S_0^2 W_0$.

The effect of the anchoring on the system is often described by an extrapolation length

$$\xi_s = K_3/W \quad (2.20)$$

where K_3 is the Frank bend elastic constant [123]. The anchoring is strong or weak depending on whether ξ_s is small or large (respectively) compared to the length scales of the system. A particle of radius a with radial anchoring will induce an elastic energy $\sim K_3 a$ (assuming uniform alignment infinitely far from the particle) and a surface energy $\sim Wa^2$. Thus, for $\xi_s \ll a$, there is perfect anchoring; for $\xi_s \gg a$ there

is uniform alignment in violation of the anchoring potential. Alternatively, Stark [123] characterizes the anchoring strength by the dimensionless quantity γ_N , defined as the ratio of the surface extrapolation length L/W_0 to the nematic corellation length $\xi_N \sim \sqrt{L/A}$ defined in subsection 2.3.3:

$$\gamma_n = \frac{L}{\xi_N W_0}. \quad (2.21)$$

For degenerate planar anchoring, we penalize deviations of \vec{n} from the plane orthogonal to the interface normal $\hat{\nu}^s$. We use the potential given in Ref. [39]:

$$\Phi_{s,\text{D.G.}} = W_1^s \left(\tilde{Q}_{\alpha\beta} - \tilde{Q}_{\alpha\beta}^\perp \right) \left(\tilde{Q}_{\alpha\beta} - \tilde{Q}_{\alpha\beta}^\perp \right) + W_2^s \left(\tilde{Q}_{\alpha\beta} \tilde{Q}_{\alpha\beta} - \left(\frac{3}{2} S_0 \right)^2 \right)^2, \quad (2.22)$$

where

$$\tilde{Q}_{\alpha\beta} \equiv Q_{\alpha\beta} + \frac{1}{2} S_0 \delta_{\alpha\beta} \quad (2.23)$$

and $\tilde{\mathbf{Q}}^\perp$ is the projection of $\tilde{\mathbf{Q}}$ onto the substrate,

$$\tilde{Q}_{\alpha\beta}^\perp = P_{\alpha\gamma} \tilde{Q}_{\gamma\delta} P_{\delta\beta}, \quad (2.24)$$

using the projection operator $P_{\alpha\beta} \equiv \delta_{\alpha\beta} - \nu_\alpha^s \nu_\beta^s$.³ The first term in (2.22) penalizes deviations of \vec{n} out of the plane orthogonal to $\hat{\nu}^s$, while the second term penalizes deviations of the scalar order parameter from S_0 . We make the simplifying assumption $W_2^s = W_1^s$.

The total free energy to be minimized is then

$$F = F_{\text{LdG}} + \sum_s \Phi_s \quad (2.25)$$

³Note that our definition of S_0 differs by a factor of 3/2 from that used in Ref. [39].

where the last term is a summation over all boundary surfaces. In Section 2.3, we will discuss how we minimize F .

2.3 Numerical approach

This section summarizes our numerical approach to finding free energy-minimizing nematic configurations.

2.3.1 Minimization algorithm

To minimize F , the program offers the option of using either nonlinear conjugate gradient (CG) or LBFGS, both using routines from the ALGLIB library for C++ (<http://www.alglib.net>).⁴ These methods do not simulate a realistic relaxational dynamics for the liquid crystal, in contrast to the molecular field approach used by others [3] [108] (sometimes augmented by simulated hydrodynamics). Instead, they efficiently search for local minima in the free energy landscape. The speeds of CG and LBFGS seem to be roughly equivalent for our problem, and all results presented here are obtained using CG. The gradient descent (a.k.a. steepest descent) method is also available but is typically at least an order of magnitude slower. This implementation of gradient descent is effectively equivalent to the molecular field approach used by others (e.g. [108]).

2.3.2 Discretizing the free energy

The free energy F is written as a functional of $Q_{\alpha\beta}(\mathbf{x})$ where $(\alpha, \beta) = (x, x), (x, y), (x, z), (y, y), (y, z)$. That is, the symmetry and tracelessness of \mathbf{Q} are taken into account before discretization. F is then discretized in a finite difference scheme as a function

⁴For an introduction to CG minimization, see Ref. [116].

of the $5N$ independent variables $\{Q_{\alpha\beta}(j)\}$ where $j = 1, \dots, N$ labels the lattice site:

$$F = \sum_j f(j).$$

For energy terms that depend only on the local value of \mathbf{Q} , such as the “phase” free energy term, this discretization is straightforward. For energy terms that depend on first derivatives of \mathbf{Q} , we use discretized forms of the derivative given by (for the case of the x derivative)

$$\partial_x^+ Q_{\alpha\beta}(j) = Q_{\alpha\beta}(xup) - Q_{\alpha\beta}(j)$$

$$\partial_x^- Q_{\alpha\beta}(j) = Q_{\alpha\beta}(j) - Q_{\alpha\beta}(xdwn)$$

Here xup and $xdwn$ are the j -values labeling the neighboring lattice sites to the right and left of site j . At each lattice site j , the program checks whether the neighboring sites xup and $xdwn$ are simulated sites (as opposed to outside of the boundaries). If xup is not a simulated site but $xdwn$ is simulated, then ∂_x^- is used; if $xdwn$ is not a simulated site but xup is, then ∂_x^+ is used. (If both xup and $xdwn$ are not simulated, then the derivative is set to 0, but this situation is to be avoided.) For the bulk case where both xup and $xdwn$ are simulated sites, we take as $f(j)$ the *average* of its value using ∂_x^+ and its value using ∂_x^- . We do this rather than using the symmetric form of the first derivative $\partial_x Q_{\alpha\beta}(j) = Q_{\alpha\beta}(xup) - Q_{\alpha\beta}(xdwn)$ (i.e. “squaring before adding” rather than “adding before squaring”) because the latter results in a numerical artifact wherein next-nearest neighbors in each direction align but nearest neighbors do not.

This procedure is repeated similarly for y and z derivatives, while averaging all uses of ∂^+ and ∂^- that are compatible with the status (simulated or not simulated) of neighboring sites. Thus a site whose six nearest neighbor sites are all simulated sites

will use an average of $2^3 = 8$ combinations of derivative definitions.

Minimization algorithms such as CG and LBFGS require us to provide a definition of the discretized version $\text{grad}(j, \alpha, \beta)$ of the functional derivative $\delta F/\delta Q_{\alpha\beta}(\mathbf{x})$ of the free energy with respect to each of the independent variables. We do this straightforwardly by differentiating the discretized version of the free energy density f with respect to $Q_{\alpha\beta}(j)$:

$$\text{grad}(j, \alpha, \beta) \equiv \frac{\partial}{\partial Q_{\alpha\beta}(j)} \sum_{j'} f(j') = \frac{\partial}{\partial Q_{\alpha\beta}(j)} \sum_{\substack{j' = j \text{ and} \\ \text{nearest neighbors}}} f(j').$$

For energy terms not involving spatial derivatives, this is straightforward. For energy terms that do contain spatial derivatives, we have to allow for the possibility of any combination of nearest neighbors being simulated or not simulated, a total of $2^6 = 64$ possibilities. Our approach is to explicitly differentiate the discretized free energy expressions with respect to the \mathbf{Q} -values of neighboring sites for all possible combinations of simulated and not simulated neighbors, and then evaluate the appropriate expressions as needed during the calculation. A Mathematica routine has been developed to automate this case-by-case differentiation and output the explicit discretized free energy gradient expressions to C++ files.

2.3.3 Nondimensionalization, material constants, and the mesh size

The LdG free energy in Equation (2.8) is nondimensionalized using the grid spacing Δx as follows.

$$\tilde{F}_{\text{LdG}} = \int_V d\tilde{V} \left\{ \left[-\frac{1}{2} \text{tr} (\mathbf{Q}^2) + \frac{\tilde{B}}{3} \text{tr} (\mathbf{Q}^3) + \frac{\tilde{C}}{4} (\text{tr} (\mathbf{Q}^2))^2 \right] \right\}$$

$$+ \frac{\tilde{L}_1}{2} \left(\tilde{\nabla} \times \mathbf{Q} + 2\tilde{q}_0 \mathbf{Q} \right)^2 + \frac{\tilde{L}_2}{2} \left(\tilde{\nabla} \cdot \mathbf{Q} \right)^2 \} \quad (2.26)$$

where $\tilde{F}_{\text{LdG}} \equiv F_{\text{LdG}} / (|A|(\Delta x)^3)$, $d\tilde{V} \equiv dV / (\Delta x)^3$, $\tilde{B} \equiv B / |A|$, $\tilde{C} \equiv C / |A|$, $\tilde{L}_{1,2} \equiv L_{1,2} / (|A|(\Delta x)^2)$, $\tilde{\nabla} \equiv \Delta x \nabla$, $\tilde{q}_0 \equiv \Delta x q_0$. Likewise, in the surface energy we will replace anchoring strengths W with $\tilde{W} \equiv W / (|A|\Delta x)$.

In the numerical modeling, we choose the energy and length scales by setting $|A| = 1$ and $\Delta x = 1$. When using the numerical modeling to obtain free energy differences, we have to multiply the free energy result by $|A|(\Delta x)^3$ using the actual value of $|A|$ and $\Delta x = L_{x,\text{exp}} / L_x$ where $L_{x,\text{exp}}$ is the actual system size in the x direction (for example) and L_x is the number of grid points in that direction.

From Ref. [108], we take typical values for the material constants of the commonly used nematic liquid crystal 5CB: $A = -0.172 \times 10^6 \text{ J/m}^3$, $B = -2.12 \times 10^6 \text{ J/m}^3$, $C = 1.73 \times 10^6 \text{ J/m}^3$. These values give $S_0 \approx 0.533$. We set the elastic constants $L_1 = L_2 \equiv L = 8 \times 10^{-12} \text{ N}$ so that the Frank elastic constant $K = L \cdot 9S_0^2 / 2 \approx 10^{-11} \text{ N}$ roughly matches the elastic constants of 5CB [47]. In practice, the procedure is numerically stable and produces reasonable results only in a small range of \tilde{L} near the default value 2.32, so changing L amounts to changing Δx .

For homeotropic anchoring (5CB in contact with a surface treated with DMOAP at room temperature), the typical anchoring strength is $W_0 \approx 1 \times 10^{-2} \text{ J m}^{-2}$ [118], giving an extrapolation length $L/W_0 = 4 \text{ nm}$. For oriented planar anchoring (5CB in contact with a rubbed PVA layer at room temperature), the typical anchoring strength is $W_0 \approx 1.5 \times 10^{-5} \text{ J m}^{-2}$ [102].

When nondimensionalizing, we take $\tilde{B} = -2.12/0.172$, $\tilde{C} = 1.73/0.172$. We compute \tilde{L} as

$$\tilde{L} = \frac{8 \times 10^{-12} \text{ N}}{0.172 \times 10^6 \text{ J/m}^3 (\Delta x)^2}$$

and W for homeotropic anchoring as

$$\tilde{W} = \frac{1 \times 10^{-2} \text{ J m}^{-2}}{0.172 \times 10^6 \text{ J/m}^3 (\Delta x)}$$

Using these values, the simulation gives reasonable results for $\Delta x = 10$ nm but not for $\Delta x = 20$ nm. For $\Delta x = 4.5$ nm, we have $\tilde{L} \approx 2.32$ and $\tilde{W} \approx 12.9$. (For oriented planar anchoring, $\tilde{W} \approx 0.0193$.)

The order of magnitude of the mesh size Δx is set by the nematic correlation length ξ_N . This is a length scale associated with spatial distortions in S , neglecting spatial distortions in \vec{n} . We derive ξ_N following the discussion in Ref. [108]. The single-elastic-constant distortion energy expression $(L/2)(\nabla \mathbf{Q})^2$ becomes $(3/4)L(\nabla S)^2$ upon taking the uniaxial limit, and the Landau-de Gennes free energy density becomes

$$f_{\text{LdG}} = \left[\frac{3}{4}AS^2 + \frac{1}{4}BS^3 + \frac{9}{16}CS^4 \right] + \frac{3}{4}L(\nabla S)^2. \quad (2.27)$$

The Euler-Lagrange equation for this energy density is

$$\frac{3}{2}L\nabla^2 S - \frac{\partial f_{\text{LdG}}}{\partial S} = 0. \quad (2.28)$$

Linearizing with respect to small deviations $\Delta S(\mathbf{x})$ about the equilibrium value S_0 , we find that the length scale associated with spatial change in $\Delta S(\mathbf{x})$ is

$$\xi_N = \sqrt{\frac{3}{2} \frac{L}{(\partial^2 f_{\text{LdG}} / \partial S^2)|_{S_0}}} \quad (2.29)$$

$$= \sqrt{\frac{L}{A + BS_0 + \frac{9}{2}CS_0^2}} \quad (2.30)$$

For the typical material constants of 5CB mentioned above, we obtain $S_0 \approx 0.533$ and

$\xi_N \approx 6.63$ nm. Note that this is very similar to the surface extrapolation length L/W_0 for homeotropic anchoring discussed above.

2.4 Results for sharp-edged colloidal inclusions

2.4.1 Background: Disclination rings around homeotropic genus-zero colloids

If the nematic director relaxes to a uniform director field at large distances or at the sample boundary, then the sample must contain zero total topological charge [86]. Thus, a defect of unit topological charge will be accompanied by a defect of the opposite charge, and the two will tend to annihilate for energetic reasons, leaving a defect-free nematic configuration. However, a spherical colloid imposing strong homeotropic (normal) anchoring on the director field at the colloid's surface acts as a radial hedgehog, and is thus accompanied by a stable topological defect [129].

This companion defect can be either a hyperbolic point hedgehog or a ring disclination of unit topological charge (Fig. 2.1). In the latter case, the ring's stable position is around the equator of the colloid, and the ring is referred to as a “Saturn ring” defect. For an isolated spherical colloid, the director field in a cross-section transverse to the disclination tangent is that of a 2D nematic disclination with winding number $-1/2$ (Fig. 1.1b). The Saturn ring sits in the plane orthogonal to the far-field nematic director \vec{n}_0 , and the director field has quadrupolar symmetry [81]. In the case of a hedgehog defect, the separation vector between the colloid's center and the hedgehog is parallel to \vec{n}_0 , and the director field has dipolar symmetry. Smaller colloid size or stronger confinement tends to stabilize the Saturn ring relative to the hedgehog.

These sphere-defect pairs self-assemble into chains parallel to \vec{n}_0 in the case of hedgehog defects, and kinked chains nearly perpendicular to \vec{n}_0 in the case of Saturn rings [94, 118]. Saturn rings of neighboring colloids may also join into a single disclination ring that entangles pairs or chains of colloids [106].

For homeotropic colloids that are topologically but not geometrically spheres, such as cubes and cylinders (with edges at least slightly rounded), the same topology applies to the surrounding nematic: Each genus-zero colloid is accompanied by a companion defect, either a hedgehog or a disclination ring [53, 54, 131]. Colloidal cylinders were shown to form chains and bound pairs depending on the types and positions of their companion defects [131]. In the case of a hedgehog, the cylinders oriented so that their long axis was parallel to the topological dipole and \vec{n}_0 . In the case of a disclination ring, the ring wrapped around the long axis of the cylinder.

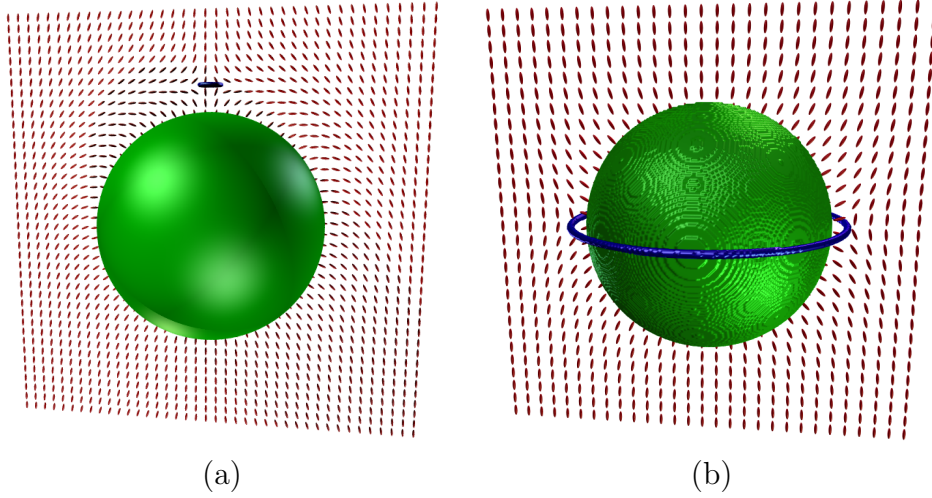


Figure 2.1: Companion topological defects to spherical homeotropic colloids in nematic liquid crystals. (a) Hyperbolic hedgehog (dipolar configuration). (b) Saturn ring disclination (quadrupolar configuration).

2.4.2 Evidence for realigning effects of sharp edges

“Microbullet” colloids, colloidal rods with one hemispherical end and one flat end, were studied in thin nematic cells [44]. In the case of hedgehog defects, the microbullet oriented parallel to \vec{n}_0 , as do colloidal cylinders. However, the hedgehog always formed near the rounded end of the microbullet. As a result, colloidal assembly took on a polar character: parallel colloids attracted end-to-end but repelled laterally, while antiparallel colloids assembled into tilted dimers when approaching head-on and attracted side-to-side. In thin homeotropic cells (vertical director anchoring at the top and bottom surfaces), these interactions led after long times to triangular lattices of repelling parallel microbullets, with some sites occupied by aggregates of antiparallel microbullets.

In a planar cell (\vec{n}_0 is horizontal), when the cell thickness is decreased to slightly greater than the microbullet’s diameter, the hedgehog defect is replaced by a disclination ring that wraps around the long axis of the colloid. Surprisingly, the colloid is oriented with its long axis making an oblique angle with \vec{n}_0 (and lying in a horizontal plane). Figure 2.2 shows an experimental micrograph of two microbullets, one with a hedgehog defect and aligned parallel to \vec{n}_0 as expected, and the other with a disclination ring and aligned at a roughly 72° angle from \vec{n}_0 . Cylindrical colloids have also been shown to orient with their long axes at angles ranging from 35° to 90° relative to \vec{n}_0 , though the shapes of these colloids were less precisely controlled [131].

LdG numerical modeling of ellipsoidal inclusions shows that this oblique alignment of microbullets and cylinders does not arise merely from the fact that the colloids are elongated. Figure 2.3 gives numerical results for ellipsoidal colloids of diameter $0.2 \mu\text{m}$ and various aspect ratios in a thin planar cell of 5CB, where infinitely strong unidirectional planar anchoring at the top and bottom surfaces defines a horizontal

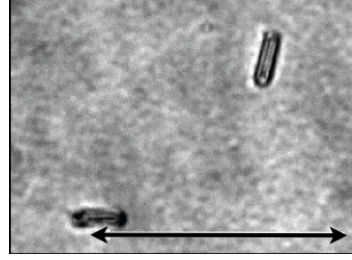
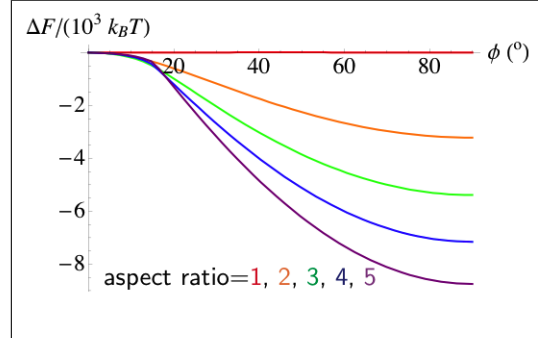


Figure 2.2: Two microbullet colloids in a thin nematic cell. The microbullet at top right has a disclination ring, while the microbullet at bottom left has a hedgehog (point) defect. The black arrow represents the far-field nematic director set by the cell boundaries. Both colloids are $10 \mu\text{m}$ in length. Image courtesy of M. Gharbi.

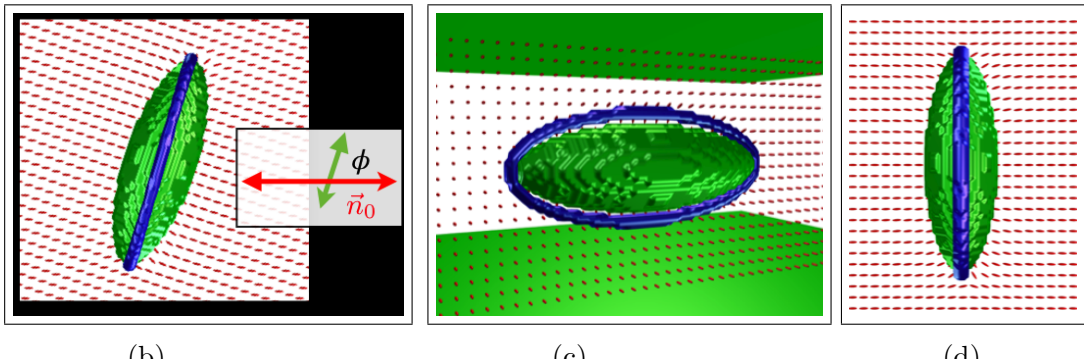
far-field director \vec{n}_0 . The colloid surface imposes homeotropic anchoring of infinite strength, and the one-elastic-constant material values as given in subsection 2.3.3 are used to model 5CB. We calculate the change in free energy as the angle ϕ between the ellipsoid's long axis and \vec{n}_0 is varied. The disclination always wraps around the long axis of the ellipsoid, but the preferred orientation for all aspect ratios greater than 1 is $\phi = 90^\circ$. (When the aspect ratio is 1, the ellipsoid is a sphere, and varying ϕ changes nothing.) Thus changing the colloidal shape from spherical to ellipsoidal shows wrapping of the disclination ring around the colloid's long axis, but does not demonstrate oblique colloidal orientation.

2.4.3 Colloidal cylinders and microbullets: Shape-controlled orientation

In order to examine the details of the shape dependence of colloidal alignment and assembly in nematics, we alter the simulated particles to model the sharp features of these shapes. However, we have to take care not to make the modeled corners *too* sharp because perfectly sharp corners introduce an unrealistic ambiguity into the director field: The rotation of the director through 90° can be accomplished through either



(a)



(b)

(c)

(d)

Figure 2.3: (a) Free energy of an ellipsoidal colloid (short axis diameter $0.2 \mu\text{m}$) in a planar-aligned nematic cell (thickness $0.6 \mu\text{m}$), with the colloid's long axis lying in the horizontal plane and making an angle ϕ with the far-field director \vec{n}_0 . The reference energy for each curve is the free energy at $\phi = 0$. At all aspect ratios larger than unity, $\phi = 90^\circ$ is energetically preferred. The setup used to calculate this plot is illustrated in (b). As shown in (b)-(d), the disclination ring wraps around the long axis of the colloid. (c) and (d) show side and top views, respectively, of the minimum-energy colloidal orientation. Boundaries are colored green; defects are marked by blue isosurfaces of order parameter $S = 0.48$; and red rods show the director field in a chosen plane.

splay (Fig. 2.4a), or bend (Fig. 2.4b). Because the colloidal corners are expected to be rounded convexly at least at the molecular scale of the nematic correlation length ξ_N , the splay configuration is more realistic. In order to obtain this configuration, we round the corners of simulated cylinders using the “superegg” equation:

$$\left(\frac{\rho^2}{b^2}\right)^p + \left(\frac{z^2}{a^2}\right)^p = 1 \quad (2.31)$$

Here, $\rho \equiv \sqrt{x^2 + y^2}$ and the coordinate frame has been rotated so that the colloid long axis points along the z direction; b is the colloid radius; a is half the colloid length; and p is a parameter we refer to as the “sharpness” of the shape. For $p = 1$, the shape is an ellipsoid. As p is increased above 1, the superegg interpolates between an ellipsoid and a right circular cylinder as $p \rightarrow \infty$ (Fig. 2.4c). To model microbullets, only the half of the colloid opposite the hemispherical cap is given the superegg shape; the other half is spherocylindrical, with no sharp edges to worry about.

The numerical results for cylinders modeled as supereggs with sharpness $p = 10$ are given in Fig. 2.5. (Here and for microbullets, the colloid diameter $0.2\text{ }\mu\text{m}$ and cell thickness $0.6\text{ }\mu\text{m}$ are the same as for the ellipsoids above.) As with the ellipsoid, the disclination ring wraps around the long axis of the colloid. However, something new happens at the sharp edges at the ends of the cylinder: The disclination loop kinks into an “S” shape to follow one half of the circular edge at one end and the opposite half of the circular edge at other end! Why? Disclinations are actually tubes of locally melted nematic. Since a disclination must exist topologically, its geometry ought to adapt to melt the nematic near places where the boundary conditions require the most director distortion, with the caveat that a core energy per unit length discourages longer disclination ring configurations. At the sharp edges of the cylinder, homeotropic boundary conditions require the director to rotate by 90° within

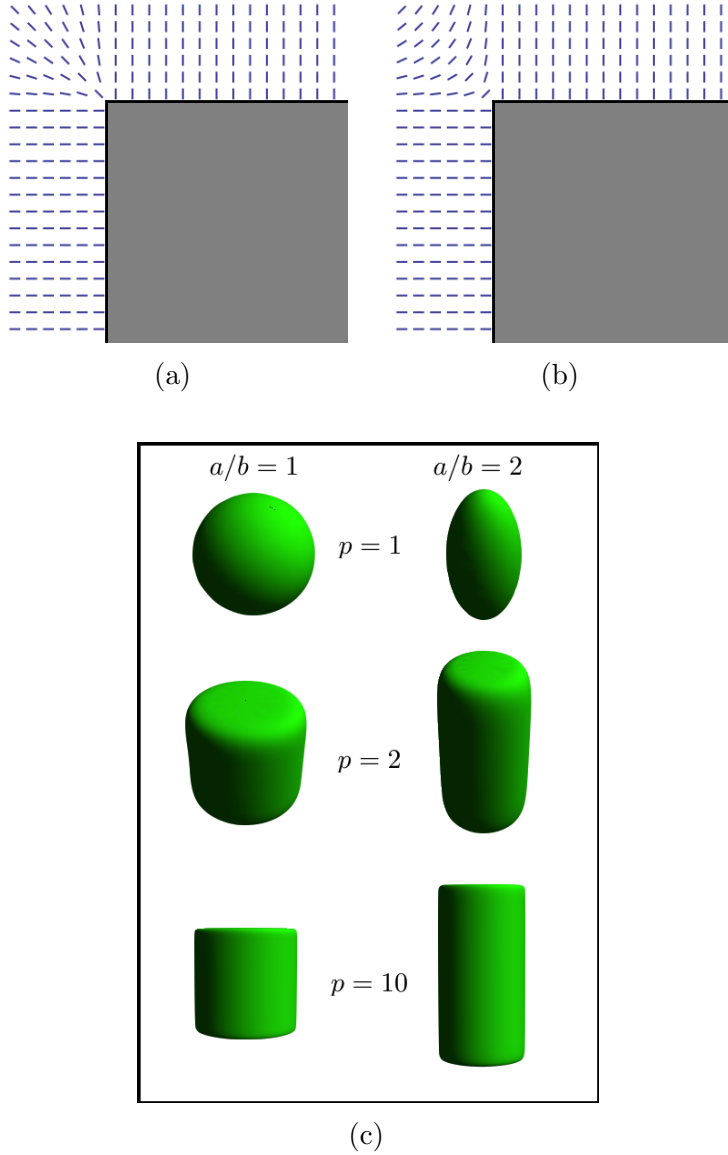


Figure 2.4: Near a sharp right-angled edge, a nematic director field can rotate by 90° either through splay (a) or bend (b). We select the more physical splay solution by modeling cylindrical colloids as supereggs of aspect ratio a/b and “sharpness” p (c).

a small region, producing more splay than anywhere else. The configuration of Fig. 2.5 represents a compromise of the disclination's splay-reducing attraction to edges with the configuration preferred by an ellipsoid in Fig. 2.3, where the ring lay in a plane perpendicular to \vec{n}_0 .

As a result, the cylinder prefers to orient with its long axis at an oblique angle ϕ_0 relative to \vec{n}_0 that increases with aspect ratio toward 90° at large a/b . For aspect ratios $a/b \gtrsim 2$, ϕ_0 is well approximated by $\tan^{-1}(a/b)$, suggesting that (at least heuristically) the energy is minimized when the separation vector between the kinked ends of the disclination lies in the plane perpendicular to \vec{n}_0 .⁵ This analytic approximation improves in accuracy as the sharpness p is increased, while the qualitative trend of ϕ_0 increasing with aspect ratio persists with decreasing p down to $p \approx 2$. For oblate cylinder shapes with aspect ratios below 1 (down to $a/b = 0.25$, the lowest tested), the kinked disclination configuration and oblique colloid orientation remain, but the positive correlation of ϕ_0 with a/b disappears. While all results presented here assume infinite anchoring strength on the colloid's surface,⁶ the same qualitative trend of ϕ_0 increasing with aspect ratio is preserved when the anchoring strength is made finite and reduced to $W = 10^{-3}$ N/m, 10% of the anchoring strength for 5CB at DMOAP-treated surfaces.

An alternative configuration, with the disclination ring encircling the colloid's short axis about its center (Fig. 2.5d), is also observed at high aspect ratio, but this state only appears when the colloid is constrained to orient at unfavorably small angles ϕ relative to \vec{n}_0 . If the aspect ratio is increased further, we expect that the

⁵These results are for confinement in a cell of thickness 3 times the colloid diameter. For stronger confinement in a cell of thickness 1.5 times the colloid diameter, the analytic approximation is less accurate, but ϕ_0 still increases monotonically with aspect ratio.

⁶The infinite anchoring strength approximation is reasonable because 5CB near DMOAP treated surfaces experiences an anchoring strength $W \approx 10^{-2}$ N/m [118], so the anchoring extrapolation length $\xi_W = K/W$ is on the order of nanometers, similar to the nematic corellation length $\xi_N \sim \sqrt{L_1/|A|} \approx 7$ nm.

core defect energy per unit length of defects will allow the short-axis disclination ring to eventually overtake the kinked long-axis disclination loop in stability, resulting in alignment of long cylindrical colloids parallel to the far-field director at $\phi = 0$. However, in the numerical results, the kinked long-axis disclination loop remains stable, with $\phi_0 \approx \tan^{-1}(a/b)$, for aspect ratios up to $a/b = 10$, the highest tested.

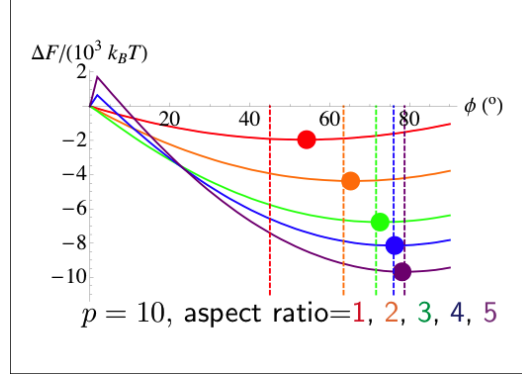
A similar result is found for microbullets (Fig. 2.6). Here, the disclination again wraps around the colloid's long axis and kinks to follow half of the circular end. At the rounded end, the disclination is nearly undeflected. The energetically preferred colloidal orientation ϕ_0 is again oblique and increases with increasing aspect ratio. At all aspect ratios tested, ϕ_0 is well approximated simply by the average of $\tan^{-1}(a/b)$ and 90° .

In Ref. [131], a wide range of cylinder orientations $35^\circ \lesssim \phi_0 \lesssim 90^\circ$ was reported for a wide range of aspect ratios $1.3 \lesssim a/b \lesssim 4.7$. The results presented here suggest that orientation and aspect ratio ought to be correlated, and moreover that controlling particle aspect ratio and corner sharpness offers a means of tuning the preferred colloidal alignment.

2.4.4 Pair potentials for colloidal cylinders

Another consequence of the disclination configuration found above is that there are actually two equivalent ground states: that of Fig. 2.5b,c/Fig. 2.6b and its mirror image reflected through \vec{n}_0 , as shown in Fig. 2.7. We now wish to calculate pair potentials for colloidal cylinders in the thin planar cell geometry, but we must keep in mind these two equivalent ground states for isolated cylinders.

To begin to understand how the effect of sharp edges on individual colloidal orientation affects the properties of colloidal assembly, we seek to calculate the energy



(a)

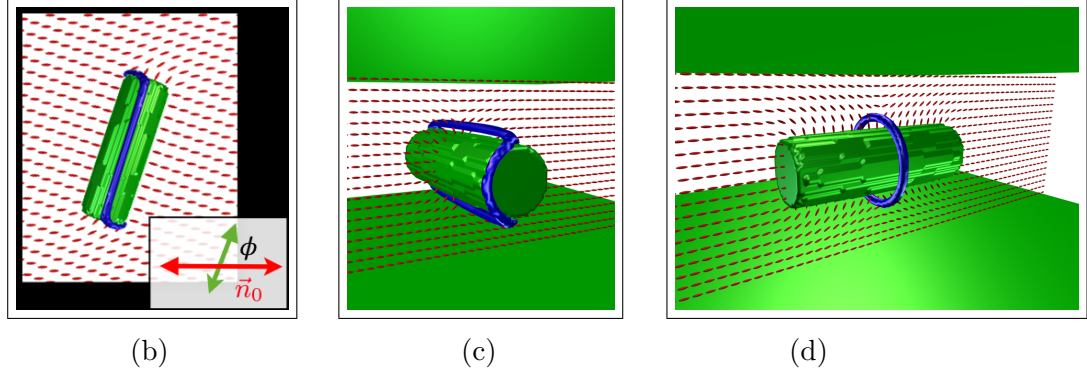


Figure 2.5: (a) Free energy of a colloidal cylinder (diameter $0.2 \mu\text{m}$, sharpness parameter $p = 10$), modeled as a superegg, in a planar nematic cell (thickness $0.6 \mu\text{m}$) with strong unidirectional planar anchoring, as a function of the angle ϕ between the cylinder's long axis and the far-field director \vec{n}_0 . The disclination ring wraps around the long axis of the colloid but is kinked into an “S”-shaped configuration at the cylinder’s ends to follow the sharp edges (b, c). As a result, the colloid prefers to orient obliquely relative to \vec{n}_0 at angles ϕ_0 marked by disks in (a). These angles depend on the aspect ratio a/b and, for $a/b \gtrsim 2$, are well approximated by $\phi_0 = \tan^{-1}(a/b)$, shown as the dashed lines in (a). An alternative disclination arrangement shown in (d) is responsible for the sharp peaks at small ϕ for aspect ratios 4 and 5 in (a).

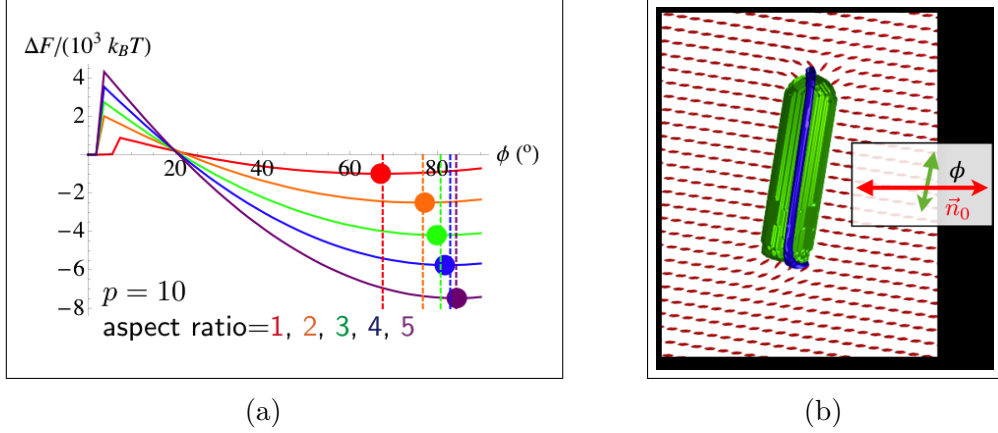


Figure 2.6: (a) Free energy of a microbullet (diameter $0.2 \mu\text{m}$, sharpness parameter $p = 10$) with various aspect ratios a/b in a planar nematic cell (thickness $0.6 \mu\text{m}$) with strong unidirectional planar anchoring, as a function of the angle ϕ between the cylinder's long axis and the far-field director \vec{n}_0 . Colored disks show the energy-minimizing angle ϕ_0 for each aspect ratio, which is well approximated by $\phi_0 = \frac{1}{2} (90^\circ + \tan^{-1}(a/b))$, shown as the dashed lines. (b) The disclination ring wraps around the long axis but is kinked at the flat end of the microbullet where there is a sharp edge.

of pairs of cylindrical colloids. In principle, this requires varying not only the separation of the two colloids but also the orientation of each one. To reduce the number of variables, we assume that both cylinders remain in the ground state orientation of an isolated cylinder. The remaining variables are the distance and angle of the cylinders' center-to-center separation, as well as the choice of equivalent or mirror-image ground states for the colloidal pair.

The pair potential for two cylinders in the same ground state is shown in Fig. 2.8. These cylinders attract end-to-end, as shown by the decrease in energy with decreasing center-to-center separation distance as the cylinders, oriented at angle ϕ_0 , approach along a separation angle $\phi_{\text{sep}} = \phi_0$ relative to \vec{n}_0 . This result predicts end-to-end chaining for a series of cylinders in the equivalent ground state orientation. Whether a chain of cylinders remains oriented at an angle ϕ_0 relative to \vec{n}_0 is an open question. Preliminary data suggests a chained cylinder pair can lower its energy by acting as a

single cylinder of twice the length and therefore twice the aspect ratio of the original cylinders individually, such that the final state contains a single kinked disclination loop; the colloidal chain then prefers to reorient at the larger angle (relative to \vec{n}_0) preferred by a cylinder with the higher aspect ratio. However, there may be a significant energy barrier to such a rearrangement of two disclination loops into one, just as the entangling of spherical colloids requires an input of energy, typically from laser tweezers, to melt the nematic locally [106]. Therefore, it remains an open question whether long chains of cylinders orient obliquely relative to \vec{n}_0 . Meanwhile, the two cylinders in Fig. 2.8 repel at two angles near $\phi_{\text{sep}} = \phi_0$, corresponding to the configurations shown in Fig. 2.8 where the cylindrical edge half with (without) a disclination running along it approaches an edge half on the other cylinder likewise with (without) a disclination.

The pair potential changes drastically when the two cylinders are in the different mirror-image states (Fig. 2.9). At large distances, the cylinders repel strongly when approaching along a line perpendicular to \vec{n}_0 . However, if the cylinders are forced close enough together, one of the two disclinations switches the side of the cylinder end that it follows, replacing the “S” configuration with a “C” configuration. Thereafter, the repulsion at separation angle $\phi = 90^\circ$ is replaced with an attraction that strongly binds the two cylinders together. It is quite likely that such a switching move in an experiment would be followed by a reorientation of the cylinder to the opposite ground-state angle and a switch of the other end’s disclination kink to turn the “C” back into an “S”, after which the cylinders could assemble end to end. Also, worth noting in Fig. 2.9 is a slight attractive well corresponding to cylinder ends approaching disclination-free side to disclination-laden side.

The fact that disclinations follow the sharp edges of cylinders also has implications for colloids’ entanglement by merging of their disclinations. Such entanglement has drawn great interest for generating a variety of stable structures [106], including

hierarchical assembly of colloids of different sizes [119] and a wide array of defect knots and links in colloid lattices [132]. An entangled state of two equal-size spheres is shown in Fig. 2.10a, where a “twist cell” geometry with 90° offset between rubbing (anchoring) directions at the top and bottom surfaces is used to stabilize the entanglement. A pair of entangled cylinders is shown in the same twist cell geometry in Fig. 2.10b. As with individual cylinders, the disclination travels in a straight line (roughly) along the long axis of the cylinder and then follows a portion of the sharp edge at the cylinder end before traversing to the end edge of the other cylinder.

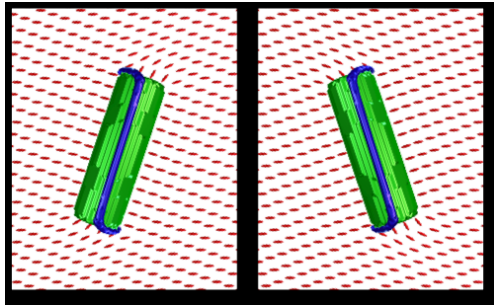


Figure 2.7: The two mirror-image ground states of a colloidal cylinder.

2.4.5 Colloidal cubes

In going from ellipsoids to cylinders and microbullets, we found that adding an edge or two created a new realignment effect with significant consequences for colloidal assembly. What will happen then, if the colloids are cuboidal, with twelve edges? Now there exist a multitude of ways for a disclination to wrap around the colloid by following only edges!

We again want to round out the edges slightly to ensure that the boundary conditions impose splay rather than bend on the director field. This is accomplished

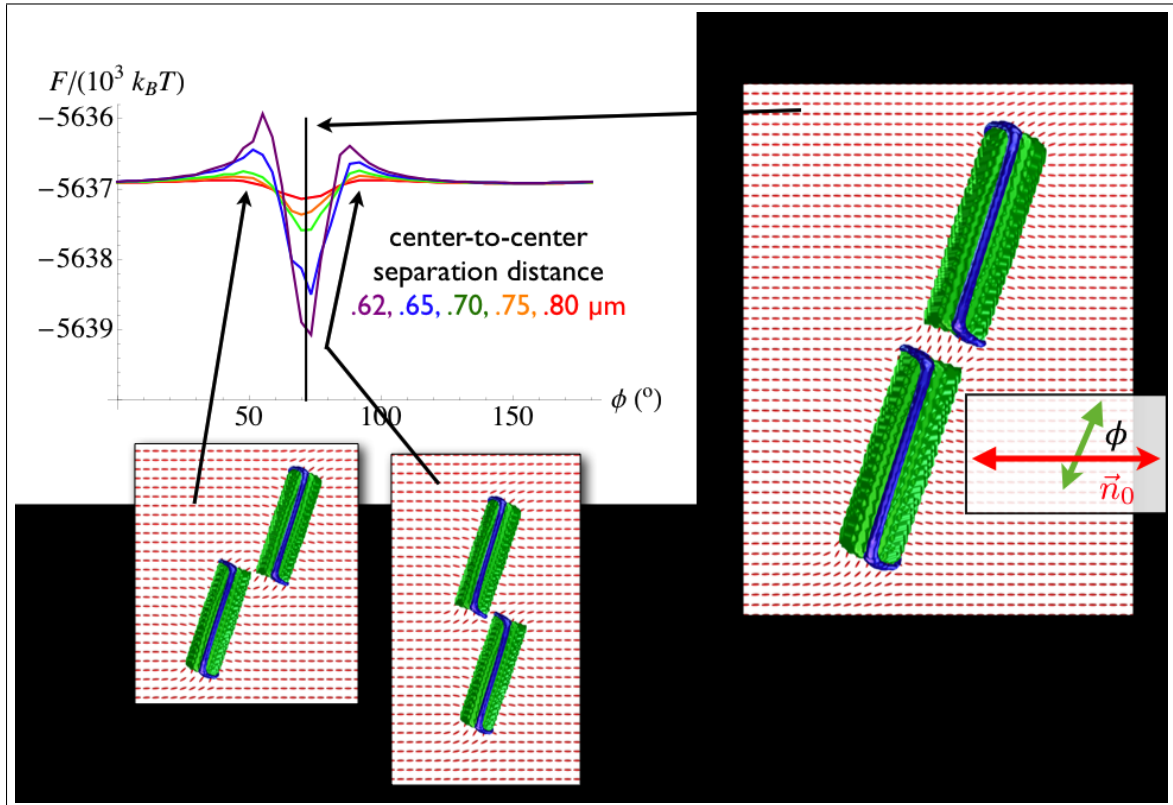


Figure 2.8: Pair potential for two colloidal cylinders in the same one-cylinder ground state at various center-to-center separation distances as a function of the angle ϕ that their separation vector makes with the far-field director \vec{n}_0 . Insets show examples of attractive (right) and repulsive (bottom left) configurations.

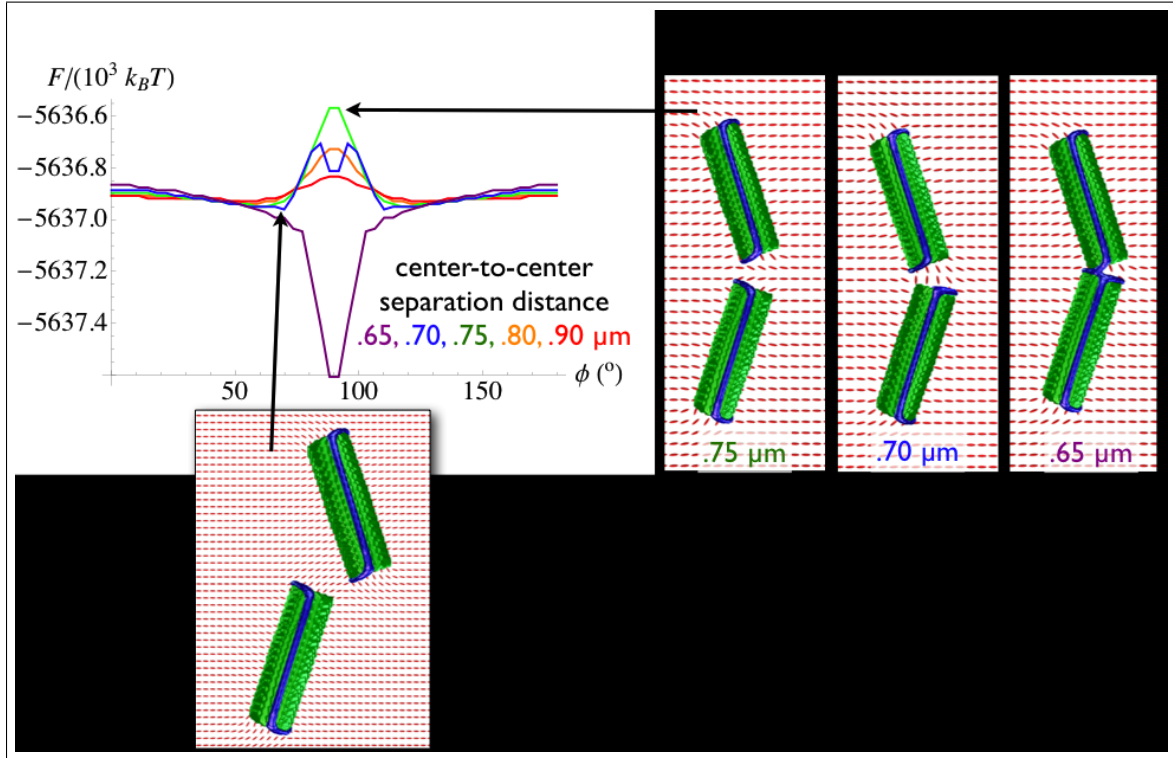


Figure 2.9: Pair potential for two colloidal cylinders in opposite mirror-symmetric one-cylinder ground states at various center-to-center separation distances as a function of the angle ϕ that their separation vector makes with the far-field director \vec{n}_0 . Insets show examples of attractive and repulsive configurations. At $\phi = 90^\circ$, a repulsive interaction at long distances becomes attractive at short distances after one disclination kink switches sides.

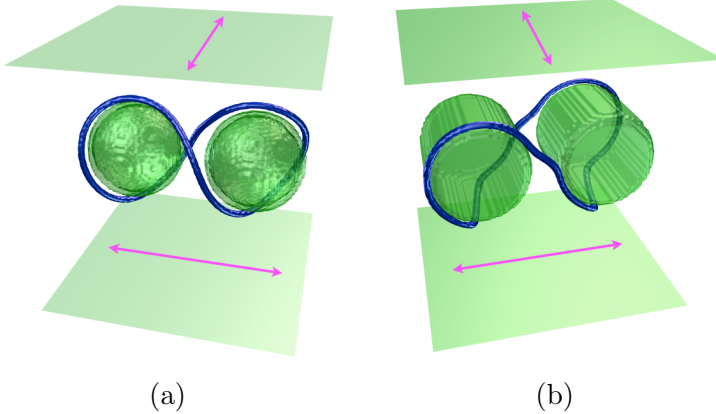


Figure 2.10: A pair of entangled colloidal spheres (a) and cylinders (b) in a nematic twist cell with alignment directions at the two surfaces shown as pink arrows. The colloid diameter is $0.2 \mu\text{m}$ in both cases. The boundary conditions are periodic in the lateral directions. For the cylinders, the aspect ratio is 1 and the sharpness parameter $p = 5$.

with the superellipsoid equation:

$$\left(\frac{x^2}{b^2}\right)^p + \left(\frac{y^2}{b^2}\right)^p + \left(\frac{z^2}{a^2}\right)^p = 1 \quad (2.32)$$

Again, the coordinates have been rotated so that the colloid long axis is the z -axis; the aspect ratio is given by a/b where a is half the cuboid length. For simplicity we investigate only $a/b = 1$. Here, the “sharpness” p interpolates the shape between an ellipsoid (a sphere for $a/b = 1$) at $p = 1$ and a rectangular cuboid (a cube at $a/b = 1$) as $p \rightarrow \infty$.

We assume that two of the cube’s faces have normals in the vertical direction. As with the ellipsoids, cylinders, and microbullets above, the cube is then rotated about the z -axis to find the orientation that minimizes the free energy. We find that the cube prefers to have the normals of its side faces oriented at 45° relative to \vec{n}_0 . The disclination wraps around six of the colloid’s twelve edges, dividing three faces

from the other three, in one of the configurations shown in Fig. 2.11b. (The sharpness parameter used in this case is $p = 3$.)

The multiplicity of possible disclination arrangements has a peculiar consequence: snap-through reconfiguration of the disclination ring when the cube is rotated. To see this, we conduct LdG energy minimization at an initial cube orientation, then rotate the cube by small increments, re-minimizing the energy after each increment. (Actually, we rotate \vec{n}_0 and leave the cube fixed, but the two processes are physically equivalent.) This models a quasi-static rotation of the colloid relative to fixed anchoring conditions at the top and bottom surfaces. The result, shown in Fig. 2.11a, is that the elastic stress builds up until a sudden rearrangement of the disclination to a set of edges more compatible with the new cube orientation, leading to a sharp drop-off in energy. Increasing the sharpness parameter p delays the defect rearrangement and increases the amount of elastic energy that builds up before the switch occurs. Upon further rotation, the cube keeps the same disclination arrangement through an energy minimum with ϕ at odd multiples of 45° before the elastic energy builds up again, leading to another snap-through defect reorganization. A similar but less drastic snap-through defect reconfiguration also occurs for cylindrical colloids, between the two mirror-symmetric configurations mentioned previously.

Generally, the disclination around a cubical colloid always follows two horizontal edges of the bottom face, two vertical edges on opposite sides of the cube, and two horizontal edges of the top face. The vertical edges chosen by the disclination lie roughly in the plane perpendicular to \vec{n}_0 . This leaves two choices of edge pairs for each of the top and bottom faces, but the defect ring always makes the opposite choice at the top face compared to the bottom. There are thus four disclination arrangements exhibited by the cube, as shown in the first four panels of Fig. 2.11b. Very sharp edges on the cube slightly modify these defect configurations with a peculiar waviness, as

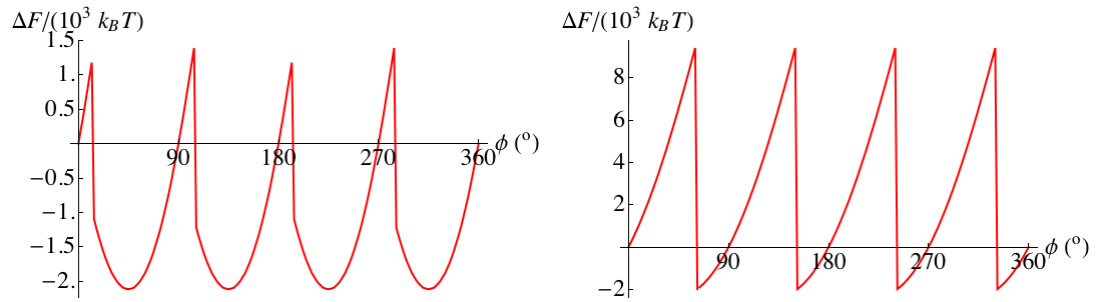
the disclination appears to avoid the *vertices* of the cube (last panel of Fig. 2.11b).

Pair potentials for colloidal cubes are shown in Fig. 2.12. As for pairs of cylinders above, the colloid orientations are fixed in the single-cube ground state, with the faces' normals at 45° angles to \vec{n}_0 . The interaction here is simple but interesting: Cubes attract face-to-face but repel edge-to-edge.

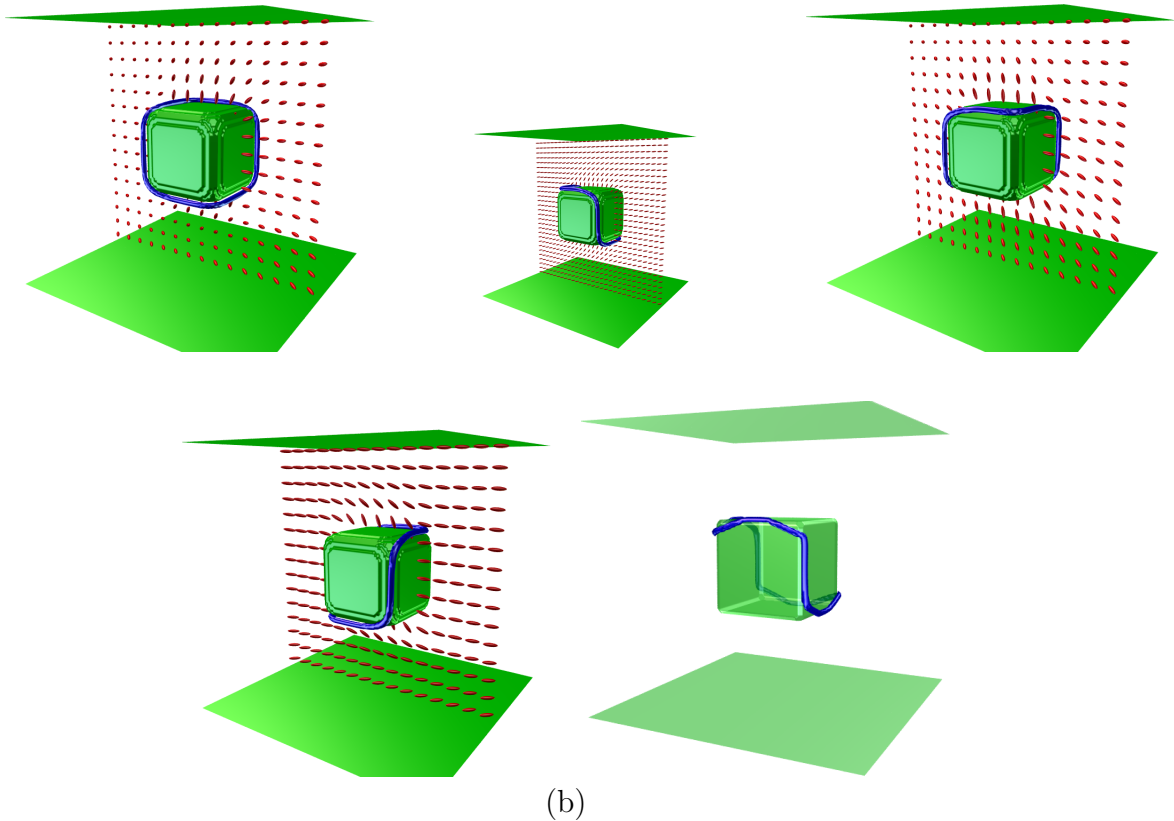
2.4.6 Summary and future work

Through Landau-de Gennes numerical modeling of anisotropic homeotropic colloids, we have found that colloid shape, and in particular the presence of sharp edges, has a remarkable effect in reshaping the companion disclination ring. The disclination executes sharp turns in order to follow the edges so as to alleviate the elastic energy cost of splay at the edges required by strong homeotropic anchoring. While it would at first seem to be only a microscopic effect, the defect's attraction to edges leads to a realignment of the colloid relative to the background director field. This predicted realignment offers an explanation for the experimentally observed oblique orientation of colloidal cylinders and microbullets in thin cell nematics. The colloidal realignment in turn affects the geometry of colloidal assembly, as colloids tend to attract along the directions normal to the faces with sharp edges. We also predict sudden changes in defect arrangement as the colloid is rotated relative to the far-field director, or as colloids are forced together along a repulsive direction.

Lithographic techniques are advanced enough to provide fairly precise control over the aspect ratio and edge sharpness of colloidal microbullets, and possibly cylinders as well. Experiments are underway to test these predictions at the time of this writing. The snap-through defect rearrangements predicted for rotating and translating colloids can likely be tested with the use of laser tweezers.



(a)



(b)

Figure 2.11: (a) Change in free energy as a cubical colloid is rotated about a vertical line through its center by angle ϕ , after numerically minimizing the energy with each incremental rotation. The cube is $0.4 \mu\text{m}$ on each side; the planar cell is $1.2 \mu\text{m}$ thick. Left: sharpness parameter $p = 3$. Right: $p = 10$. The disclination cycles through four possible arrangements, shown in the first four panels of (b) for the $p = 3$ case. The last panel of (b) shows one configuration for the cube with $p = 10$.

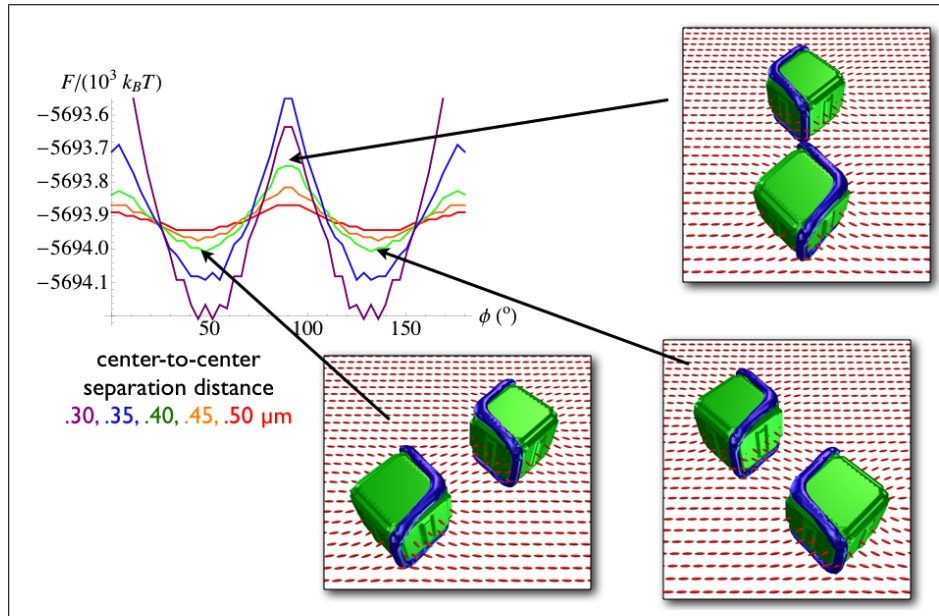


Figure 2.12: Pair potential for colloidal cubes, oriented with their side faces at $\pm 45^\circ$ to the far-field director \vec{n}_0 , as a function of the angle ϕ that their separation vector makes with \vec{n}_0 . Insets show examples of the most attractive and most repulsive cube arrangements at $\phi = 45^\circ$, 135° , and 90° . Cubes are $0.2 \mu\text{m}$ on each side with sharpness parameter $p = 3$; the cell has thickness $0.6 \mu\text{m}$.

Future numerical work will proceed in three key directions. First, pairs of colloids will be replaced with chains and lattices to test various self-assembly outcomes. Snap-through defect rearrangement could be especially important here in developing multistable systems. Second, the interactions of colloids with different sizes and shapes will be studied to determine the potential for new hierarchical self-assemblies, just as disclination entanglement led to hierarchical assembly of differently-sized spheres [119]. Third, colloid shapes of increased complexity will be investigated to determine the geometric possibilities offered by disclinations effectively confined to a one-dimensional subset of a three-dimensional system—a prospect that suggests exciting connections to topology. All of these areas of investigation will further the key finding presented in this section: Colloidal assembly and alignment in nematic liquid crystals are highly sensitive to details of colloid shape, offering a route to tunable effective colloid interactions and an expanded library of self-assembly outcomes.

2.5 Disclinations in nematic liquid crystals in micropost confining geometries

2.5.1 Introduction

Classically, the bulk of a material system is where the action is: the interface is oft relegated to a set of “boundary conditions.” However, crystal faceting [136], the quantum hall effect [130], and even the AdS-CFT correspondence [2] fundamentally reverse this relationship—the bulk properties can be read off from their effects on the boundaries. In this section, we demonstrate migration and organization of colloids constrained to a liquid crystal-air interface, driven remotely by the elastic distortion created by the presence of topological defects in the liquid crystalline bulk. We examine

experimental results in a nematic liquid crystalline system confined in a micropost geometry, meaning a thin film of nematic on a substrate topographically patterned with cylindrical microposts. A disclination ring is observed to form consistently in the bulk of the liquid crystal 5CB around each micropost in the experiment. Colloidal spheres on the interface experience an attraction to the regions above the submerged defects, as well as an elastic repulsion from each other, leading to complex new assemblies. The long range of these elastic interactions allows defects in the bulk nematic phase far below the interface to direct assembly at the interface. Other recent work on producing ordered arrangements of particles at liquid crystal interfaces beyond simple triangular lattices—such as chains [46], stripes [91], and dense quasihexagonal lattices [97]—has focused on confining the nematic in thin film or droplet geometries and varying the surface coverage fraction. In these experiments, sensitive control over substrate topography provides the ability to tune the defects’ positions and their influence on the interface, offering a route to tunable non-trivial colloidal assemblies.

To understand how topological defects in the bulk drive complex assembly at the boundary, in this section we use theoretical tools to examine both the appearance of bulk disclination rings in the micropost geometry and the attraction of colloids at the surface to the bulk disclinations below. We begin with a description of the experimental setup and microscopy results, along with an analytic approximation to broadly characterize the defect complexion. We corroborate this approach with Landau-de Gennes numerical modeling and find that, surprisingly, the connection between the boundary conditions and the substrate topography is not always entirely geometric. Finally, we study the migration and arrangement of colloids at the surface in response to disclinations in the bulk, and again gain insights through LdG numerical modeling.

2.5.2 Experimental setup and results

A square array of cylindrical microposts is prepared, with homeotropic anchoring imposed at all surfaces. A thin film of the nematic liquid crystal 5CB is deposited on this substrate, with its top surface exposed to air. As a result, a circular disclination ring appears around each micropost. The defect lines encircle the microposts and appear as bright lines in an otherwise black polarized optical micrograph shown in Fig. 2.13a. Under sample rotation, the dark regions remain black, confirming homeotropic anchoring, while bright field optical microscopy corroborates this observation (inset of Fig. 2.13a). When the sample is heated above the clearing point ($T_{NI} = 34^\circ\text{C}$), the defect line is absorbed into the isotropic phase, resulting in a completely black image under crossed polarizers. Upon cooling back to the nematic phase (either slowly at $0.1^\circ\text{C}/\text{min}$ or in contact with the room environment), the disclination reappears, confirming that the texture is due to the equilibrium elasticity of the nematic liquid crystal and the frustrated director field near the surface of the micropost. Fluorescence confocal polarizing microscopy (FCPM) is used to determine the vertical position of the disclination line, showing that, for a wide range of post heights, the disclination occurs near the mid-height position (Fig. 2.13b). In addition, FCPM results indicate that the disclination's lateral separation from the micropost surface is within $5\ \mu\text{m}$.⁷ Finally, varying the cross sectional shape of the microposts demonstrates that the disclination line bears the signature of the micropost shape as shown in Fig. 2.13c.

⁷Though both bright field and polarized microscopy suggest a larger gap between the posts and defects, this is believed to be an optical effect due to the curved interface and the birefringence of the LC.

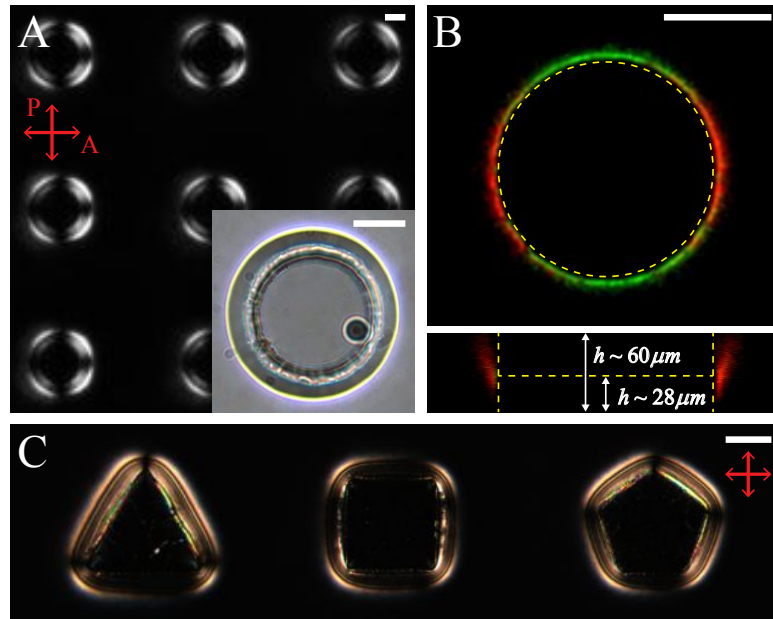


Figure 2.13: Micropost-induced bulk defect rings. (a) Polarized optical microscopy (POM) image of a micropost array where all surfaces have homeotropic anchoring resulting in defect rings that circumscribe each micropost. INSET: Bright field image of a single micropost where the bright line indicates the approximate lateral position of the defect loop. (b) Fluorescence confocal polarization microscopy (FCPM) image indicating the location of defects in an otherwise uniform director field. Top: A top view of the micropost. Bottom: A z-stack of FCPM images in which the maximum intensity represents the location of the defect core that occurs at approximately the post mid-height. (c) Disclination lines are dictated by the shape of the micropost as shown around triangular, square and pentagonal microposts. All scale bars are $50 \mu\text{m}$. Red arrows mark the polarizer and analyzer directions in POM images. [19]

2.5.3 Landau-de Gennes numerical modeling of bulk disclination ring

What does the observed disclination ring imply about the bulk director field and the boundary conditions associated with confinement? To address this theoretically, we use LdG numerical modeling to study nematic 5CB in micropost confining geometries, examining both the calculated director field and disclinations. In this section we use the unequal elastic constants measured for the elastic anisotropy of 5CB, abandoning the one-elastic-constant approximation in order to most accurately model the experiment. The elastic constant values are $L_1 = 3.8 \times 10^{-12}$ N, $L_2 = 5.3 \times 10^{-12}$ N, and $L_3 = 5.3 \times 10^{-12}$ N, which are used to model 5CB with elastic constants $K_1 = 0.64 \times 10^{-11}$ N, $K_2 = 0.3 \times 10^{-11}$ N, $K_3 = 1 \times 10^{-11}$ N [70] (see Appendix A for relations between L_i and K_j constants). The mesh spacing corresponds to 4.4 nm. The microposts modeled have diameter 440 nm and height 264 nm. The simulation box has length 1320 nm in both horizontal dimensions. We model the anchoring strength on all the substrate surfaces as infinite by imposing a fixed, uniaxial \mathbf{Q} at the boundaries. We have verified that finite anchoring strength in the strong anchoring regime does not significantly change the results using a Rapini-Papoulier-type surface potential as used in Ref. [108]. Periodic boundary conditions in the horizontal directions are used to simulate a square array of microposts.

The micropost is modeled as a right cylinder bridging two planar interfaces. We find four distinct local minima of the free energy: two in which there is no defect in the bulk (Fig. 2.14b and its reflection through the horizontal), one with a disclination ring around the micropost with $+1/2$ winding geometry (Fig. 2.14c), and one in which the disclination ring has instead a $-1/2$ geometry (Fig. 2.14d). All the minima exhibit axial symmetry and we find that the director field has no axial component as in Fig.

2.14b-d. It follows that we can discuss the topology of the texture in terms of *two-dimensional* nematics corresponding to each radial slice, promoting the $\pm 1/2$ geometry into a pseudo-topological charge. The disclination ring is topologically charged in the three-dimensional sense, as the director field profile is essentially constant along its contour [5, 29, 55]; we will henceforth focus exclusively on the two-dimensional pseudo-charge.

The total pseudo-charge can be calculated via the winding of the director around the boundary of the sample. However, as our numerics demonstrate in Fig. 2.14, the sharp corners at the cylinder-planar junctions require careful consideration of the topology in each slice. Each corner can be resolved via a splay or bend texture leading to a director rotation of $\pm\pi/2$, respectively. Thus the defect pseudo-charge in each radial slice is determined by the details of each junction. When the winding sense is positive at corner X and negative at corner Y (Fig. 2.14b) or vice versa, there is no disclination ring in the bulk. On the other hand, a disclination ring of winding number $+1/2$ (Fig. 2.14b) is predicted at mid-height around the micropost when the two corners both have positive winding. Likewise, a disclination ring of winding number $-1/2$ (Fig. 2.14c) is predicted at mid-height around the micropost when the two corners both have negative winding. Thus, the experimental observation of a disclination in the bulk implies that the director winding has the same sign at both corners. The nematic degree of order is diminished locally at the corners due to the incompatible boundary conditions. It should be noted that the computed free energies of the states with the bulk disclination ring (Figs. 2.14c and 2.14d) are slightly higher than that of the states with no bulk defect (Fig. 2.14b), whereas the bulk disclination is stable in experiment. A similar multistability due to sharp-cornered boundaries has been reported for nematics in square wells with planar anchoring [82, 134]. There, the choice of winding sense at each corner gives rise to two optically distinct states, a

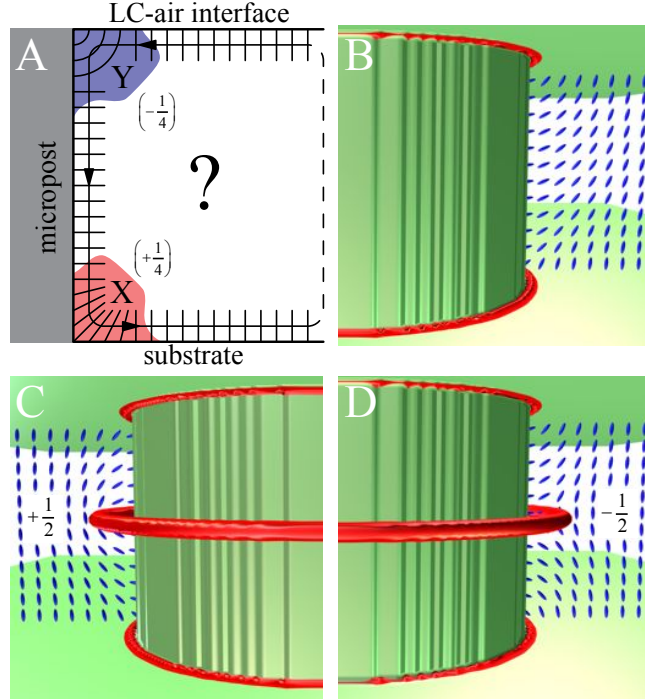


Figure 2.14: Numerical and topological evaluation of the director field. (a) The system has two corners, labeled X and Y, where the director field can choose between two winding senses. (b-d) Director fields corresponding to the relative minima of the Landau-de Gennes free energy for a cylindrical micropost and planar interfaces, found numerically. Isosurfaces of $S = 0.48$ are shown in red, where S is the leading eigenvalue of \mathbf{Q} . Blue ellipsoids indicate the director field. The nematic is locally melted at the sharp corners. (b) Opposite winding at the two corners precludes the possibility of a disclination in the bulk. (c) A bulk disclination with $+1/2$ (i.e., anticlockwise) winding number requires positive winding at both corners. (d) A bulk disclination with $-1/2$ (i.e., clockwise) winding number requires negative winding at both corners. Since the numerics show that the (meta)stable states have azimuthal symmetry and that the director has no azimuthal component, we may think of these winding numbers as pseudo-charges. [19]

useful situation for bistable displays.

In the numerical model, we can induce a local preference for a given winding sense by altering the geometry of either corner. For example, Fig. 2.15a shows a 5CB-air interface curving upward to meet the micropost at a nonzero pinning angle as in the experiment. As a result, bend is favored over splay and the winding is negative. Conversely, curvature at the bottom of the micropost favors positive winding, as shown in Fig. 2.15b. With this resolution of the sharp boundaries, the bulk disclination ring is not even metastable in the numerics. To probe this experimentally, the sharp corner at X was replaced with a curved base to favor a positive winding sense (+1/4) as in Fig. 2.15b; the surface pinning maintains the preference for negative winding at corner X. When the base of the micropost is slightly curved (Fig. 2.15c) the bulk disclination persists but is pushed away from the base, closer to the 5CB-air interface. This result is in contrast to the numerical prediction that *any* curvature at the micropost base will cause the disclination to disappear. The defect position is verified using FCPM as shown in Fig. 2.15d. Heating into the isotropic phase and re-cooling into the nematic phase several times demonstrates the stability of the defect, which re-forms upon each cooling into the nematic phase. Further, the bulk disclination remains even when the microposts are completely submerged in a thick nematic film. However, when the microposts are tapered all the way to the top (Fig. 2.15e-g), the bulk disclination ring fails to form in the experiment (Fig. 2.15f and 2.15g), as verified by FCPM, which is in agreement with the numerical results. Thus, the geometry of the boundary alone is not sufficient to predict the qualitative features of the bulk director field. We suspect that variations in surface chemistry, roughness, or relative magnitudes of anchoring strength are important for the stabilization of bulk defects. On the other hand, these findings demonstrate that sensitive control over the boundary shape offers the ability to tune the stable position of the disclination ring.

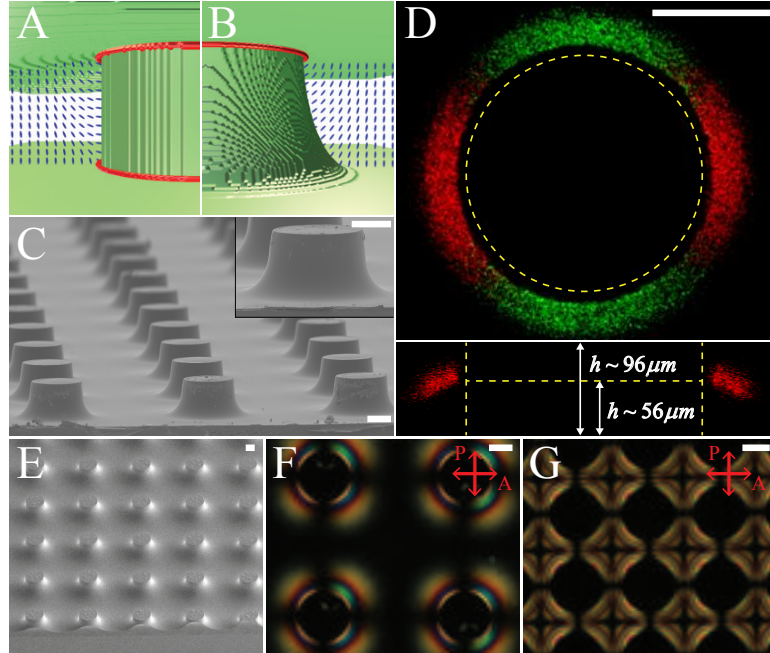


Figure 2.15: The effect of surface curvature. (a) Where the 5CB-air interface curves upward to meet the micropost, LdG numerical modeling predicts that negative winding is favored. (b) Likewise, curvature at the bottom of the micropost favors positive winding; the surface defect in this case can be viewed as virtual, inside the micropost. (c) Scanning electron microscopy (SEM) image of microposts with a curved base and a corresponding (d) FCPM image detecting the presence of a disclination loop when the micropost array is filled with LC. Typically this defect will sit toward the upper half of the micropost. (e-g) Curved microposts tapered along their entire lengths, SEM image shown in (e), do not induce the formation of a bulk disclination ring (verified with FCPM), as is evident when viewed between crossed polarizers. The relaxation of the director to the vertical direction with increasing distance from the micropost is much more gradual in (f) than in Fig. 2.13a. Axial symmetry is lost at smaller micropost spacing (g). All scale bars are $50\mu m$. [19]

As a further demonstration of the influence of boundary shape on defect configuration, we consider numerically a micropost design with an undulating profile (Fig. 2.16). Surprisingly, multiple disclination rings appear around the micropost. Their cross-sectional winding number alternates in sign, with a $-1/2$ disclination ring around the convex region and $+1/2$ disclination rings around the concave regions. In comparison with a cylindrical micropost, the curvature of the undulating micropost favors positive or negative winding of nearby disclinations in ways that are visually obvious in the figure. The stability of multiple disclinations suggests the possibility of multistable systems based on undulating microposts, with the number of disclinations alterable by application of an electric field, for example. (Note that we have been careful to curve the intersections of the micropost with both the top and bottom boundaries to avoid the $\pi/2$ ambiguities discussed above and thus isolate the effects of boundary curvature on disclinations in the bulk.)

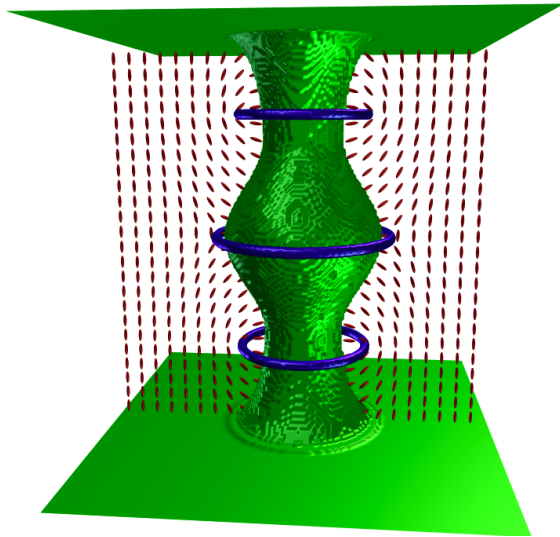


Figure 2.16: Appearance of multiple disclination rings of alternating sign around a micropost with undulating profile.

2.5.4 Effect of bulk disclination on colloidal self-assembly at an interface

Having carefully characterized the bulk nematic configuration, we now turn to the interaction of the liquid crystal with colloidal particles. Prior work has established that colloids are attracted to disclination lines, an effect that has been exploited in the bulk to form wire-like chains of colloidal particles along the defects [38, 103, 114, 118]. Here, however, we study how to use the distortion field generated by the defect to *remotely* steer particles trapped at the 5CB-air interface. Experimentally, when a $5\text{ }\mu\text{m}$ diameter silica microsphere with homeotropic anchoring is placed on the interface, it migrates radially toward the micropost until contact (Fig. 2.17a). Though capillary interactions are known to induce particle migration along curved surfaces [20], capillarity effects are absent in this system since the interfacial distortions induced by the microspheres are negligible [46, 98]. Further, when the system is heated above the nematic-isotropic transition to annihilate the disclination lines, migration is no longer observed, demonstrating that the observed migration must be orchestrated solely by the elastic director field. In other words, the elastic distortion created by the spherical particle is interacting with the bulk nematic texture. As noted in [46], however, the distortions made by the particles are quadrupolar in nature and die off rapidly away from the surface. Thus we expect that the colloids will only interact with large director deformations. In a number of experimentally tested micropost-nematic thin film geometries, colloidal migration was shown to depend on distance from the bulk disclination but not (or at best weakly) on the distortion of the interface or on nematic elastic distortion at Corner Y.

As the surface density of the microspheres is increased, a single ring of colloids around each micropost (Fig. 2.17b and 2.17c) gives way to complex structures that form

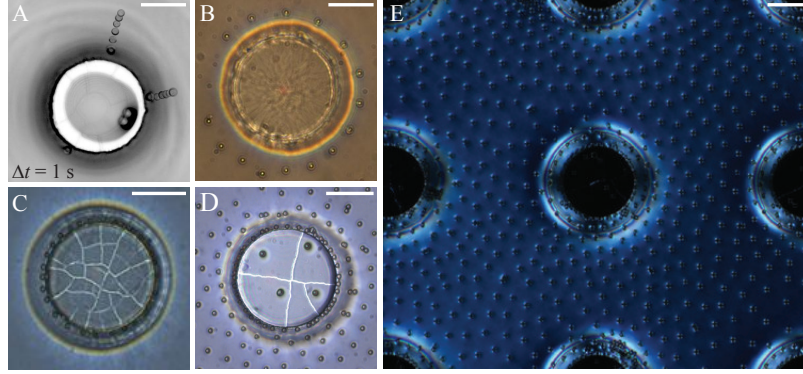


Figure 2.17: Elastic migration of colloidal particles induced by bulk topological defects. (a) Time-lapsed images of the migration of spherical colloids towards a micropost ($\Delta t = 1$ s). (b) A ring of colloids forms above a submerged micropost. (c) At moderate surface coverage, ordered rings assemble around the micropost due to attraction by the bulk defect and repel one another via long range interparticle repulsion. (d) As particle density continues to increase, radial assemblies evolve into hexagonal ordering until (e) highly complex structures form at a very high surface coverage. All scale bars are $50 \mu\text{m}$. [19]

owing to the balance of attraction to the micropost and the long-range interparticle elastic repulsion. This competition results in complex, ordered structures as shown in Fig. 2.17d and Fig. 2.17e that nucleate from the post and evolve with distance away from the post into a hexagonal lattice.

Since the particles migrate in creeping flow, the elastic potential in which they move can be estimated by balancing the elastic and viscous forces. Particle trajectories were tracked, and drag coefficients were inferred from the Brownian fluctuation of particles at the interface and the Stokes-Einstein relation. The estimated elastic interaction energies of order $E_p \approx 10^4 kT$ (Fig. 2.18a) were found to fall off as the inverse square of the radial position from the post center. We again apply LdG numerical modeling to study this attraction of colloids at the nematic-air interface to the micropost. We do this by moving a small simulated spherical colloid with a quadrupolar defect at fixed height near the top surface toward a micropost with a defect ring. As shown in Fig. 2.18b, the elastic energy is well described by $E_p = E_0 - \alpha(r - r_d)^{-2}$, where

r_d is the radius of the disclination ring around the micropost and E_0 and α are fit parameters. The dependence of this potential on distance from the disclination, rather than from the center or edge of the micropost, for example, further underscores the role of the disclination as the principal cause of the elastic attraction.

2.5.5 Summary

We have demonstrated that bulk defects can be generated in confined liquid crystals and can guide the assembly of remote colloidal particles into ordered structures through nematic elasticity. The colloids assemble to mimic the defect structure in the bulk, in this case, a ring around the micropost. At high surface coverage, attraction to the defect ring is coupled with long-range interparticle repulsion and leads to highly ordered structures that nucleate radially outward from microposts. LdG numerical modeling has been applied to shed light on the important relationship between the existence of a disclination around each micropost in the bulk of the nematic and the nematic director field at the corners where the microposts meet the interfaces. The inverse square dependence of the surface colloids' elastic attraction to the microposts was also verified in LdG numerical modeling, which highlights the relevant distance as the colloids' lateral separation the disclination itself. Coupled with the ability to manipulate the nematic director through flow, fields, and functionalization, these results paves the way to dynamically tunable assemblies at fluid interfaces.

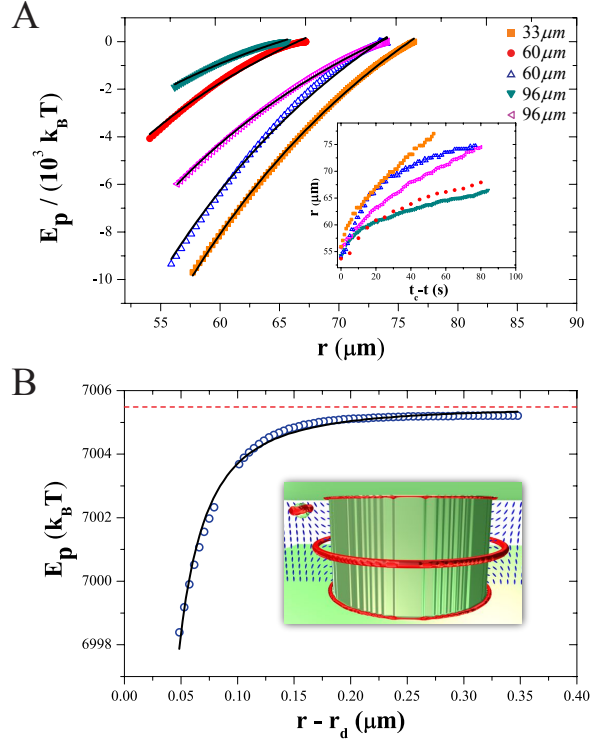


Figure 2.18: Elastic potential. (a) Migration of colloids implies bulk-colloid interaction energies on the order of $1 \times 10^4 kT$ and follow $E_p \propto r^{-2}$ (solid curves), where E_p is the inferred elastic potential and r is the radial distance in the horizontal plane from the center of the micropost. As the height of a micropost is increased (different curves), attractions become weaker due to an increased separation between particles and the bulk defect. INSET: Migration rates are faster for microposts with base curvature compared to those of comparable height that have a sharp corner at the base (corner Y in Fig. 2.14a). This is due to the tendency of the bulk disclination to position itself closer to the free interface for microposts with curved bases. Closed (open) symbols: microposts with (without) curved base. (b) Numerically modeled energy of a colloidal sphere approaching a micropost capturing the $E_p \propto (r - r_d)^{-2}$ dependence of the quadrupolar colloid interacting with a disclination ring. The red dashed line represents the asymptotic value for E_p at large distances and r_d is the radius of the micropost's disclination ring. INSET: Representative image of the numerical modeling. [19]

Chapter 3

Cusps and disclinations in 2D smectics on piecewise developable surfaces

3.1 Introduction and summary

Dramatic progress has been made in algorithmic origami; it is now possible to design nearly arbitrary three-dimensional constructions out of unstretched [73] or *nearly* unstretched [31] plaquettes, isometric to pieces of the Euclidean two-plane. At the same time, there has been theoretical and technological interest in crystalline and liquid crystalline order on curved substrates [15, 56, 101, 135, 137]. The latter problem can be studied in reduced complexity by considering surfaces with vanishing Gaussian curvature except at isolated points and curves. Were we to consider only intrinsic interactions between the substrate and the ordered phase, it follows that the in-plane positional and orientational order would be completely determined by the folds and conical points of the substrate. The connection between smectic textures, geometric optics [57, 111, 137], and shocks [7] on flat and curved surfaces makes studies of the smectic phase amenable to exact analytic study [6, 110] while capturing the salient features of broken translational and rotational invariance [23]. Combined with the



Figure 3.1: Substrates with conical defects. Notice that all of these surfaces are intrinsically flat almost everywhere—they fail to be flat at points and lines only. [92]

simplified geometries we consider, we are led to highly tractable models of order on curved backgrounds.

Here we study equally-spaced smectic textures on infinite cones, cones intersecting with planes, and cones intersecting with cones, the latter two standing in for simple bumps on surfaces and saddle-like regions, respectively; see Fig. 3.1. Not only do we see the occurrence of focal lines and cusps in the ensuing smectic textures in Section 3.2, but we also see violations of the rules that usually govern the schlieren textures of the sample in Section 3.3. Recall that curved geometry interacts with topological defects [9] to alter the conservation of topological charge in much the same way the background intrinsic curvature changes the rules for the sum of the interior angles of a triangle. In the case of schlieren textures in flat geometries, defects mark the confluence of an even number of dark brushes. However, even this simple counting rule is violated on curved surfaces, as we will demonstrate. In Section 3.4, we develop additional rules for equally spaced smectic layers on substrates with both conical points and linear folds.

We commence with a cone C embedded in \mathbb{R}^3 . C is a singular surface which has zero Gaussian curvature everywhere except at its apex, where all the Gaussian curvature is concentrated. The geometry of C may be conveniently examined by cutting the cone along a radial line L and laying it flat on a plane (Fig. 3.2). This way, C looks like a disk with a circular sector of angle δ removed and with its two straight edges identified. The angle δ is called the deficit angle. A direct application

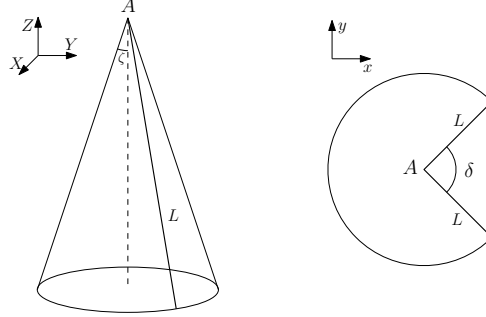


Figure 3.2: A cone is isometric to a cut planar disk with two radial lines (denoted by L above) identified. The point A is the apex of the cone. [92]

of the Gauss-Bonnet Theorem shows that δ is also the total Gaussian curvature of any region of the cone which contains its apex.

In order to establish notation, let X, Y, Z and x, y be Cartesian coordinates as in Fig. 3.2. A parameterization of C is given by:

$$X(R, \Phi) = R \cos \Phi \sin \zeta,$$

$$Y(R, \Phi) = R \sin \Phi \sin \zeta,$$

$$Z(R, \Phi) = -R \cos \zeta,$$

where, as can be easily seen, the apex angle 2ζ is related to δ by $\sin \zeta = \frac{2\pi - \delta}{2\pi}$. In terms of x, y (see Fig. 3.2) and their polar coordinates, $r = \sqrt{x^2 + y^2}$ and $\tan \phi = y/x$, we have

$$\begin{aligned} R &= r, \\ \Phi &= \left(\phi - \frac{\delta}{2} \right) \csc \zeta. \end{aligned} \tag{3.1}$$

3.2 Building the layers

A necessary condition for the layers to be uniformly spaced is that their normal vector field points along geodesics of the surface [1, 12, 57, 111]. In the flattened model, these geodesics are just the straight lines of the plane. We know that defects (even in flat space) tend to concentrate on lower dimensional sets in order to save energy so, in a 2-dimensional surface, this means that point defects are favored and this gives rise to layered structures in the form of wavefronts emanating from a point. Note that the case where this point is taken to infinity formally corresponds to a defect free configuration. We are thus led to consider a wavefront starting at some point P_0 , whose corresponding point p_0 on the cut disk lies at a distance r_0 from the disk center, which maps to the cone apex. Experimentally, this scenario can be created deliberately with a colloidal particle that induces homeotropic anchoring for the molecules of the liquid crystal. We can always cut the cone so that L is exactly opposed to P_0 and then choose coordinates such that L lies in the XZ plane. By doing so, we have $p_0 = (-r_0, 0)$. The geodesic “light rays” may then be parameterized by $x(\lambda) = -r_0 + \lambda \cos \omega$, $y(\lambda) = \lambda \sin \omega$; see Fig. 3.3. Whereas computing the geodesics on a generic surface is nontrivial, for a conical substrate we have a simple analytic mapping of straight lines on the cut disk to geodesics on the cone. The associated smectic layers are concentric circles centered at p_0 . Note that we could choose the cut L along any direction we like as long as we identify the two edges. Were we to do so, when a straight line in the *flattened* model hits one of these cuts, we would continue it with a straight line emanating from the other cut, making the same angle with the new edge. This ensures that the geodesics remain straight and demonstrates that the smectic texture is independent of the choice of L . The presence of any cusps or grain boundaries in the smectic does not result from the flattened geometry—all this

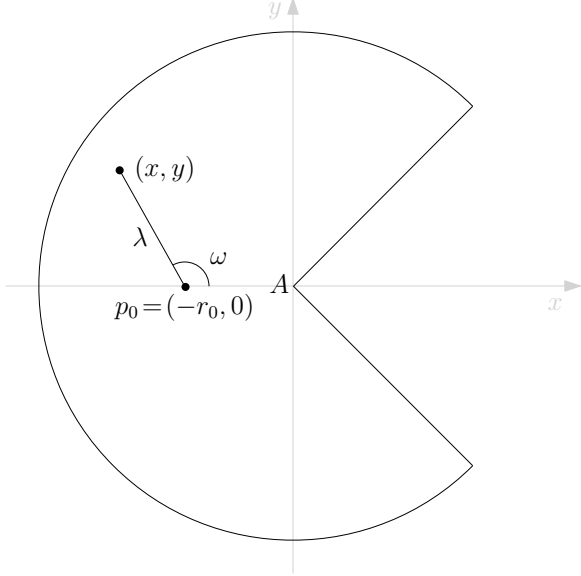


Figure 3.3: Cut-disk view of the cone, showing a parameterization of geodesics emanating from a point disclination. [92]

could be computed directly on the cone, for instance. Note that we could, alternatively, construct geodesics on a (full) two-disk, parameterized by X and Y with induced metric:

$$ds^2 = \left[\left(1 + \cot^2 \zeta \frac{X^2}{X^2 + Y^2} \right) dX^2 + \cot^2 \zeta \frac{2XY}{X^2 + Y^2} dXdY + \left(1 + \cot^2 \zeta \frac{Y^2}{X^2 + Y^2} \right) dY^2 \right]. \quad (3.2)$$

Let $X(\lambda), Y(\lambda), Z(\lambda)$ be the coordinates on the cone of the geodesics defined above. A straightforward calculation shows that

$$\begin{bmatrix} \dot{X}(\lambda) \\ \dot{Y}(\lambda) \\ \dot{Z}(\lambda) \end{bmatrix} = k \begin{bmatrix} \cos \Psi X + \sin \Psi Y \\ -\sin \Psi X + \cos \Psi Y \\ \cos \Psi Z \end{bmatrix}, \quad (3.3)$$

where

$$k = \frac{\sin^2 \zeta}{X^2 + Y^2} \sqrt{(\lambda - r_0 \cos \omega)^2 + \left(\frac{r_0 \sin \omega}{\sin \zeta} \right)^2}, \quad (3.4)$$

$$\Psi = \arctan \left(\frac{r_0 \sin \omega}{(\lambda - r_0 \cos \omega) \sin \zeta} \right). \quad (3.5)$$

The unit vector field obtained after normalizing this expression is given by

$$N = \frac{1}{\sqrt{1 + \cot^2 \zeta \cos^2 \Psi}} \begin{bmatrix} \cos(\Phi - \Psi) \\ \sin(\Phi - \Psi) \\ -\cos \Psi \cot \zeta \end{bmatrix}. \quad (3.6)$$

Therefore, the projection of N onto the XY plane makes an oriented angle $\Phi - \Psi$ with the X axis (note that Ψ depends on X and Y through λ and ω (Fig. 3.3)). The corresponding vector in the XY plane points along the unit direction

$$N_p = \begin{bmatrix} \cos(\Phi - \Psi) \\ \sin(\Phi - \Psi) \end{bmatrix}. \quad (3.7)$$

The projected layers can also be directly obtained in these coordinates by drawing lines which are everywhere perpendicular to N_p , with respect to the induced cone metric (3.2). Thus, a single prescribed defect, together with the constraint of equal layer spacing, uniquely determines the layer structure everywhere.

Alternatively, we can compute the layers as the level sets of a function $D(P)$ that measures the distance from a given point P to the wavefront source P_0 . If the cut line L is appropriately chosen (so that it contains P_0 , for example), the distance between two points $P = (X, Y, Z)$ and $P_0 = (X_0, Y_0, Z_0)$ on the cone is just the planar distance between their counterparts $p = (x, y)$ and $p_0 = (x_0, y_0)$ on the cut disk. In terms of

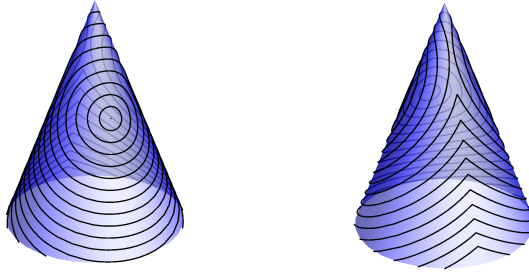


Figure 3.4: Layer structure on the 3D cone for a deficit angle $\delta = 5\pi/4$. The image on the right shows the back of the image on the left and *vice versa*. [92]

the coordinates R, Φ (see Eq. (3.1)), this yields

$$\begin{aligned} D(P) &= \sqrt{(x + r_0)^2 + y^2} \\ &= \sqrt{R^2 + r_0^2 + 2r_0 R \cos\left(\frac{\delta}{2} + \Phi \sin \zeta\right)}. \end{aligned} \quad (3.8)$$

The layer structure on the cone, obtained from equally spaced level sets of D , is shown in Fig. 3.4. The projected layers and geodesics seen from above are shown in the left panels of Fig 3.5. Notice that the positive X axis develops a grain boundary for any nontrivial deficit angle.

Indeed, the existence of a cusp is a consequence of the Gauss-Bonnet Theorem [57, 111]; the maximum cusp angle of the layers at the grain boundary is equal to $\pi - \delta$ and occurs at the cone apex. To see this, consider a closed path consisting of the geodesic at $\omega = \omega_0$ from P_0 to an arbitrary point P_1 on the grain boundary, followed by the “mirror” geodesic at $\omega = -\omega_0$ from P_1 back to P_0 . The geodesics form an interior angle $\pi - \alpha_c$ on the cone at P_1 , where α_c is the cusp angle formed by the layer at P_1 . At P_0 , $2\omega_0$ is the interior angle formed by the geodesics on the cone. Because the geodesic curvature is zero on this path, and the integrated Gaussian curvature is

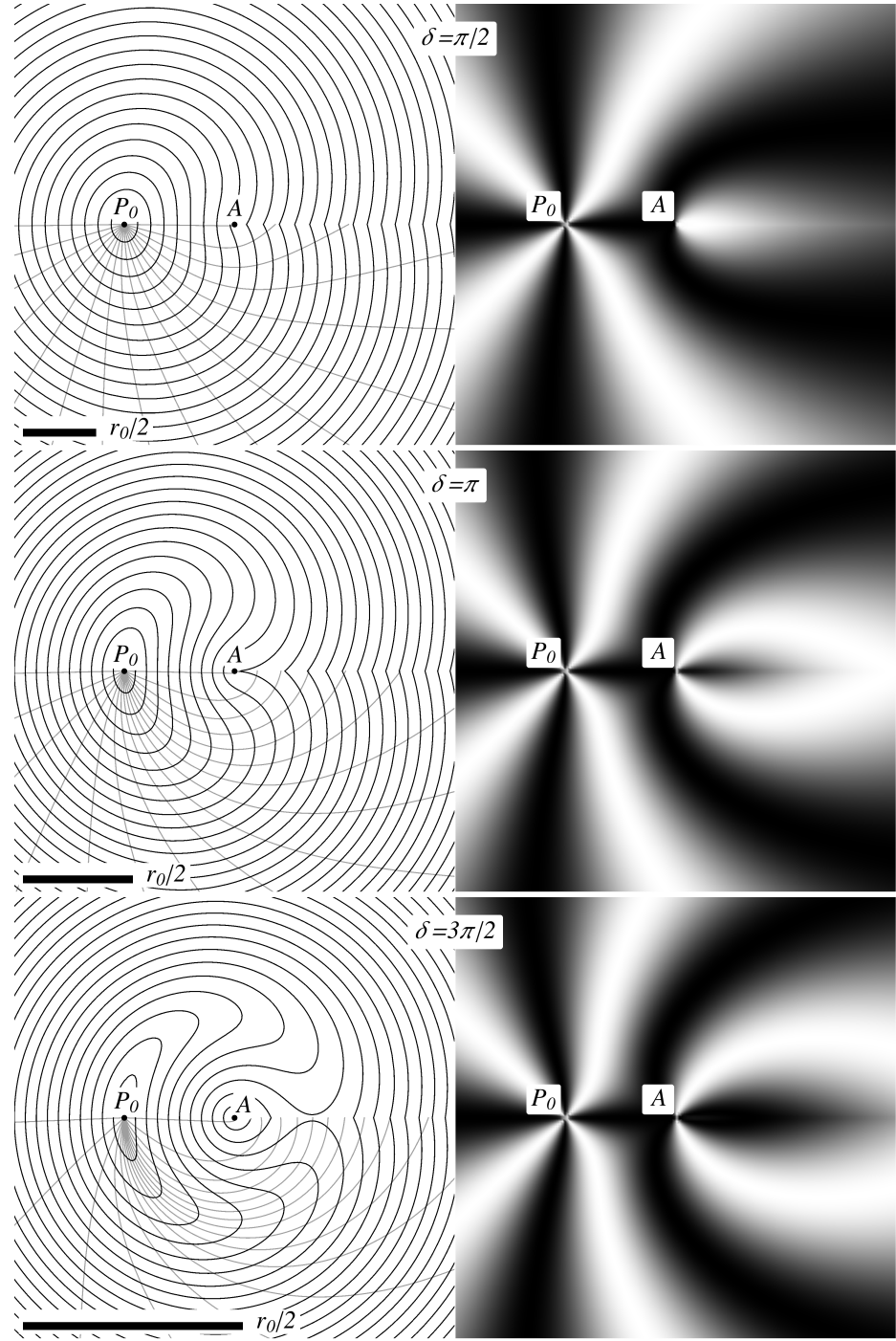


Figure 3.5: The left panels show the layer structure (black lines) superimposed on geodesics (gray lines on the bottom half) on the cone, as seen from above (i.e., projected on the XY plane), for deficit angles $\delta = \pi/2, \pi$, and $3\pi/2$, respectively. The right panels show the corresponding schlieren textures for the same deficit angles. A and P_0 label the cone apex and the disclination location, respectively. [92]

simply δ , the Gauss-Bonnet Theorem implies

$$\delta = 2\pi - (\pi - \alpha_c) - (\pi - 2\omega_0) = \alpha_c + 2\omega_0 \quad (3.9)$$

(notice that this equation also follows at once from the flattened model by elementary geometry). The cusp angle α_c is therefore maximized when we take $\omega_0 \rightarrow 0^+$, which corresponds to taking P_1 arbitrarily close to the cone apex. For values of δ greater than π , the cusp angle becomes π at some point to the right of the cone apex, meaning that the layers turn back toward the apex. Consequently, when $\delta > \pi$ the grain boundary is interrupted by two new point defects: a $+1$ -index disclination at the apex and a -1 -index disclination on the positive X -axis! This is shown in the left panels of Fig. 3.5 and also in Fig. 3.4. The negative-index defect results from the fact that the normal of some layers turns through an angle greater than or equal to π , and the outermost such layer has a self-intersection on the grain boundary, resulting in a locally hyperbolic configuration. By setting $Y = 0$, $N_p = (0, \pm 1)$ and solving for X , we discover that the -1 -index disclination is located at $X = -\frac{2\pi-\delta}{2\pi}r_0 \cos(\delta/2)$ when this quantity is positive. As $\delta \rightarrow \pi^+$, the -1 -index disclination coincides with the $+1$ disclination at the cone apex, and for smaller values of δ the grain boundary is free of point disclinations. Note that this disclination dipole does not create a dislocation and is an example of a *pincement* [23, 69] that is so “large” as to have generated extra internal concentric layers, the dual to large Burgers vector dislocations [69].

3.3 Schlieren textures

How would these layer structures appear in an experiment? In examining nematic and smectic liquid crystalline textures, it is common to view the sample between a pair of perpendicularly crossed polarizers. The resulting schlieren texture, characterized

by dark brushes on a bright background, reveals where in the sample the molecular orientation aligns on average with the direction of either polarizer. For a smectic-A liquid crystal on a conical substrate, the molecules are normal to the layers aligned along the unit vector field $N = (N_X, N_Y, N_Z)$ in the three-dimensional ambient space. If we were to view the sample between a pair of crossed polarizers parallel to the XY plane, we would measure N_p , the normalized horizontal projection of N . Denoting Θ as the oriented angle between the axis of one of the polarizers and the X axis, it follows from Eq. (3.7) that the intensity of the light observed at a point (X, Y) is proportional to $\sin^2[2(\Phi - \Psi - \Theta)]$. Fig. 3.5 shows the schlieren texture along with the layer structure for several choices of the deficit angle when $\Theta = 0$. It is interesting to note that, besides the defect at P_0 (wavefront source), the schlieren texture also displays what is usually the signature of defects, the termination of dark brushes, at the apex and at another point farther down the cone at positive X . This occurs due to the grain boundary even for $\delta < \pi$, when the positive X axis contains no topological defects. More surprising deviations from the usual rules governing schlieren textures are apparent when $\delta = 3\pi/2$ and we rotate the polarizers, as shown in Fig. 3.6. To the right of the apex, dark brushes abruptly disappear into the horizontal axis from below, while other dark brushes spring into existence in the upper half-plane, as the polarizers turn counterclockwise. In an experiment, such a schlieren texture would be the clearest evidence of a grain boundary, demonstrating the range of “missing” angles associated with a discontinuity in layer normals. Furthermore, the number of dark brushes emerging from the point defect at the apex is not constant and is odd for certain polarizer angles. In contrast, liquid crystalline textures that are continuous except (only) at point disclinations typically exhibit a constant, even number of dark

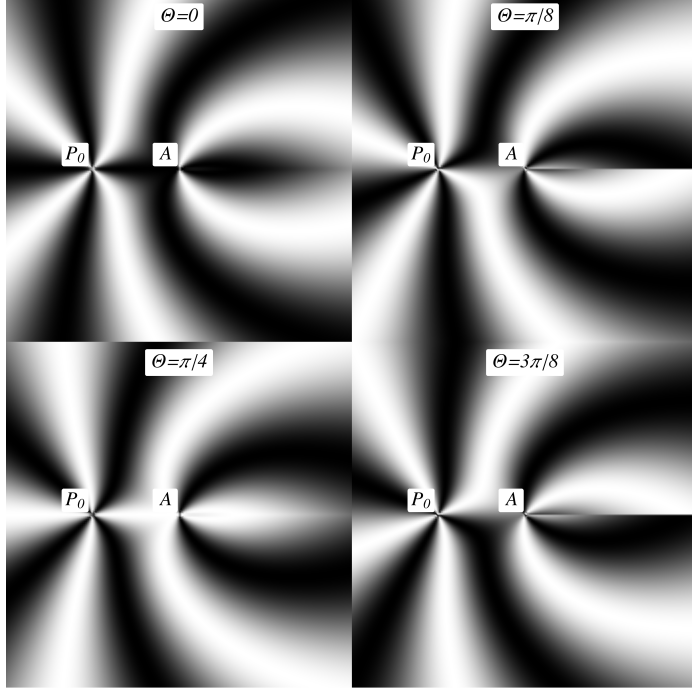


Figure 3.6: Schlieren textures for deficit angle $\delta = 3\pi/2$, with the polarizer direction at angles of $\Theta = 0, \pi/8, \pi/4$ and $3\pi/8$ with the X -axis, respectively. The analyzer direction rotates to remain perpendicular to the polarizer direction. A and P_0 label the cone apex and the disclination location, respectively. [92]

brushes emanating from each disclination.⁸ This strange behavior can be understood by noting that the normalized horizontal projection N_p of N is not orthogonal to the projection of the layers on the XY plane (as opposed to the 3D vector N and the layers on the 3D cone which are, of course, orthogonal to each other). This can be easily seen in the left panels of Fig. 3.5 and follows from the form of ds^2 in (3.2). We will come back to this point in the next section when we discuss the conical bump.

A slight generalization of the conical surface above is given by a tent, as shown in Fig. 3.7 for $\delta = \pi$. When $\delta > \pi$, a ± 1 -index disclination pair appears as on the cone, with the $+1$ -index disclination located at the right endpoint of the tent ridge. The

⁸A notable exception is the case of degenerate hybrid aligned nematic (HAND) films, where the number of dark brushes may vary with the polarizer angle because distortions in the director field are most concentrated in a small sector of a disk surrounding the defect [76].

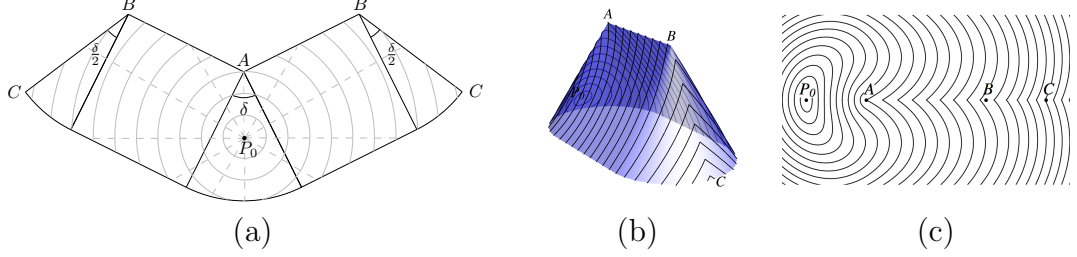


Figure 3.7: Substrate in the shape of a tent. (a) A flattened model from which a tent can be constructed by gluing along the lines AB and the lines BC . Also shown are a point disclination at P_0 and its associated geodesics (dashed lines) and layers (solid lines). (b-c) The corresponding layers in the 3D tent (b) and their 2D projection (c) for the case when $\delta = \pi$ and $\overline{AB} = \overline{AP_0} = 1$. A , B , and P_0 label the cones apices and the prescribed disclination location, respectively. [92]

layer structure can be obtained identically as before by employing the flattened model shown in Fig. 3.7a.

3.4 Smectics around edges

The infinite cone has an isolated singularity at the apex. We have also considered the case of a tent, where the substrate has an edge, i.e., a line where the surface is not smooth. Other examples are shown in the last three images of Fig. 3.1, for which a flattened model is not easily obtained because the edge is not straight in the xy -coordinate system. The geodesics of such surfaces will generally appear kinked at the edge. In fact, an argument similar to what is used in geometric optics, in connection to Fermat's principle, shows that a geodesic should cross an edge following Snell's law. This can be easily seen by noting that a geodesic is a curve with constant velocity that provides the path of minimal length—and therefore minimal time—between two given points. Note that the smectic analog of time is the number of layers through which the geodesic passes over a given distance. Since the smectic layer spacing is the same on both sides of the interface, Snell's law implies that the angle of incidence

equals the angle of “refraction” from the edge, where these angles are measured in the tangent planes on either side of the edge. The angle of refraction might differ from the angle of incidence if an interface separated two smectic phases of different layer spacing, as larger layer spacing is analogous to smaller index of refraction. This could occur in systems of immiscible smectics or at first-order transitions between different smectic phases of the same material. But we digress.

Consider the “crater” on the second panel of Fig. 3.1. By symmetry, its layer structure (provided some boundary condition) can be immediately obtained from that on the single cone by reflection across an appropriate horizontal plane. A more interesting configuration is the mountain pass shown in the third panel of Fig. 3.1. Here we can also use symmetry to simplify matters. Since the substrate has mirror symmetry across the vertical plane that contains the intersection, a geodesic that crosses the interface is simply the mirror image of a geodesic reflected through the edge. In the flattened model of the cone, the intersection will thus appear as a boundary Γ that acts like a mirror, reflecting the “incident rays” according to the “angle of incidence equals angle of reflection” rule on the plane. This is displayed in Fig. 3.8, which also shows the resulting layer structure for this case. Notice that a grain boundary is formed at the intersection between the surface and the XZ plane for all points on the left of the rightmost apex, even between the cones.

Our discussion so far illustrates the general principle that, whenever curvature is present, the constraint of having equally spaced layers leads to singularities in their structure, with the appearance of cusps and grain boundaries. In particular, smectics on substrates composed of Gaussian bumps have been shown to provide an accessible system where these ideas take place [57, 111]. We now analyze a minimalist and localized version of the Gaussian bump, the conical bump on the rightmost panel of Fig. 3.1.

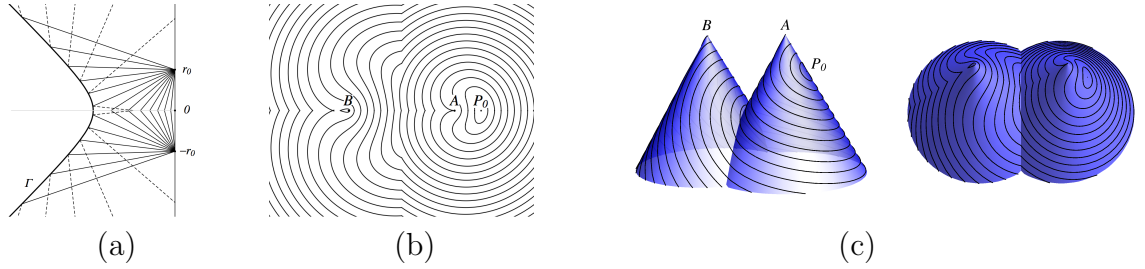


Figure 3.8: Smectic layers on two intersecting cones with deficit angle π and apices A , B . The layer structure is determined by a point disclination at P_0 , located a distance r_0 from apex A as measured on the cone. The horizontal distance between the two apices is chosen to be $2r_0$. (a) Geodesics in the flattened out model of the rightmost cone. Notice that the cut line L (Fig. 3.2) coincides, in this case, with the positive and negative y axes so that $(0, r_0)$ and $(0, -r_0)$ represent the same point. The intersection line is represented by Γ . Geodesics on the rightmost cone are represented by solid lines while the mirror reflection of those geodesics that enter the leftmost cone are depicted by dashed lines. (b-c) The layer structure on the cones. [92]

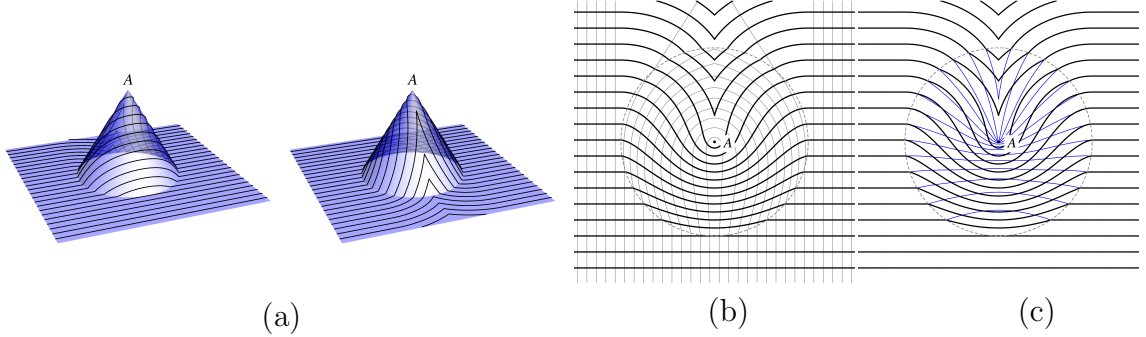


Figure 3.9: Conical bump with deficit angle given by π . We consider as boundary conditions layers parallel to the X axis at $Y \rightarrow -\infty$. (a) The layers on the 3D bump. (b) The projected layers (black) and projected geodesics (gray) on the substrate; notice that they are not orthogonal to each other in the plane metric. (c) The projected layers (black) along with fictitious layers (thin blue lines) which are constructed by demanding orthogonality with the projected geodesics (see text). The intersection between the cone and the plane is depicted by a dashed circle and A labels the cone apex. [92]

We consider a situation with the boundary condition chosen to be layers parallel to the X axis at $Y \rightarrow -\infty$. Before meeting the cone, a geodesic γ which is normal to the layers is a straight line parallel to the Y axis. At the interface it deflects according to Snell's law and then becomes a geodesic on the cone. There are two possibilities at this point, as the geodesics can become trapped in the cone or can escape. If γ enters the cone near the Y axis, i.e., with $X = X_0$ close to 0, it will reach the $X = 0$ plane before leaving the cone. As X_0 grows, γ will leave the cone and become a straight line again before crossing the $X = 0$ plane. By symmetry, the same will happen to the geodesic corresponding to $-X_0$ and, as a result, a grain boundary will develop at the points of the cone located along the positive Y axis. An interesting observation can be made about the escaped geodesics. Since a cone is an axisymmetric surface, γ must satisfy Clairaut's relation. This means that if $\rho(s)$ is the radial distance of the point $\gamma(s)$ (in the XY plane) from the cone apex and $\alpha(s)$ is the angle that $\gamma'(s)$ makes with a longitude line of the surface, then $\rho(s) \sin \alpha(s)$ is constant for each such geodesic. At the boundary of the cone all the values of ρ are the same and α is just the angle that γ makes with the interface. Therefore, γ enters and leaves the cone making the same angle with the edge. As before, to determine the trajectory of the geodesics inside the cone (and their exit point), we may either trace straight lines in the flattened model or solve the geodesic equations on the cone. This is all illustrated in Fig. 3.9 for a conical bump with deficit angle $\delta = \pi$.

We saw in the previous section that the projected layers of a non-planar surface are generally not orthogonal to their projected geodesics. This leads to schlieren textures exhibiting an odd behaviour when the sample is analyzed with crossed polarizers parallel to the XY plane. Now, suppose that we do not initially know that the sample is really a curved surface and try to interpret it as a planar substrate. Apart from the fact that we would be surprised by the unusual pattern of brushes, we would also

be led to identify a fictitious set of planar layers which are everywhere orthogonal to the projected geodesics, the latter being inferred from measurements under crossed polarizers. Since the projected geodesics are not geodesics on the plane by themselves, these fictitious layers cannot be equally spaced! This is illustrated by Fig. 3.9b,c. Notice that, as expected, both the projected and the fictitious layers agree in the planar region but, inside the bump, the latter are highly compressed and have the opposite sign of curvature than the projected layers. This explains why the schlieren textures resulting from a non-planar surface look so odd. If these fictitious layers were real, they would correspond to a high energy configuration, due to compression, and therefore would not represent the ground state. The transition to an equally spaced structure amounts precisely to escaping to the third dimension and assuming the layer configuration and shape of the bump. The infinite strain in the fictitious layers near the cone apex signals this incompatibility as well. Whether the fictitious layers and their geometry can be used as a surrogate to calculate the back reaction forces on a deformable surface is an open question.

Chapter 4

Focal conic domains in smectic-A liquid crystals with confining boundaries of complex shape

This chapter explores new types of micropatterning in smectic-A liquid crystals achieved through the influence of boundary geometry—specifically, curvature and topographic patterning—on the self-assembly of focal conic domains (FCDs). We begin in Section 4.1 with an overview of the structure and energetics of focal conic domains, as well as an elegant geometrical model of complex FCD self-organization called the law of corresponding cones. Topographically patterned substrates are shown to confine and direct the patterning of a special, axially symmetric kind of FCD, called the toric focal conic domain, in Section 4.2. In Section 4.3, topographic patterning in the boundary leads to more complicated, hierarchical packings of more general FCDs without axial symmetry, and we model both the geometry and energetics of resulting smectic structures. Finally, in Section 4.4, curvature in the boundary is shown to promote an unusual, radial organization of FCDs, which we explain via analogy with the FCDs found in smectic tilt grain boundaries and then connect with the classical “law of corresponding cones” through a new geometrical model.

4.1 Background: Focal conic domains and the law of corresponding cones

4.1.1 The smectic-A phase, focal sets and Dupin cyclides

The smectic-A liquid crystal (SmA LC) phase consists of rod-like molecules assembled into layers one molecule in thickness, with the molecules' long axes oriented on average normal to the layer. It can be considered a two-dimensional fluid within each layer, and a one-dimensional crystal along the layer normal direction. The ground state (Fig. 4.1a) consists of parallel, planar layers with constant spacing d_0 approximately equal to the molecular length.

The bulk free energy for a SmA LC can be written

$$F = \int dV \left[\frac{1}{2} K_1 (\sigma_1 + \sigma_2)^2 + \bar{K} \sigma_1 \sigma_2 + \frac{1}{2} B \left(\frac{d - d_0}{d_0} \right)^2 \right]. \quad (4.1)$$

In the first term, the splay elastic modulus K_1 penalizes mean curvature of the layers, defined in terms of the principal curvatures σ_1 and σ_2 , which are functions of space. In the second term, a Gaussian curvature modulus \bar{K} multiplies the Gaussian curvature of the layers. In the third term, a bulk modulus B penalizes compression or dilation of the layer spacing d from the preferred layer spacing d_0 . Generally, compression/dilation distortions are much more energetically costly than layer curvature distortions. More precisely, the length scale $\lambda \equiv \sqrt{K_1/B}$ is usually on the order of the layer spacing d_0 , a microscopic length, so that distortions significantly affecting the layer spacing ought to be confined to regions of microscopic volume [30]. For this reason, it is common to assume the “limit of incompressibility”, according to which the smectic layers are equally spaced everywhere except possibly in sets of dimensionality smaller than the

sample dimensionality: walls, curves, or points for 3D smectics. From a macroscopic perspective, these sets, known as *focal sets*, appear to have “cusp” discontinuities in the layer normal direction, and they are treated as geometrical singularities where smectic order breaks down. Crucially, however, the energetic cost of these singular sets depends strongly on their dimensionality. The limit of incompressibility leads to an intriguing mathematical explanation for the shapes of experimentally observed singular curves in SmA LCs, which will be the signature of focal conic domains, as we will explore below. Everywhere outside of the focal sets, the layers maintain constant spacing d_0 along the layer normal direction, which requires that consecutive layers are parallel, i.e., the layer normal direction integrates to a straight streamline.

Whereas the smectic ground state easily satisfies uniform boundary conditions, in this chapter we will mainly study thin films of SmA LCs under *hybrid anchoring conditions*, with a substrate/LC interface below and an air/LC interface above providing mutually antagonistic boundary conditions. At the free air/LC interface, the rod-like molecules prefer an orientation perpendicular to the interface, so that a topmost layer is parallel to the interface. This is *homeotropic anchoring*, and is illustrated in Fig. 4.1a where we imagine the topmost layer to be the air/LC interface. At the substrate/LC interface, the substrate chemistry is chosen to promote *degenerate planar anchoring*, meaning that the rod-like molecules prefer any direction in the plane of the substrate, so that the layers prefer to approach the substrate perpendicularly, as illustrated in Fig. 4.1b.

The antagonistic nature of the two interfaces defining hybrid anchoring conditions requires the smectic layers to distort away from the ground state in the bulk. However, the high energetic cost of compression/dilation distortions, along with the associated assumption of parallel layers, means that almost all distorted layer configurations will prove highly energetically costly because of the nature of their focal sets. On the other

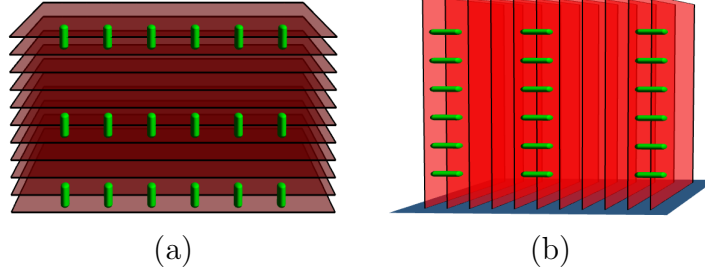


Figure 4.1: Schematic illustrations of the smectic-A ground state and anchoring conditions, with smectic layers in red and representative rod-like molecules in green. (a) Smectic-A ground state. If the topmost layer is the air/LC interface, then this illustrates homeotropic anchoring. (b) Smectic-A ground state illustrating degenerate planar anchoring at a planar substrate.

hand, a very special set of layer configurations will have significantly lower free energy; these will be the focal conic domains.

To explore the concept of focal sets, we begin in two dimensions with planar curves. Fig. 4.2 illustrates the concept with an ellipse as the example curve. At any point on the curve, the tangent vector is perpendicular to a unit normal vector, and the magnitude of the tangent vector's rate of change is the curvature, inverse to a radius of curvature that defines the distance along the normal direction from the point on the curve to its associated center of curvature. Generically, as we move the point under consideration around the ellipse, the center of curvature moves, tracing out a one-dimensional set which is the ellipse's focal set, also known as the evolute. There exists a special curve, the circle, whose focal set is one dimensional, namely the center of the circle.

Surfaces embedded in three dimensions generically have two-dimensional focal sets. This is illustrated in Fig. 4.3 with a saddle-shaped surface. Each point on the surface has curves passing through it in all directions in the tangent plane, each with its own curvature. The maximum and minimum such curvatures are the principal

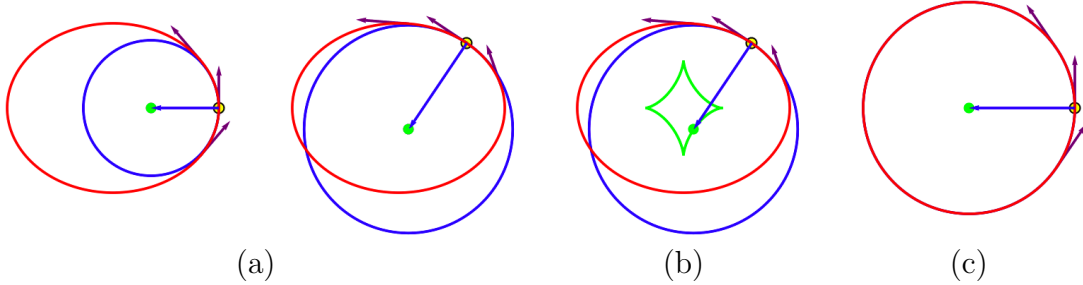


Figure 4.2: Concept of focal sets for planar curves illustrated with an ellipse (red). For a given point (yellow) on the curve, the magnitude of the rate of change of the tangent vector (purple) gives the radius of curvature, which describes the size of a circle (blue) that approximates the curve locally and that is centered at the local center of curvature, shown in green in (a). In (b), the locus of centers of curvature associated with all points on the curve traces out a one-dimensional set called the focal set, or evolute. (c) For the special case of a circle, the focal set collapses to a point at the circle's center.

curvatures σ_1 and σ_2 , which are respectively inverse to radii of curvature R_1 and R_2 and are associated with two principal directions. The radii of curvature give the size of circles that approximate the surface locally along the principal directions (Fig. 4.3a). Importantly, the point on the surface and its two centers of curvature are collinear, separated along a line parallel to the surface normal direction called the *generator*. As we trace out the locus of centers of curvature for all points on the surface, we generically trace out two disjoint two-dimensional sets, which are the focal set (evolute) of the surface (Fig. 4.3b).

The key fact about focal sets that is pertinent to SmA LCs is that in a family of parallel surfaces (e.g., smectic layers), all the surfaces share the same focal set. Consider a surface S_0 and a parallel surface S_ϕ constructed by shifting every point on S_0 a distance ϕ in the surface normal direction. This shift changes the radii of curvature R_1 and R_2 at any given point P_0 on S_0 to $R_1 + \phi$ and $R_2 + \phi$ at the corresponding point P_ϕ on S_ϕ [32]. As the layer normal direction remains unchanged by the shift, the center

of curvature associated with P_ϕ is the same point as the center of curvature associated with P_0 ; the change in the radii of curvature simply offsets the shift distance ϕ . This implies that, as we keep adding smectic layers, eventually the layers will intersect their own focal set. At such places, a radius of curvature vanishes so that one of the principle curvatures diverges, and also the layer normal experiences a “cusp” discontinuity so that equal layer spacing much break down. Thus there is a significant energetic cost both in terms of curvature and compression/dilation. A single layer might intersect its focal set along a one-dimensional subset, so a portion of the family of parallel layers will suffer from these singularities along a two-dimensional set, namely, the focal set itself.

When boundary conditions require distortion, SmA LCs would therefore encounter a major energetic problem, unless they can have focal sets of dimensionality smaller than two. Just as circles are the only planar curves with zero-dimensional focal sets, we seek a special class of surfaces with only one-dimensional focal sets. As it turns out, collapsing the focal surfaces to focal curves is indeed possible, but only for a very special class of surfaces called the Dupin cyclides [35]. The focal curves must be conjugate conic sections: an ellipse and one branch of a hyperbola in orthogonal planes, each passing through a focus of the other (Figures 4.4 and 4.5a). (In a limiting case that we will not consider here, the focal curves may instead be two parabolas intersecting at a point.)

As shown in Fig. 4.5a, we restrict our attention to the inner portions of the Dupin cyclides with negative Gaussian curvature. Negative Gaussian curvature implies smaller mean curvature than a positively curved surface with principle curvatures of similar magnitude; moreover, the portions of the cyclides considered are sufficient to explain the experimental observations. A focal conic domain (FCD) is a family of parallel, equally spaced smectic layers in the form of portions of Dupin cyclides (Fig. 4.5b).

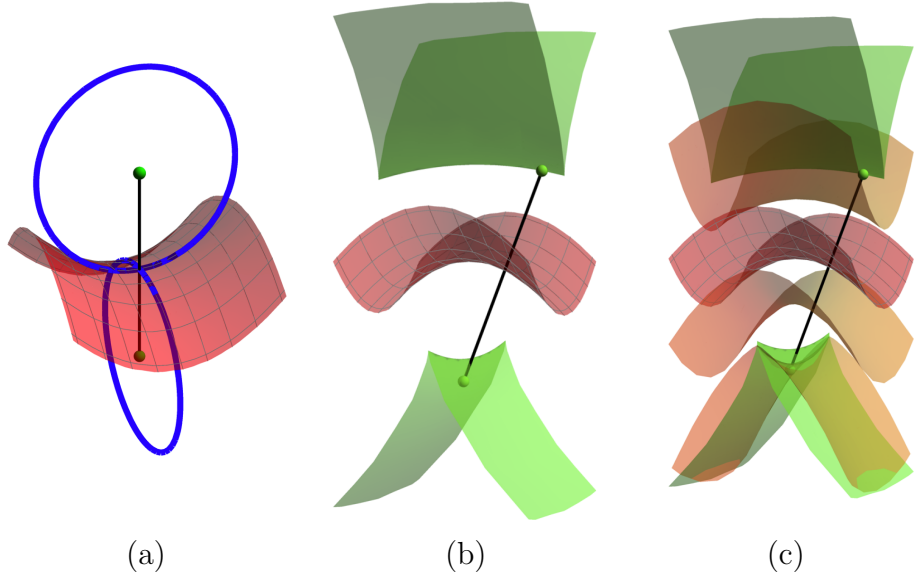


Figure 4.3: Concept of focal sets for surfaces illustrated with a saddle (red). (a) Any point on the surface has two centers of curvature (green) which describe the size of circles (blue) that approximate the surface along the two principal directions. The circles' radii are radii of curvature, inverse to the principal curvatures. Both centers of curvature are separated from the point on the surface along the normal direction (black). (b) Tracing out the locus of centers of curvature generically yields two disjoint two-dimensional sets, which together form the surface's focal set, or evolute. (c) Surfaces (orange) parallel to the original surface (red) share the same focal set (green). Eventually, adding parallel layers requires some layer to intersect its own focal set.

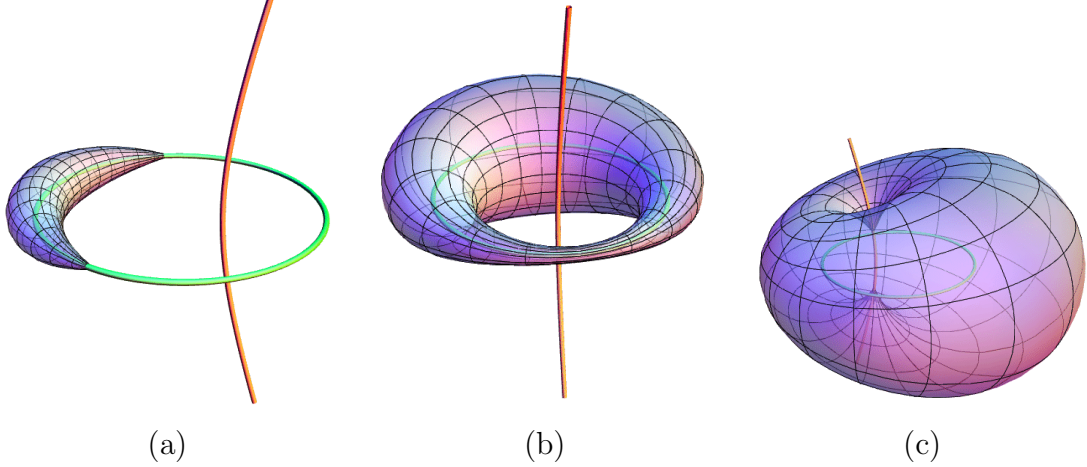


Figure 4.4: Dupin cyclides, with their focal ellipse in green and focal hyperbola in orange. A cyclide may be singular on the ellipse (a), on the hyperbola (c), or neither (b) (as shown from different viewing angles).

The ellipse-hyperbola pair comprises the focal set of the FCD, which is therefore one-dimensional.

In addition, it is possible for a family of parallel surfaces to have a zero-dimensional focal set, but only in the special case where the surfaces are concentric spheres (Fig. 4.5c), their focal set being the common center. Due in part to their high mean curvature, concentric sphere families do not destabilize FCDs. However, the availability of concentric sphere families as a smectic building block will turn out to be of great importance to FCD assembly.

We might think of Dupin cyclides as merely a mathematical curiosity were it not for the fact that SmA LCs frequently show evidence of possessing them. In fact, the prototypical kinetically-trapped texture of this LC phase exhibits singular lines in the form of nearly perfect elliptical and hyperbolic singular lines, visible under bright-field microscopy [40]. Such “focal conics” are also present at equilibrium in many situations (see, e.g., Fig. 4.21a and Fig. 4.22c below). Moreover, under polarized optical microscopy, one focus of each ellipse exhibits a four-fold crossing of light and

dark bands, characteristic of a +1 winding of the director in the plane of the ellipse around the focus (see Fig. 4.21b). It was actually from such observations of focal conics that the physical manifestation of Dupin cyclides, and thus the equally-spaced layer structure of the SmA LC phase, were first deduced [40].

Why should the smectic free energy disallow 2D focal sets but permit 1D focal sets, when 0D focal sets are also available? Part of the answer lies in the fact that FCDs provide a natural way to satisfy hybrid anchoring conditions, as we will explore in Section 4.2. But we can also gain some insight from a simplified energetic scaling argument based on the bulk free energy of Eqn. 4.1. We assume that there is a single macroscopic length scale L , the system's linear size. We also assume that there is a single microscopic length scale $\lambda \equiv \sqrt{K_1/B}$ roughly equal to the smectic layer spacing and the molecular length, which for the SmA LCs considered in this chapter is around 3 nm. The microscopic defect core size is taken to be $\sim \lambda$. We also define a relative layer compression/dilation factor $\varepsilon \equiv (d - d_0)/d_0$.

Using these definitions, we calculate how the compression and mean curvature energies of Eqn. 4.1 scale for smectic layer configurations with focal sets of dimensionality 0 (concentric spheres), 1 (focal conic domains), or 2 (tilt grain boundaries). A singularity of dimensionality n has size L in n dimensions and size λ in $3 - n$ dimensions. The energetic scaling estimates are:

n	name	compression energy	curvature energy
0	concentric spheres	$\sim (B\varepsilon^2)\lambda^3 \sim K_1\lambda\varepsilon^2$	$\sim K_1L$
1	focal conic domains	$\sim (B\varepsilon^2)L\lambda^2 \sim K_1L\varepsilon^2$	$\sim K_1L\ln(L/\lambda)$
2	tilt grain boundaries	$\sim (B\varepsilon^2)L^2\lambda \sim K_1L(L/\lambda)\varepsilon^2$	$\sim K_1L(L/\lambda)$

The total energy scales as $\sim K_1L$ for concentric spheres, $\sim K_1L\ln(L/\lambda)$ for FCDs, and $\sim K_1L(L/\lambda)$ for tilt grain boundaries. Tilt grain boundaries are more energetically costly than concentric spheres by a factor $L/\lambda \sim 10^3 - 10^4$. However, FCDs are more

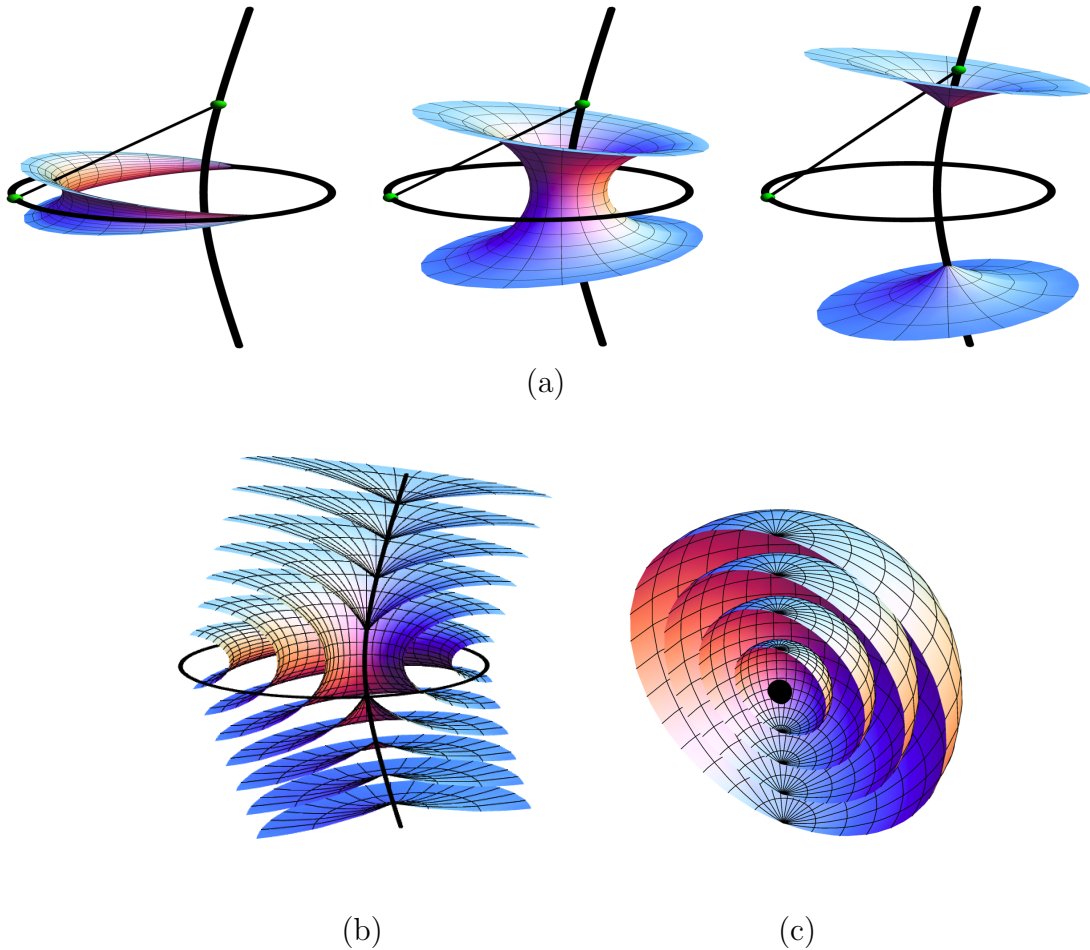


Figure 4.5: Construction of a focal conic domain from Dupin cyclides. (a) Dupin cyclides and their focal set (the “focal conics”), with example centers of curvature shown as green balls. The point on the surface and its associated centers of curvature on the hyperbola and the ellipse are collinear along the generator line. We consider only the portions of the cyclides with negative Gaussian curvature, which are the surfaces relevant to physical FCDs. (b) A focal conic domain (FCD), constructed from a family of equally spaced Dupin cyclides, along with its focal set (the “focal conics”). (c) A family of equally spaced concentric spherical layers, whose focal set is zero-dimensional.

energetically costly than concentric spheres by a smaller factor $\ln(L/\lambda)$ which is typically less than 10, and therefore not prohibitive. In combination with surface energies from the hybrid anchoring conditions, FCDs are therefore often more stable than concentric spheres despite having focal sets of one higher dimensionality.

4.1.2 The usual parameterization

Here we review the mathematical construction of idealized elliptic-hyperbolic focal conic domains (FCDs). We take as focal sets an ellipse, parameterized as $\vec{E}(u)$, and a hyperbola, parameterized as $\vec{H}(v)$, as follows:

$$\vec{E}(u) = (a \cos(u), b \sin(u), 0), \quad u \in [0, 2\pi] \quad (4.2)$$

$$\vec{H}(v) = (c \cosh(v), 0, b \sinh(v)), \quad v \in (-\infty, \infty) \quad (4.3)$$

Here, a and b are respectively the semi-major and semi-minor axes of the ellipse, and $c \equiv \sqrt{a^2 - b^2} \equiv ae$ where e is the eccentricity of the ellipse. We call e the eccentricity of the FCD, as well. We now wish to construct smectic layers that, for fixed u , are circles concentric about the ellipse point $\vec{E}(u)$, and, for fixed v , are circles concentric about the hyperbola point $\vec{H}(v)$. We first calculate the distance from $\vec{E}(u)$ to $\vec{H}(v)$:

$$\begin{aligned} d(u, v) &\equiv \sqrt{\vec{H}(v) - \vec{E}(u)} \\ &= [a^2 \cos^2(u) + c^2 \cosh^2(v) - 2ac \cos(u) \cosh(v) + b^2 \sin^2(u) + b^2 \sinh^2(v)]^{1/2} \\ &= [(b^2 + c^2) \cos^2(u) + (a^2 - b^2) \cosh^2(v) - 2ac \cos(u) \cosh(v) + b^2 \sin^2(u) \\ &\quad + b^2 \sinh^2(v)]^{1/2} \\ &= [c^2 \cos^2(u) + a^2 \cosh^2(v) - 2ac \cos(u) \cosh(v) + b^2 - b^2]^{1/2} \\ &= a \cosh(v) - c \cos(u) \end{aligned}$$

Every point \vec{X} in the domain is associated with a single generator line $G(u, v)$ connecting $\vec{E}(u)$ to $\vec{H}(v)$. For each \vec{X} , there are two possible choices of G : one for which \vec{X} lies between $\vec{E}(u)$ and $\vec{H}(v)$, and the other for which $\vec{H}(v)$ lies between $\vec{E}(u)$ and \vec{X} . Type I FCDs are constructed of the former, and Type II FCDs are constructed of the latter. We can consider all the possible $\vec{E}(u)$ points simultaneously by imagining the cone of revolution $C_{\vec{X}}$ with base on the ellipse and with apex at \vec{X} . $C_{\vec{X}}$ intersects the hyperbola at one point, which gives $\vec{H}(v)$ for a Type II FCD. The rays of $C_{\vec{X}}$ can be extended to produce an inverted cone $C'_{\vec{X}}$ with apex at \vec{X} . $C'_{\vec{X}}$ also intersects the hyperbola at up to one point, which gives $\vec{H}(v)$ for a Type I FCD. However, $C'_{\vec{X}}$ may not intersect the hyperbola at all, in which case the virtual branch of the hyperbola must be considered, as we will discuss below.

Each layer is parameterized by (u, v) . The entire FCD is parameterized by (u, v, ϕ) , where ϕ parameterizes the layer normal direction and is defined such that $\phi = c \cos(u)$ on the ellipse and $\phi = a \cosh(v)$ on the hyperbola, with the positive ϕ direction pointing from $\vec{E}(u)$ to $\vec{H}(v)$. Then (u, v, ϕ) is an orthogonal coordinate system. The parameterization of a Type I FCD is

$$\begin{aligned} x(u, v, \phi) &= \frac{a \cos u (a \cosh v - \phi) + c \cosh v (\phi - c \cos u)}{a \cosh v - c \cos u} \\ &= \frac{\phi (c \cosh v - a \cos u) + b^2 \cos u \cosh v}{a \cosh v - c \cos u} \\ y(u, v, \phi) &= \frac{b \sin u (a \cosh v - \phi)}{a \cosh v - c \cos u} \\ z(u, v, \phi) &= \frac{b \sinh v (\phi - c \cos u)}{a \cosh v - c \cos u} \end{aligned}$$

$$u \in [0, 2\pi), \quad v \in (-\infty, \infty), \quad \phi \in [c \cos u, a \cosh v].$$

This actually parameterizes only the portions of the Dupin cyclides that have non-positive Gaussian curvature, which are the layer configurations typically seen in FCDs.

To construct the entire Dupin cyclides, we have to introduce another, virtual focal set located at the non-physical branch of the hyperbola. We do this by changing variables from v to t defined by $\cos t \equiv 1/\cosh v$. Then $\sinh v = \tan t$ and $\tanh v = \sin t$. The physical and unphysical branches of the hyperbola are parameterized together by $\tilde{H}(t) = (c/\cos t, 0, b \tan t)$, with t spanning the whole range of angles $(-\pi, \pi)$. Making the change of variables in the FCD-I parameterization from above, we obtain

$$\begin{aligned} x(u, t, \phi) &= \frac{\phi(c - a \cos u \cos t) + b^2 \cos u}{a - c \cos u \cos t} = \frac{\phi(e - \cos u \cos t) + a(1 - e^2) \cos u}{1 - e \cos u \cos t} \\ y(u, t, \phi) &= \frac{b \sin u (a - \phi \cos t)}{a - c \cos u \cos t} = \frac{\sqrt{1 - e^2} \sin u (a - \phi \cos t)}{1 - e \cos u \cos t} \\ z(u, t, \phi) &= \frac{b \sin t (\phi - c \cos u)}{a - c \cos u \cos t} = \frac{\sqrt{1 - e^2} \sin t (\phi - ae \cos u)}{1 - e \cos u \cos t} \end{aligned} \quad (4.4)$$

$u \in [0, 2\pi), \quad t \in [-\pi, \pi), \quad \phi \in [c \cos u, a \cosh v] \quad (\text{Type I})$

The same parameterization can be used to construct Type II FCDs, simply by changing the intervals used for the variables to

$$u \in [0, 2\pi), \quad t \in (-\pi/2, \pi/2), \quad \phi \in [a \cosh v, \infty) \quad (\text{Type II})$$

4.1.3 An aside: Transformations between Type I and Type II FCDs

Define $\varphi \equiv \phi - a/\cos t$, so that $\varphi = 0$ on the hyperbola. Now the parameterization reads

$$x(u, t, \varphi) = \frac{\varphi(c - a \cos u \cos t) + ac/\cos t - a^2 \cos u + b^2 \cos u}{a - c \cos u \cos t}$$

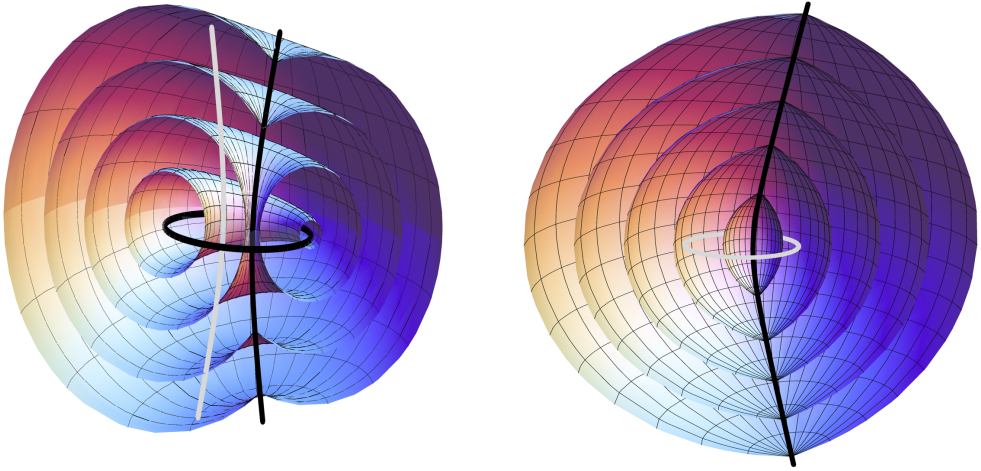


Figure 4.6: Left: Complete Dupin cyclides of Type I FCD. Right: Type II FCD. Physical focal sets are shown as black curves. Virtual focal sets are shown as light gray curves.

$$\begin{aligned}
 &= \frac{\varphi(c - a \cos u \cos t) + ac/\cos t - c^2 \cos u}{a - c \cos u \cos t} \\
 y(u, t, \varphi) &= -\frac{b\varphi \sin u \cos t}{a - c \cos u \cos t} \\
 z(u, t, \varphi) &= \frac{b \sin t(\varphi - c \cos u) + ab \tan t}{a - c \cos u \cos t}
 \end{aligned} \tag{4.5}$$

The intervals for φ are $[c \cos u - a/\cos t, 0]$ for Type I FCDs and $[0, \infty)$ for Type II FCDs. φ is nonpositive for Type I FCDs and nonnegative for Type II FCDs.

Now consider the following transformation: Send the ellipse major and minor axis lengths to their opposites and rotate the FCD about \hat{z} by π , while keeping the sign of c unchanged. In symbols,

$$a \rightarrow -a, \quad b \rightarrow -b, \quad c \rightarrow c, \quad u \rightarrow u + \pi. \tag{4.6}$$

Then, parameterization (4.5) becomes

$$\begin{aligned} x(u, t, \varphi) &= \frac{-\varphi(c - a \cos u \cos t) + ac/\cos t - c^2 \cos u}{a - c \cos u \cos t} \\ y(u, t, \varphi) &= \frac{b\varphi \sin u \cos t}{a - c \cos u \cos t} \\ z(u, t, \varphi) &= -\frac{b \sin t(-\varphi - c \cos u) + ab \tan t}{a - c \cos u \cos t} \end{aligned} \quad (4.7)$$

Comparing with parameterization (4.5), we see that transformation (4.6) is equivalent to taking $\varphi \rightarrow -\varphi$. (There is an additional reflection through the xy plane required to formally return to the original parameterization, but the FCD was symmetric under this reflection in the first place.) This means that taking a, b to $-a, -b$, along with a rotation by π , transforms an FCD of type I into an FCD of type II with the same eccentricity, and vice versa.

A continuous transformation of a and b into their opposites can be accomplished by taking them through 0, at which point the smectic layer configuration passes through concentric spheres. To see this more clearly, we can rewrite parameterization (4.5) with numerator and denominator divided by a :

$$\begin{aligned} x(u, t, \varphi) &= \frac{\varphi(e - \cos u \cos t) + ae/\cos t - ae^2 \cos u}{1 - e \cos u \cos t} \\ y(u, t, \varphi) &= -\frac{\sqrt{1 - e^2}\varphi \sin u \cos t}{1 - e \cos u \cos t} \\ z(u, t, \varphi) &= \frac{\sqrt{1 - e^2}(\sin t(\varphi - ae \cos u) + a \tan t)}{1 - e \cos u \cos t} \end{aligned} \quad (4.8)$$

Taking $a \rightarrow 0$,

$$\begin{aligned} x(u, t, \varphi) &= \frac{\varphi(e - \cos u \cos t)}{1 - e \cos u \cos t} \\ y(u, t, \varphi) &= -\frac{\sqrt{1 - e^2}\varphi \sin u \cos t}{1 - e \cos u \cos t} \end{aligned}$$

$$z(u, t, \varphi) = \frac{\sqrt{1 - e^2} \varphi \sin t}{1 - e \cos u \cos t} \quad (4.9)$$

which reduces to $x^2 + y^2 + z^2 = \varphi^2$. Alternatively, we could take a, b to $-a, -b$ through $\pm\infty$. At $a = \pm\infty$, the FCD becomes a family of cylinders coaxial about the line $x = y = 0$. This is less easy to see from the parameterization, but it is geometrically obvious for the $e = 0$ case where the focal sets are the line $x = y = 0$ and the circle in the xy plane at infinity; furthermore, the structure is invariant under Lorentz boosts and therefore does not change for $e \neq 0$. [4].

This relation between Type I and Type II FCDs under reversing the sign of a, b is seen clearly in the general formula of Ref. [4] for zero-eccentricity FCDs as the “product of two cones”,

$$[(s+r)^2 + z^2 - \phi^2] [(s-r)^2 + z^2 - \phi^2] = 0 \quad (4.10)$$

where $s = \sqrt{x^2 + y^2}$. Setting the first factor equal to zero gives Type II FCDs; setting the second factor equal to zero gives Type I FCDs. It is obvious that the two factors are related by reversing the sign of r .

4.1.4 The law of corresponding cones

The law of corresponding cones [40] allows multiple Type I FCDs to be joined together with no dislocations or discontinuities in the smectic layer normal. We now review the law of corresponding cones for a family of FCDs. The i th FCD is bounded by a right circular cone C_i that has its apex P on the hyperbola H_i and that includes the ellipse E_i . Thus, C_i consists entirely of generators, straight lines which are normal to the smectic layers and which each connect a point on E_i to a point on H_i . In the “fan” texture typical of kinetically trapped FCD assemblies, when two ellipses E_1 and

E_2 are tangent at a point Q , then their boundary cones C_1 and C_2 are tangent along an entire generator if C_1 and C_2 have a common apex P where the hyperbolae H_1 and H_2 intersect (Fig. 4.7a). Tangency along the generator \overline{QP} means that the layer normals of the two FCDs agree precisely where the FCDs come into contact with each other. Similarly, an FCD with bounding cone apex at P may be joined smoothly onto a family of concentric spheres centered at P (Fig. 4.7b) [115]. This is fortunate because concentric spheres, like FCDs, have a focal set of dimension less than two, avoiding energetically costly cusp wall defects.

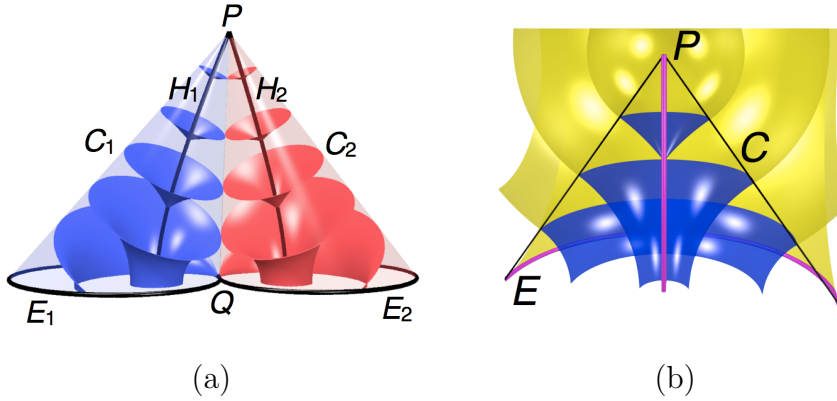


Figure 4.7: (a) The law of corresponding cones (LCC) illustrated for a pair of Type I focal conic domains (blue and red) with focal ellipses E_1 and E_2 tangent at point Q , focal hyperbolae H_1 and H_2 intersecting at point P , and bounding cones C_1 and C_2 tangent along the generator \overline{QP} . (b) A Type I focal conic domain (blue) with elliptical focal curve E and bounding cone C (outlined by black lines) intersecting the hyperbolic focal curve (a straight line in this case) at point P , with layers joined smoothly onto a family of spherical layers concentric about P .

What about Type II FCDs? Do they have a law of corresponding cones? For Type I FCDs, the key was to first construct a bounding cone consisting of generators (layer normals). Let's start by considering, for Type II FCDs, the cone of revolution C with apex on the hyperbola at $\vec{H}(v)$ and containing the elliptical focal curve. Unfortunately, the FCD generators no longer lie on the cone. However, if we continue the lines that

formed the cone, from $\vec{E}(u)$ to $\vec{H}(v)$ for $u \in [0, 2\pi]$, upward past $\vec{H}(v)$, we form an inverted cone of revolution C' that *does* consist of generators of the Type II FCD. By keeping only the region of the Type II FCD that is inside C' , we can join the Type II FCD onto other Type II FCDs, onto concentric spheres, and even onto Type I FCDs, all with bounding cone apex or center at $\vec{H}(v)$. This construction is illustrated in Fig. 4.8.

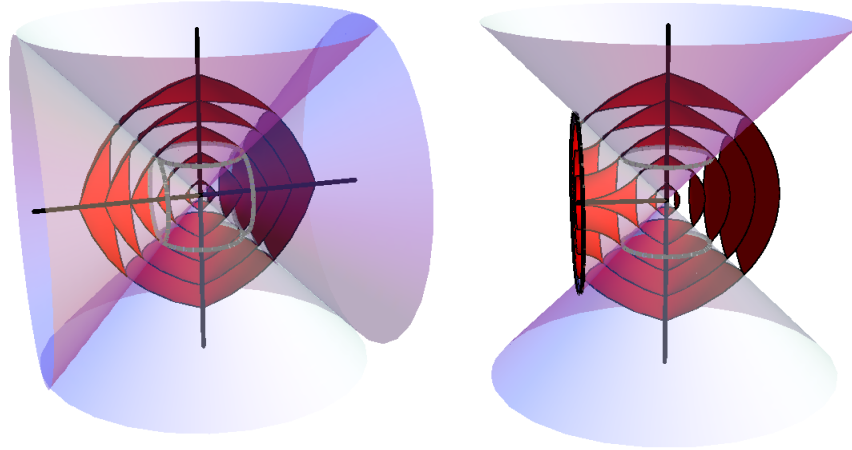


Figure 4.8: Left: Corresponding cones for Type II FCDs. Right: Composite texture of Type I and II FCDs and concentric spheres. Physical focal sets are shown in black, virtual focal sets in gray. For both figures, zero eccentricity is taken for simplicity.

4.2 Epitaxial directed assembly of toric focal conic domains on topographically patterned substrates

4.2.1 Introduction

Self-assembly, self-processing, and bottom-up design are ever more important tools for the development of new materials of both fundamental and technological interest due to their robust capability for generating complex, hierarchical structures. In general, self-assembling materials, including colloids, block copolymers, and supramolecules or DNA form thermodynamically stable structures over a broad range of length scales, from the micro- to nanoscales. Structure formation in these long-range ordered phases is often governed by entropic and geometric considerations, leading frequently to a limited variety of optimal, close-packed structures. However, close-packed structures are not always appropriate in device applications. Some control has been gained through so-called graphoepitaxy, which exploits substrates with topological [8, 11, 60, 112, 125] or chemical [36] surface relief patterns that nearly match the domain structures of block copolymers, for instance, and direct their epitaxial assembly into nanostructures with long-range positional order and orientation in thin films. However, epitaxial assembly of highly ordered square arrays has only been recently achieved in both triblock copolymers [26, 126] and supermolecular assemblies of hydrogen-bonding diblock copolymer in thin films [127].

Because of their geometrical, mechanical, and electronic anisotropy, liquid crystals are not only highly sensitive to external aligning fields but can also exquisitely control the propagation of electromagnetic phenomena. Consequently, the patterning of LC molecules has long been of interest for scientific discovery and technological

advancement. When the surface chemistry promotes planar alignment of LC molecules, smectic-A LCs spontaneously form highly ordered hexagonal arrays of toric focal conic domains (TFCDs; see Fig. 4.9c) [62], an axially symmetric case of the focal conic domain in which the focal ellipse and hyperbola degenerate to a circle and a straight line through the circle’s center (Fig. 4.9b). The Dupin cyclides in the TFCD case are simply portions of nested tori; hence the name “toric”.

With a self-assembly viewpoint, we regard the entire TFCD as a composite defect object. In surface measurements, a defect domain appears as a circular, cone-shaped dimple at the LC/air interface. The bending of the LC layers under hybrid anchoring conditions to form TFCDs results from the competing effects of planar anchoring at the LC/substrate interface and homeotropic anchoring at the LC/air interface. In the standard smectic ground state, the smectic layers are flat and parallel to the substrate and thus the molecular orientation points normal to both the LC/air and LC/substrate interfaces (Fig. 4.9a). The TFCDs form spontaneously when the decrease in surface energy obtained by planar anchoring on the substrate outweighs the elastic energy cost of bending the layers and the increase in surface energy due to the dimple-like deformation of the LC/air interface. Regular hexagonal lattices of TFCDs have been used to create microlens arrays [61], matrices for the self-assembly of soft microsystems [85, 105, 138], lithographic templates [63], 2D charge transport models [25], and patterned functional surfaces. The ability to control the size and arrangement of TFCDs is currently under investigation; for instance, studies have employed substrates presenting different surface chemistries [25, 117, 140, 141], confinement within 1D microchannels [24, 25, 62, 109, 139], and randomly patterned planar and depressed substrates [49]. Little is known, however, about a higher level of control of TFCDs into three dimensions [32, 33]. Controlling topological defects and smectic LC phases in three dimensions is of particular interest to the generation of blue phases and

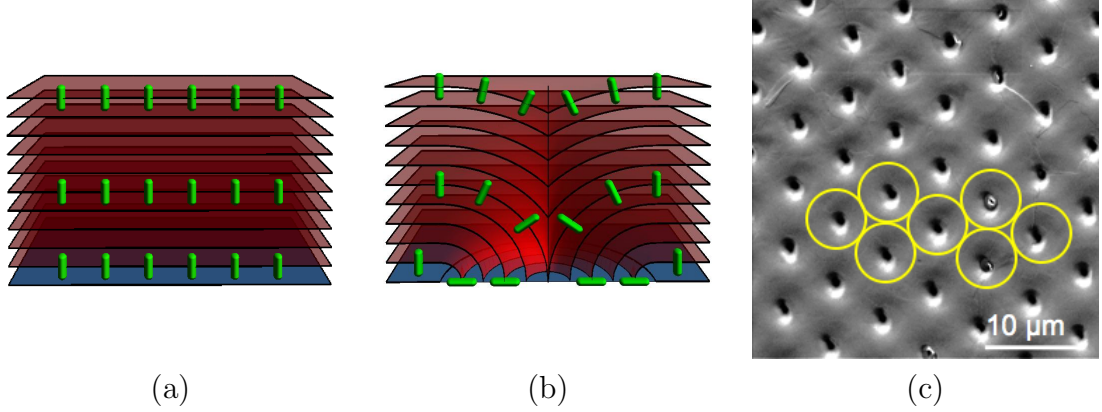


Figure 4.9: Thin-film smectic-A LC under hybrid boundary conditions on a featureless, planar substrate. (a-b) Schematic illustration of smectic configurations, with smectic layers in red, substrate in blue, and representative rod-like molecules in green. (a) Smectic ground state. (b) A toric focal conic domain. (c) Scanning electron microscopy (SEM) image of the top surface of a hexagonal lattice of TFCDs, with yellow circles added to illustrate the close-packing of cylindrical domains. Images from Supporting Information to Ref. [52].

other topologically structured materials, which will lead to possibly disruptive display technologies.

Here, we study the epitaxial assembly of SmA LCs into arrays of TFCDs with variable sizes and arbitrary symmetries (e.g., a square lattice) directed by pillar arrays. In the experiments accompanying our theoretical description, planar anchoring of LC molecules is induced by a substrate made of SU-8, a bisphenol A epoxy derivative. We show that varying the pillar dimensions (size, height, and spacing) and thickness of the LC film allows one to confine and direct the growth of each TFCD. As a result, we promote a new variety of TFCD arrays beyond the close-packed hexagonal arrangement formed spontaneously on a flat surface by controlling the size and symmetry of the underlying pillar pattern. We hope that this template-directed assembly method will benefit a number of engineering applications and advanced device concepts.

Using 1D microchannels, Kim *et al.* studied confined assembly of high density

TFCDs and reported that domain formation was strongly influenced both by the channel width W and, even more dramatically, by the channel depth H [62]. They found that an energetically stable, hexagonal array of TFCDs is formed when W and H are above the critical values, $W_c \approx 4 \mu\text{m}$ and $H_c \approx 2 \mu\text{m}$. Here, we study planar-anchoring pillar arrays with varying pillar diameter, height, spacing, and symmetry as a 3D confinement system for SmA LCs.

4.2.2 Experimental results

Figures 4.10 and 4.11 demonstrate different TFCD morphologies from the assembly of SmA LCs directed by confinement and interaction with the underlying square pillar arrays at variable length scales. The SmA LC is composed of rigid biphenyl molecules with semifluorinated chains. The geometry created by a square array of pillars is described by three parameters: S , the smallest distance between the edges of two diagonally neighboring (next-nearest-neighbor) pillars; D , the pillar diameter; and H , the pillar height. Depending on the values of these parameters and of the LC thickness h , the pillars define anchoring points for TFCDs at the centers of the pillars' top surfaces, or on the substrate positioned symmetrically between four neighboring pillars, or both.

When the LC thickness h exceeds the pillar height H by at least $1.5 \mu\text{m}$, a single TFCD forms on the circular top of each pillar (see Fig. 4.10a). No TFCDs were observed on the tops of pillars, however, when $D < 1 \mu\text{m}$. This is due to inadequate anchoring area for a circular defect. For such small TFCD diameters, the negative energy contribution from the surface term at the LC-substrate boundary is outweighed by the elastic energy cost and the increased surface area at the air-LC interface. The experimental value of this critical diameter, $D_c \approx 1 \mu\text{m}$, agrees well with our

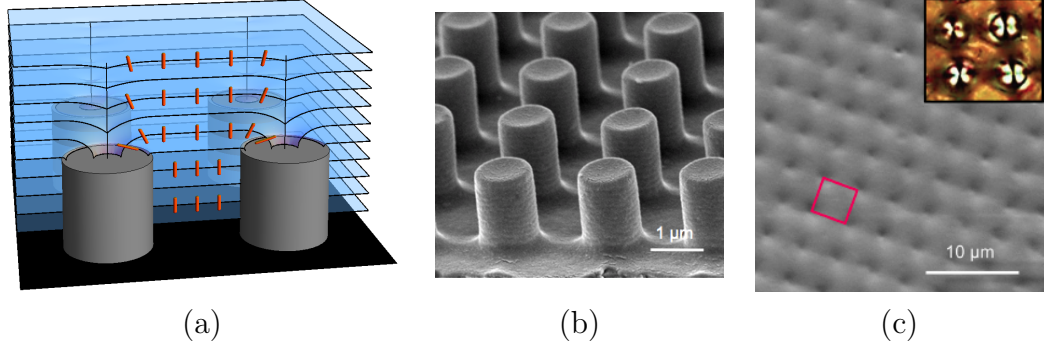


Figure 4.10: Epitaxial assembly of TFCDs on SU-8 square pillar arrays with diagonal next-nearest-neighbor separation $S < S_c$ (the critical value of S). (a) Schematic illustration of SmA LCs confined by a square pillar array with $S < S_c$. (b) Scanning electron microscopy (SEM) image of the SU-8 square pillar array with diameter $D = 1 \mu\text{m}$, diagonal separation $S = 3 \mu\text{m}$, and height $H = 1.5 \mu\text{m}$. (c) SEM image of the corresponding TFCDs assembled on the SU-8 pillar array (b) at LC thickness $h = 3.5 \mu\text{m}$. A representative square unit cell is outlined in pink. Inset: Polarized optical microscopy image at a high magnification, each cross corresponding to one TFCD.

calculations of TFCD energies in 3D pillar arrays (see Fig. 4.13b), which predict the minimum domain diameter of an energetically stable TFCD to be approximately $1.0 \mu\text{m}$. Notably, this critical diameter does not change appreciably over a wide range of $h - H$. Thus, with directing pillars of $D \geq D_c$, a square array of TFCDs could be generated that grows relatively large distances into the bulk. Indeed, we find that both the square symmetry and dimensions of the pillar array were maintained in the TFCDs for LC thicknesses up to $40 \mu\text{m}$ (Fig. 4.13a), demonstrating the long-range ordering into the bulk from surface epitaxy. Since the main aim of this study is to control the arrangements of TFCDs other than the natural close-packed structures using geometric confinement by pillars, in all experiments D and $h - H$ were kept small enough to avoid generating multiple close-packed TFCDs on the top surface of a single pillar.

The experimental data also show that the pillar array defines TFCD anchoring

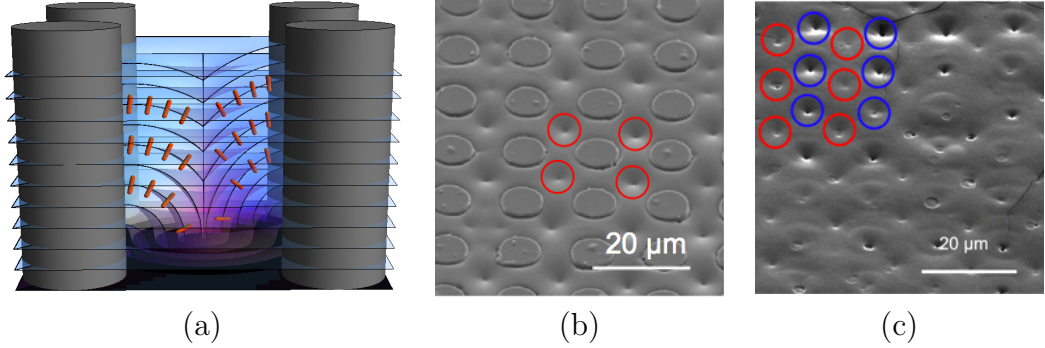


Figure 4.11: Epitaxial assembly of TFCDs on SU-8 square pillar arrays with diagonal separation $S > S_c$ and diameter $D > D_c$ (the critical value of D). (a) Schematic illustration of SmA LCs confined by a square pillar array with $S > S_c$. (b,c) Scanning electron microscopy (SEM) image of an SU-8 square pillar array with diameter $D = 10 \mu\text{m}$, diagonal separation $S = 15 \mu\text{m}$, and height $H = 7.5 \mu\text{m}$. (b) At LC thickness $h = 7.5 \mu\text{m}$, a square lattice of TFCDs (centers circled in red) forms between the pillars. (c) At LC thickness $h = 9 \mu\text{m}$, two simultaneous square lattices of TFCDs form, one with TFCDs between the pillars (centers circled in red) and one with TFCDs on top of the pillars (centers circled in blue). [52]

points on the substrate between pillars: In the center of each unit cell defined by four neighboring pillars, a single TFCD is observed when the diagonal pillar spacing S exceeds a critical value, $S_c \approx 5 \mu\text{m}$, and the LC thickness h exceeds the critical height, $h_c \approx 1.5 \mu\text{m}$. The pillars cause this transition in two ways: They limit the surface area on the substrate available to the TFCD for planar anchoring and they impose additional planar anchoring conditions along the vertical pillar sides, requiring the smectic layers to orient horizontally as they approach the pillars. As a result, when $S < S_c$, LC layers align parallel to the bottom of the substrate, filling up the spaces between pillars without forming a focal conic domain at any LC thickness. Conversely, TFCDs formed between the pillars when $S = 15 \mu\text{m} > S_c$ for $h \geq h_c$, as shown in Fig. 4.11b. When $S \geq S_c$, $D \geq D_c$, and h surpasses the pillar height H by at least $1.5 \mu\text{m}$ (i.e., $h - H \geq h_c$), TFCDs are observed to develop from both anchoring sites, the surface between pillars and the top surface of the pillars, as shown in Fig. 4.11c.

4.2.3 Calculation of smectic free energy and critical pillar diameter

We first calculate the energy of a TFCD on a planar substrate. The energy of a TFCD relative to the flat-layer state is the sum of a surface energy term and a bulk elastic term:

$$\Delta F = \Delta F_s + \Delta F_{el}.$$

The first term is the surface energy,

$$\Delta F_s = (\sigma_{\perp}^{\text{air}} A' + \sigma_{\parallel}^{\text{subs}} A) - (\sigma_{\perp}^{\text{air}} A + \sigma_{\perp}^{\text{subs}})A = \sigma_{\perp}^{\text{air}} A' + (\Delta\sigma^{\text{subs}} - \sigma_{\perp}^{\text{air}})A,$$

where A is the “undistorted” area taken up by the TFCD on the substrate; A' is the surface area of the distorted LC exposed to the air; $\sigma_{\perp}^{\text{air}}$ is the energy per unit area for molecules at the air/LC interface with orientation perpendicular to the interface; and $\Delta\sigma^{\text{subs}} = \sigma_{\parallel}^{\text{subs}} - \sigma_{\perp}^{\text{subs}}$ is the difference in energy per unit area for molecules at the LC/substrate boundary with orientation parallel vs. perpendicular to the boundary.

The second term is the bulk elastic energy, $\Delta F_{el} = \int dV \Delta f_{el}$, where the integral is over the volume of the TFCD, and the elastic energy density is the integrand of Eqn. 4.1, which we rewrite as

$$\Delta f_{el} = \frac{K_1}{2} \left(\frac{1}{R_1} + \frac{1}{R_2} \right)^2 + \frac{\bar{K}}{2} \frac{1}{R_1 R_2} + \frac{1}{2} B \varepsilon^2$$

where R_1, R_2 are the layers’ principal radii of curvature and ε is a relative compression/dilation factor. Because the smectic-A system is equally spaced, or more specifically because the length scale $\lambda \equiv \sqrt{K_1/B}$ is microscopic, we will assume that the costly compression/dilation term vanishes outside of the cores of defects, so that

$\varepsilon = 0$ throughout the region of integration. Following Kim *et al.* [62], we take $\bar{K} = 0$.

What remains is

$$\Delta f_{\text{el}} = \frac{K_1}{2} \left(\frac{1}{R_1} + \frac{1}{R_2} \right)^2.$$

The elastic energy is always positive, whereas the surface energy may be negative. In the absence of pillars, the balance of the elastic energy and surface energy determines whether a TFCD of a given radius is energetically favorable compared to the flat-layer ground state.

We now find an explicit formula for ΔF_{el} , following the method laid out in the Supporting Information to [62]. The smectic layers are assumed to distort from the horizontal ground state inside a cylindrical volume of radius a . With respect to the origin at the center of the unit cell, we first use the cylindrical coordinates z , the height above the substrate; s , the radial distance from the origin in a plane parallel to the substrate; and ϕ , an azimuthal angle. We assume that the layers are distorted into portions of tori as follows: If a layer's height above the substrate is η for $s > a$ ($0 \leq \eta \leq h$), then the layer has height function $z(s) = \sqrt{\eta^2 - (s - a)^2}$ for $s \leq a$. Fixing ϕ selects a half-plane, in which we define new planar polar coordinates (r, θ) relative to an origin at the point $(z = 0, s = a, \phi)$, with $\theta \in [0, \pi/2]$ and $r \in [0, h]$. The two principal radii of curvature (of opposite sign) are

$$R_1 = r$$

$$R_2 = -(a - r \sin \theta) / \sin \theta = r - a / \sin \theta$$

where R_1 corresponds to curvature about the circular defect, and R_2 corresponds to

curvature about the central line defect. Therefore,

$$\Delta f_{\text{el}} = \frac{K_1}{2} \left(\frac{1}{r} + \frac{1}{r - a/\sin\theta} \right)^2 = \frac{K_1}{2r^2} \left(\frac{2r - a/\sin\theta}{r - a/\sin\theta} \right)^2$$

and the area measure on each layer is $dS = r(a/\sin\theta - r) \sin\theta d\theta d\phi = r(a - r \sin\theta) d\theta d\phi$.

We divide the cylindrical region occupied by the TFCD into two: Region I, a cone of hypotenuse h , defined by:

$$\xi \leq r \leq a/\sin\theta - \xi, \quad \arcsin(a/h) \leq \theta \leq \pi/2,$$

and Region II:

$$\xi \leq r \leq h, \quad 0 \leq \theta \leq \arcsin(a/h)$$

(see Fig. 4.12a). Here, ξ defines the core size of the line defect in the center of the TFCD; its value of 3 nm is comparable to the layer spacing. Let $\rho = a/h$ and $\theta^* = \arcsin(\rho)$.

The total elastic free energy is then

$$\begin{aligned} \Delta F_{\text{el}} &= \int_0^{2\pi} d\phi \left(\int_{\theta^*}^{\pi/2} d\theta \int_{\xi}^{a/\sin\theta - \xi} dr + \int_0^{\theta^*} d\theta \int_{\xi}^{h - \xi} dr \right) r(a - r \sin\theta) \left[\right. \\ &\quad \left. \frac{K_1}{2} \frac{1}{r^2} \left(\frac{2r - a/\sin\theta}{r - a/\sin\theta} \right)^2 \right] \\ &= 2\pi K_1 h \rho \left(\ln \left(\frac{h\rho}{\xi} \right) - 2 \right) \left(\frac{\pi}{2} - \theta^* \right) - 2\pi K_1 h \rho \int_{\theta^*}^{\pi/2} d\theta \ln(\sin\theta) \\ &\quad + 4\pi K_1 h (\sqrt{1 - \rho^2} - 1) + \pi K_1 h \rho \theta^* \ln(h\rho/\xi) - \pi K_1 h \rho \int_0^{\theta^*} d\theta \ln(\rho - \sin\theta) \end{aligned}$$

To calculate the surface energy, we need the undistorted area $A = \pi r^2$ and the distorted area of the air-LC interface

$$A' = \int_0^a ds \int_0^{2\pi} s d\phi \sqrt{1 + \left(\frac{d}{ds} \sqrt{h^2 - (s-a)^2} \right)^2} = \int_0^a ds \int_0^{2\pi} d\phi \frac{sh}{\sqrt{h^2 - (s-a)^2}}$$

$$= 2\pi h^2 \left(\sqrt{1 - \rho^2} - 1 + \rho\theta^* \right).$$

The total free energy of the TFCD relative to the flat-layer state is therefore

$$\begin{aligned} \Delta F = & 2\pi K_1 h \rho \left(\ln \left(\frac{h\rho}{\xi} \right) - 2 \right) \left(\frac{\pi}{2} - \theta^* \right) - 2\pi K_1 h \rho \int_{\theta^*}^{\pi/2} d\theta \ln(\sin \theta) \\ & + 4\pi K_1 h (\sqrt{1 - \rho^2} - 1) + \pi K_1 h \rho \theta^* \ln(h\rho/\xi) - \pi K_1 h \rho \int_0^{\theta^*} d\theta \ln(\rho - \sin \theta) \\ & + 2\sigma_{\perp}^{\text{air}} \pi h^2 \left(\sqrt{1 - \rho^2} - 1 + \rho\theta^* \right) + (\Delta\sigma^{\text{subs}} - \sigma_{\perp}^{\text{air}}) \pi h^2 \rho^2. \end{aligned}$$

This energy as a function of the domain radius a is plotted in Fig. 4.12b for LC thickness $h = 3 \mu\text{m}$. Material constants used in the calculation, corresponding to the SmA LC used in the experiments, include the splay elastic constant $K_1 = 5 \times 10^{-11} \text{ N}$, the defect core size $\xi = 3 \times 10^{-9} \text{ m}$, and the energy per unit area for molecules oriented normal to the LC/air interface $\sigma_{\perp}^{\text{air}} = 20 \times 10^{-3} \text{ N m}^{-1}$. The energy per unit area for molecules oriented parallel vs. normal to the LC/SU-8 interface is $\Delta\sigma^{\text{subs}} = -1.1 \times 10^{-3} \text{ N m}^{-1}$; this is found by requiring that the calculated TFCD energy allow energetically stable TFCDs only for values of $h \geq h_c = 1.5 \mu\text{m}$.

In Fig. 4.12c, we consider the case where a TFCD is confined on top of a pillar of radius $D/2 = 1 \mu\text{m}$. When the domain radius a is less than $D/2$, the free energy is the same as in the planar substrate case. However, for $a \geq D/2$, the energy benefit of planar anchoring on the pillar top ceases to increase with increasing a ; the surface energy term is replaced by

$$\Delta F_s = \sigma_{\perp}^{\text{air}} (A' - A) + \Delta\sigma^{\text{subs}} \pi (D/2)^2.$$

Meanwhile, the elastic energy cost and the surface tension at the LC-air interface

continue to increase with increasing a , so that the total free energy increases monotonically for $a \geq D/2$. As a result, we know with certainty that the free energy of an isolated TFCD is minimized by $a = D/2$ (for sufficiently large h), meaning that the pillar defines the lateral size of the TFCD.

In Fig. 4.13b, we plot the TFCD energy on a planar substrate as a function of domain radius a at various values of the LC thickness h . We see from this plot that the value of a where ΔF changes from positive to negative is approximately $0.5 \mu\text{m}$ for all LC thicknesses $h \geq 2 \mu\text{m}$. This size gives the predicted critical pillar diameter $D_c = 1 \mu\text{m}$ below which the flat-layer state replaces the TFCD, which agrees well with the experimentally observed value. A very similar calculation predicts the same value for the critical diagonal spacing S_c between the sides of next-nearest-neighbor pillars for TFCDs confined in the spaces between pillars, though the experimental value of S_c is mysteriously far larger. The details of the calculation for S_c are somewhat tedious and are omitted here in the interest of brevity, but they can be found in the Supporting Information to [52].

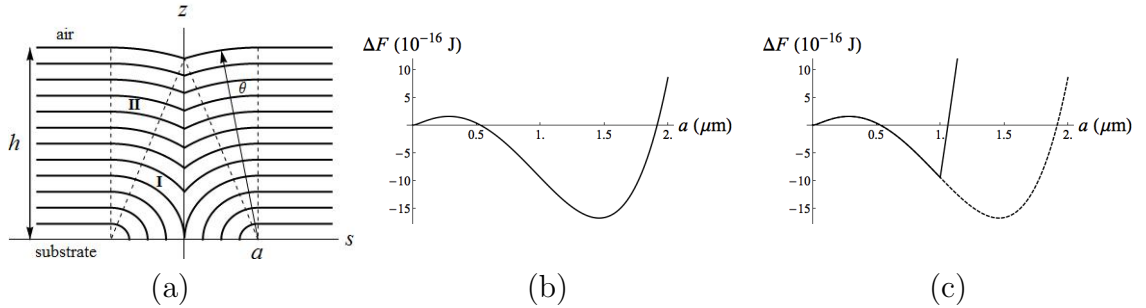


Figure 4.12: Calculated free energy of a single TFCD as a function of domain radius a . (a) Schematic diagram showing calculation parameters. (b) Free energy of a TFCD on a planar substrate with LC film thickness $h = 3 \mu\text{m}$. (c) Free energy of a TFCD confined on a pillar of radius $1 \mu\text{m}$ (solid curve) and height $H = h - 3 \mu\text{m}$, with the dashed curve showing the energy from (b). [52]

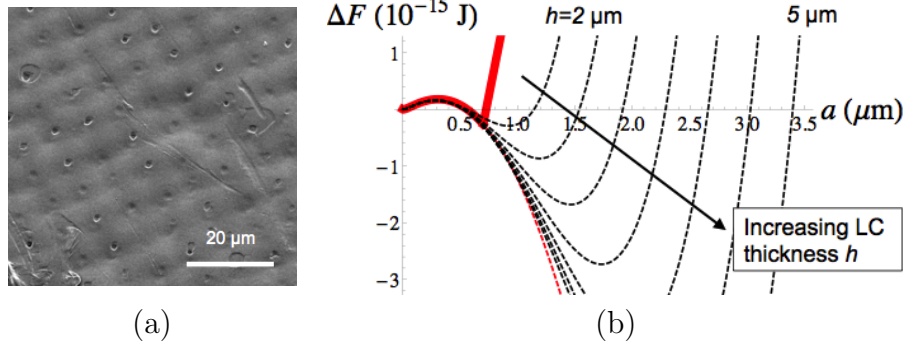


Figure 4.13: Insensitivity of epitaxial assembly to LC thickness. (a) SEM image of a square array of TFCDs assembled in a SmA LC film of thickness $h = 40 \mu\text{m}$ on an SU-8 square pillar array with $D = 5 \mu\text{m}$, $S = 5 \mu\text{m} \sim S_c$, and $H = 2.5 \mu\text{m}$. Image courtesy of A. Honglawan. (b) Dashed black curves: TFCD free energy relative to the flat-layer state versus domain radius a for a flat substrate, with LC thickness h increasing from $2 \mu\text{m}$ to $5 \mu\text{m}$ by increments of $0.5 \mu\text{m}$. Red dashed curve: The same energy in the limit $h \rightarrow \infty$. Thick red curve: The free energy for a TFCD of radius a confined on top of a pillar with radius $0.6 \mu\text{m}$, in the limit $h \rightarrow \infty$. Adapted from Fig. S7 in the Supporting Information to Ref. [52].

4.2.4 Discussion

Our results demonstrate three important features with regard to epitaxial assembly of LC molecules confined and directed by an SU-8 pillar array. First, it is possible to alter the naturally occurring close-packed lattice of the TFCD arrays via anchoring on a non-planar boundary. The effect is not unique to square lattices; a non-close-packed TFCD lattice was also generated experimentally by a hexagonal lattice of pillars [52].

Second, defect size and spacing can be controlled simply by varying the dimensions of the directing pillars, which enables generation of TFCD arrays with defect size and spacing smaller than previously observed in the same material at any given LC thickness ($\approx 5 \mu\text{m}$ on treated and untreated flat Si surfaces and $\approx 2.6 \mu\text{m}$ in a 1D microchannel [49] for the smallest tested $h = 5 \mu\text{m}$). The possibility of down-scaling the spacing between defects is advantageous for possible LC-based device fabrication.

The third and most important implication of pillar-directed epitaxial assembly of

LCs is the conservation of the symmetry and size scale of TFCD arrays at relatively large LC thickness, experimentally observed up to 40 μm (Fig. 4.13a) despite the fact that on a flat non-patterned substrate the domain size scales roughly as the film thickness [48, 49]. This behavior is a direct result of LC confinement and epitaxial growth of individual TFCDs in which the geometry of the pillar sets the upper limit for the size of a domain by imposing a sharp energy barrier to further domain growth. Furthermore, the minimum allowable domain size is also nearly independent of LC thickness, as predicted by the energy model: In Fig. 4.13b, we plot the calculated energy of a TFCD relative to the flat-layer state as a function of domain radius. The energy curve crosses zero at approximately the same domain radius (0.5 μm) at any $h \geq 2 \mu\text{m}$, setting the predicted S_c and D_c independently of h . While this finding does not show that the TFCD is the state with globally minimizing free energy at all h , the calculation does show that the simplest alternative state of planar layers remains higher-energy than the epitaxially assembled TFCD lattice at arbitrarily large h , in agreement with the experimental robustness of the lattice at $h/a > 10$. As a result, the simple proof-of-principle experiments and modeling presented here provide a viable technique to generate a uniform array with arbitrary symmetry of equal-sized TFCDs that extend into the bulk.

4.2.5 Conclusion

We have demonstrated epitaxial assembly of focal conic domain arrays in SmA LCs using substrates of patterned topography. The 3D nature of the pillar array is crucial to confine and direct the formation of toric focal conic domains on the top of each pillar as well as between neighboring pillars. Independently of LC thickness (above a critical thickness h_c), the pattern of pillar arrays determines the final crystal habit

of the TFCD array: both highly ordered square and hexagonal array TFCDs were obtained. The epitaxial approach presented here offers an entirely new and promising organizational principle for smectic LC systems using simple topographic substrates. In turn, it may lead to the formation of more complex LC phases in 3D that are critical to the advancement of LC-based electronic and optical devices [32, 33], and perhaps generation of novel materials when incorporating functional units such as nanoparticles, nanocrystals, and carbon nanotubes into the LC layers.

4.3 Hierarchical assembly of elliptic-hyperbolic focal conic domains on topographically patterned substrates

4.3.1 Introduction

In liquid crystals, average local molecular orientations assume geometries that can be controlled by boundary conditions [17, 78] and external fields [58, 90], and the resulting mechanical and electric anisotropies of LCs provide powerful tools in controlling the propagation of light and the assembly of soft materials [71, 77, 91, 94, 104, 121]. A quintessential example is the blue-phase LC organized around a 3D disclination network [27, 107]; as a display component, it offers rapid response time without surface alignment [42]. The ability to tailor LCs with complex, topologically structured geometries will be necessary for the next generation of display technologies and beyond.

In smectic-A LCs, focal conic domains have gone from mere geometric curiosities to the focus of much attention in recent years as an enabling technological tool [49, 59, 138, 140]. Toric focal conic domain arrays have been used to fabricate functional surfaces [61, 64], to direct the self-assembly of soft microsystems [89, 105, 138], to template

lithographic patterns [63], and to enhance charge transport in photovoltaics and transistors [100]. So far, most attention has been devoted to the precise manipulation of the locations of FCDs in 2D lattices by confining individual domains within small regions through both chemical and topographical patterning of the substrate [49, 59, 62]. For device applications, it is desirable to produce FCDs with prescribed arrangements in 2D and 3D over large regions and to scale down the LC patterning.

Here, we present a unique level of control to direct the growth of FCD arrays by inducing hierarchical assembly of multiple FCDs centered at the edges of micropillars with nonoverlapping elliptical focal curves. Below a critical pillar height, the confining effects produced by anchoring conditions on the pillar sides are diminished, but the LC elastic and surface energies remain sensitive to the positions of the FCDs on the patterned substrate. Consequently, multiple FCDs “share” a single pillar and self-assemble in a hierarchical manner; changing the shape of the pillars promotes a variety of nontrivial FCD arrangements. We use a simple energetic model for the smectic LC that predicts the transition between this hierarchical assembly and topographic confinement of FCDs as the pillar height varies. Additionally, we exploit the size and spacing of the pillar array to tune the eccentricity, e , of the FCDs. In the case of TFCDs with circular focal curves, $e = 0$, whereas parabolic FCDs have $e = 1$. The ability to tune the eccentricity allows the creation of a versatile assortment of asymmetric FCD arrays, the first step toward the formation of 3D networks and more complex geometries. Finally, we present a geometric ansatz for the layer configurations that allows us to numerically investigate the energetic effects of nonzero eccentricity. These calculations are consistent with the observed nonzero eccentricity in the samples.

In a thin film geometry, smectic layers spontaneously assemble into FCDs in response to antagonistic boundary conditions, with homeotropic anchoring at the air interface and degenerate planar anchoring at the substrate. We now write the

total free energy of the system as a sum of three terms, the elastic energy of the LC and (separately) the surface energies at the air and substrate interfaces: $\Delta F = \Delta F_{\text{el}} + \Delta F_{\text{air}} + \Delta F_{\text{subs}}$, where ΔF_{subs} is highly dependent on topography of the substrate and where we measure the free energy with respect to a reference state of horizontal flat layers. In Section 4.2, we studied the uses of circular micropillar arrays of SU-8 to confine SmA LCs both by limiting the surface area on the substrate available to each FCD with degenerate planar anchoring and by imposing frustrating degenerate planar anchoring conditions along the vertical pillar sides [52]. It is natural to ask (i) how the FCD arrangement changes when the pillars become short enough so that their vertical sides do not present an insurmountable barrier to local FCD anchoring, and (ii) how the arrangement of FCDs and the smectic layer structure depend on pillar shapes and lateral dimensions. Previous research on nematic LCs in micropillar arrays has highlighted the importance of pillar shape in determining the texture and controlling the placement of defects, demonstrating an inherently bistable LC display [65, 66].

4.3.2 Experimental results

Three sets of short (height $H = 1 \mu\text{m}$) SU-8 micropillar arrays were constructed with differing cross-section (circular vs. elliptical; Fig. 4.14 a1-c3). The SmA LC film thickness cast on pillars was kept constant ($h \approx 7 \mu\text{m}$) so that $h - H > h_c \approx 1.5 \mu\text{m}$, the minimum film thickness at which FCDs form (using the same SmA LC material as in Section 4.2). In the case of circular pillars, the center-to-center spacing between pillars along a diagonal of the square lattice is $S = 12 \mu\text{m}$, roughly twice the TFCD diameter ($7.2 \mu\text{m}$) that minimizes the free energy of a single TFCD on a substrate with degenerate planar anchoring at the same h . As seen in Fig. 4.14 a2 and a3, four FCDs formed on each pillar with their centers lying on the lattice diagonal and near

the pillar edges. On elliptical pillars, the number of FCDs on each pillar decreased from four, to three (aspect ratio $A/B = 1.2$; Fig. 4.14 b2 and b3), to two ($A/B = 2.5$; Fig. 4.14 c2 and c3), which is in sharp contrast to the confinement effect with taller pillars ($H \geq 1.5 \mu\text{m}$) explored in Sec. 4.2 [52], where FCD centers were positioned only in the centers of pillars or evenly spaced between neighboring pillars (see schematics in Fig. 4.15). Simply reducing the height of pillars effectively changes the interaction between pillar sides and FCD centers from repulsive to attractive, thereby promoting “edge-pinning” of FCD centers to the boundaries of short pillars. As the pillar’s minor axis length decreases, fewer FCDs are packed with their centers on the pillar edge.

To further elucidate the edge-pinning effect, an array of $1 \mu\text{m}$ -tall, Y-shaped pillars was prepared with each side of length $30 \mu\text{m}$, a much larger lateral scale than the cylindrical pillars. Under crossed polarizers, the Maltese cross patterns of each FCD were clearly distorted at the edges of the Y-shaped pillar (Fig. 4.14d). The distortion was even more apparent in the 3D topography of the top surface imaged by atomic force microscopy (AFM; Fig. 4.14 d4): the surface was depressed at the periphery of the Y pattern but relaxed in the middle to the height of the surrounding flat region, confirming that the attraction of FCD centers to pillar edges is strong enough to disrupt the assembly of close-packed hexagonal lattices of TFCDs. The hierarchical nature of the epitaxial assembly leads to geometric relations among the orientations of FCD groups from one pillar to the next over regions spanning the whole pillar array. For example, in Fig. 4.14a the centers of the four FCDs surrounding each circular pillar form a square aligned with the substrate patterning’s lattice directions consistently from pillar to pillar. Different pillar shapes yield distinct hierarchical arrangements of FCDs. An especially interesting case is presented by the most eccentric pillars in Fig. 4.14c, where the two FCDs on each pillar are connected by a line slightly rotated off the major axis of the ellipse. This pattern breaks mirror symmetry along the pillar’s

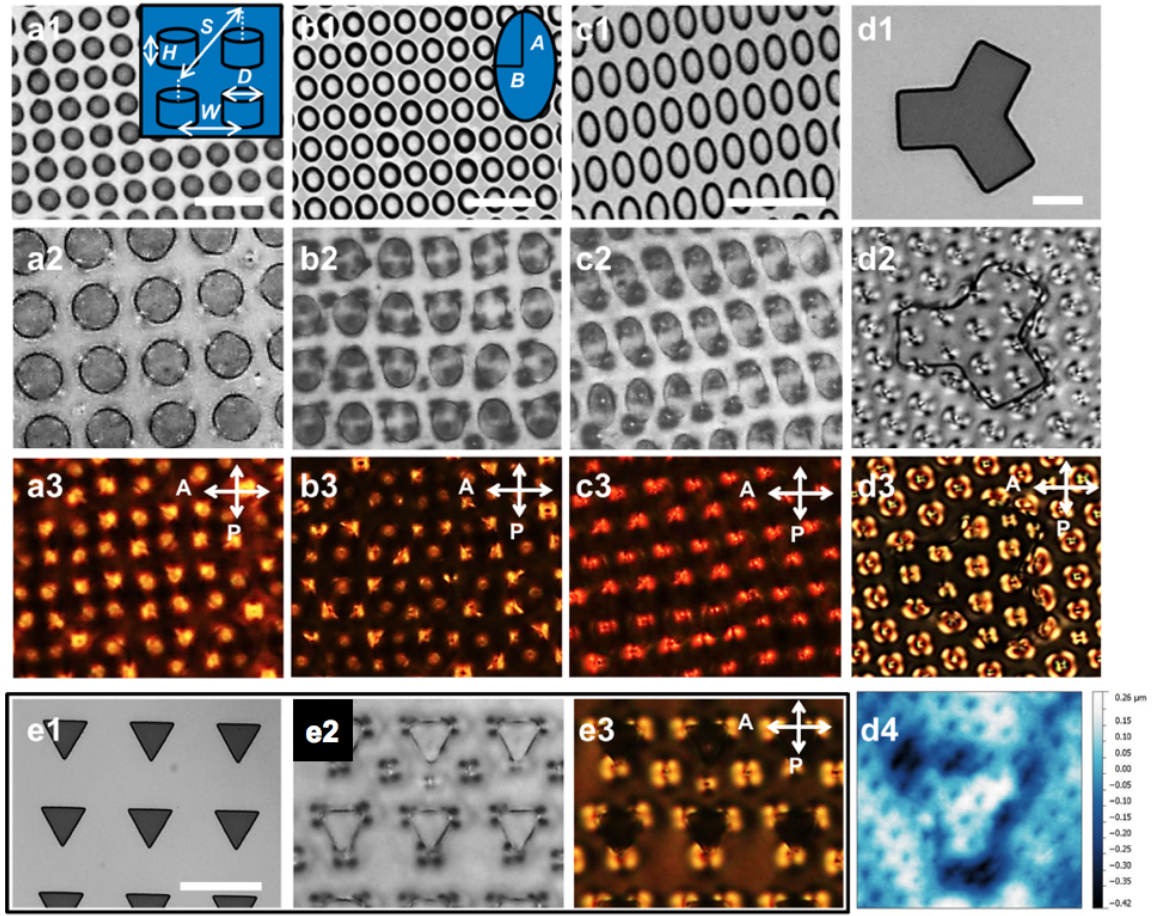


Figure 4.14: Formation of FCD arrays on 1 μm -tall SU-8 pillars with variable sizes and shapes. Optical images of top view of SU-8 pillars (a1–e1) and LC defect textures on pillars without (a2–e2), and with crossed polarizers (a3–e3). (Scale bars: 20 μm .) (a) Circular pillars with diameter $D = 5.5 \mu\text{m}$, the center-to-center spacing of the nearest pillars $W = 8.5 \mu\text{m}$, and the diagonal center-to-center distance of the next-nearest pillars $S = 12.0 \mu\text{m}$. (b) Elliptically shaped pillars with major axis length $2A = 6.2 \mu\text{m}$, minor axis length $2B = 5.2 \mu\text{m}$, $W = 7.4 \mu\text{m}$ (along the shorter lattice vector), and $S = 12.2 \mu\text{m}$. (c) Elliptically shaped pillars with $2A = 7.0 \mu\text{m}$, $2B = 3.4 \mu\text{m}$, $W = 6.3 \mu\text{m}$ (along the shorter lattice vector) and $S = 11.8 \mu\text{m}$. (d) Y-shaped post with equal peripheral dimension of 30 μm at all sides. (e) Triangularly shaped pillars with each side of length 10 μm . The LC thickness h is $\approx 7 \mu\text{m}$ (a–c) and $\approx 10 \mu\text{m}$ (d and e). (d4) AFM height profile of LC defects assembled on a Y-shaped post with equal lateral dimensions of 30 μm . [51]

major axis, and the choice of ground state is consistent over regions spanning tens of pillars, even though the substrate patterning does not break this symmetry. In this way, simply varying the pillar height and shapes causes transforms of the arrangements of FCDs into anisotropic patterns, exhibiting order over large regions.

The importance of pillar shape to hierarchical assembly of FCDs is further evidenced by the attraction of domains to the more highly curved regions of convex pillar edges shown in Fig. 4.14c. We attribute this effect to the strong steric repulsion between the neighboring FCDs. Two FCDs will prefer to position their centers as far apart as possible while remaining tangent and keeping their centers pinned to the pillar edge. The effective attraction of FCD centers to pillar “corners” is especially evident in pillars with triangular cross-sections (Fig. 4.14e).

4.3.3 Surface confinement/edge-pinning transition

The transition from surface confinement to edge-pinning results from a delicate balance of the elastic (layer curvature) energy in the bulk and the surface energy of both the LC/air and the LC/substrate interfaces (details will be presented in Section 4.3.5). Degenerate planar anchoring along the pillar’s vertical surface imposes an energy penalty for rod-like molecules tilted out of the vertical direction unless the molecule happens to tilt in the tangent plane to the pillar edge. For tall pillars (empirically, $H \geq 1.5 \mu\text{m}$), the substrate surface energy favors smectic layers horizontal at the pillar edge, a condition that is not satisfied in the interior of an FCD. Thus, the surface energy promotes confinement, with the FCD centers as far as possible from the pillar edges. In contrast, the elastic energy is concentrated most strongly near the elliptic and hyperbolic defect curves of the FCD, the focal set of the Dupin cyclides. This effect would be further enhanced by including a core energy for the defect curves;

in this analysis, we have omitted this core energy because its form is uncertain and because a transition from confinement to edge-pinning can be predicted by considering only the bulk elastic energy. If the dimensions of the pillar and the LC thickness are chosen so that two or more FCDs form for each pillar, then the elastic energy often favors “hiding” the lower portion of the hyperbolic defect curve inside of the pillar, removing a significant fraction of the elastic energy. The role of the pillar’s top surface is more subtle, but the degenerate planar anchoring conditions on this surface generally favor the edge-pinning configuration for short pillars. The balance of these energies promotes edge-pinning as the confining effects of the pillar diminish with decreasing pillar height.

To understand the transition from confinement to edge-pinning with decreasing pillar height, we use numerical energy calculations to investigate a simplified scenario: two TFCDs and one pillar in the shape of a circular cylinder. Fig. 4.15 presents the calculated free energy ΔF relative to the reference state of equally spaced, horizontal planar layers, as a function of the relative position of the pillar center along the line connecting the two TFCD centers (see Sec. 4.3.5). We set the pillar radius to 1.1 times the TFCD radius, so that it is possible to hide portions of both straight-line focal curves within the pillar. The LC thickness is $10\text{ }\mu\text{m}$ and the TFCD radius is $5.2\text{ }\mu\text{m}$, chosen to minimize the analytic expression for ΔF on a flat substrate [64]. For all values of H , local minima in ΔF are seen when the pillar is centered directly at the center of either TFCD, and when the pillar is positioned symmetrically between the two TFCDs. The results reveal that the global minimum changes abruptly as H decreases: for $H > 2\text{ }\mu\text{m}$, the energy is minimized by centering the pillar at the center of either TFCD, corresponding to a confinement effect. For shorter pillars, the global minimum switches to a symmetric configuration of two TFCDs “sharing” a pillar equally, with their centers near the pillar edges. This calculation correctly captures the

transition of FCDs from confinement to edge-pinning with decreasing pillar height.

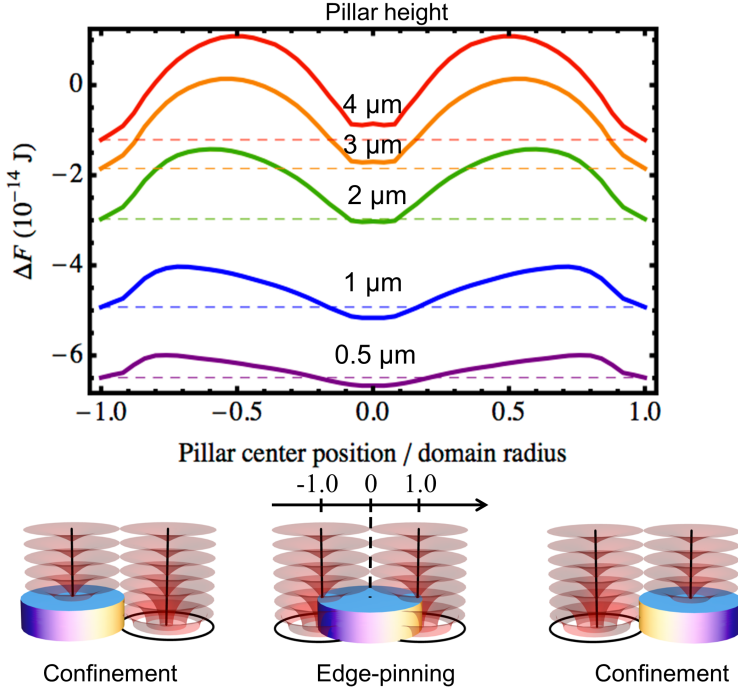


Figure 4.15: A plot of the numerically calculated free energy ΔF , relative to the reference state of planar layers, as a function of the relative position of the circular pillar center along the line connecting the two TFCD centers for different pillar heights ($H = 0.5 – 4 \mu\text{m}$). The TFCD radius is set to $5.2 \mu\text{m}$ at LC thickness $h = 10 \mu\text{m}$ on the pillar array with radius of $5.72 \mu\text{m}$. Schematics illustrate the TFCD arrangements on the pillar with edge-pinning and confinement effects.

The edge-pinning regime provides a geometric means to tune the eccentricity of FCDs. By comparing the AFM height profile of FCD arrays formed on circular and elliptical pillar arrays to LC textures observed in optical and scanning electron microscopy (SEM) images (Fig. 4.16), we find two surprising features. First, the LC thickness is typically smaller over the pillar, where the substrate is raised, than over the lower regions between pillars. Along a line that passes through successive cusp-like indentations marking the terminations of hyperbolic defects at the air interface, we measure an alternating set of large and small arcs on the topmost layer. Second,

relatedly, there is a lack of axial symmetry about the cusp. The absence of axial symmetry clearly implies that the edge-pinned FCDs are not toric; their eccentricity is nonzero.

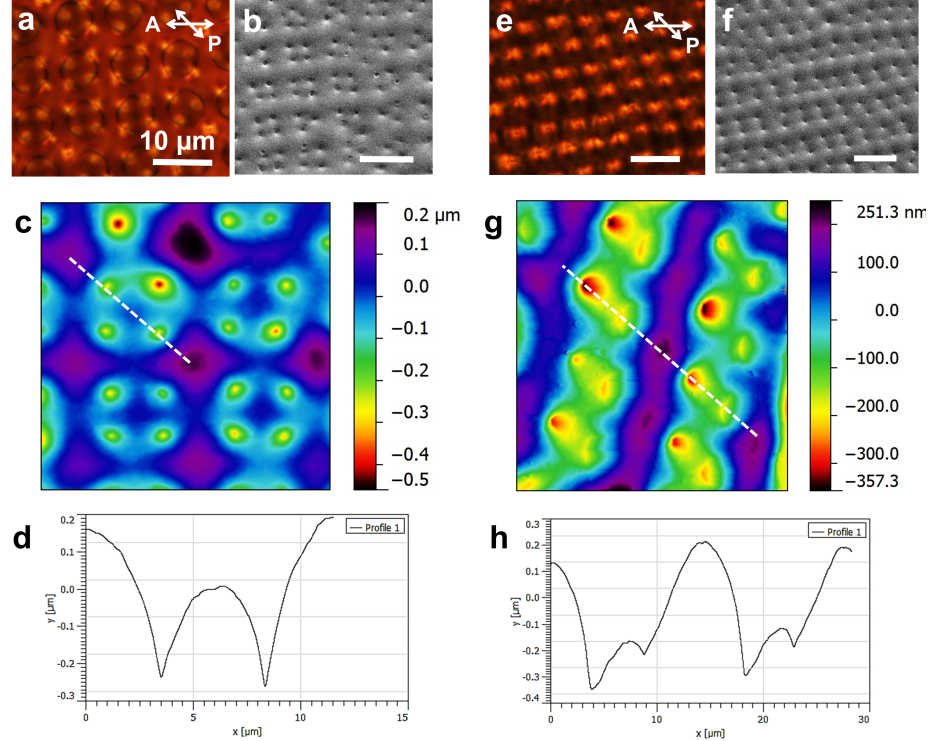


Figure 4.16: Surface characterization of FCD formation on the circular (a–d) and elliptical pillar arrays (e–h); the former correspond to the pillars seen in Fig. 4.14a, the latter to Fig. 4.14c. Optical images (a and e) reveal a defect texture with the polarizer and analyzer at a relative angle of 45° , and the corresponding surface topography of FCDs arrays obtained from SEM (b and f). (c and g) 3D maps of the surface of the LC films extracted from AFM measurements based on their height profiles with color representation of relative thickness of the film. (d and h) Plots of the height profiles along the dashed white lines in c and g.

FCDs with zero and nonzero eccentricity are illustrated in Fig. 4.17a-c. Nontoric FCDs select a particular direction in the plane given by the direction in which the hyperbola bends. In the topmost-layer profile, the periodic alternation of small and large arcs suggests the following model: the hyperbolae face inward toward the pillar

centers, and thus face away from each other over the spaces between the pillars (Fig. 4.17d).

Why should nonzero eccentricity be favored in the edge-pinning regime? We propose an answer based on geometry. Consider the square array of circular pillars (Fig. 4.14a), where S slightly exceeds 4 times the pillar radius of $2.75\text{ }\mu\text{m}$. Consequently, TFCDs in a symmetrical arrangement with their centers pinned to the edges of one pillar could not possibly have their circular focal curves tangent to those of the corresponding TFCDs of the neighboring pillars. A small gap would be left in between, creating extra area on the substrate with unfavorable, homeotropic anchoring rather than the preferred degenerate planar anchoring.

However, the FCD array can close the gap by shifting to small but nonzero eccentricity. Like the TFCD, an FCD of any eccentricity enjoys degenerate planar anchoring on a level surface in the area enclosed by its ellipse. Because the hyperbolic defect passes through the focus of the ellipse rather than through its center, nonzero eccentricity can shift the FCD center so that the ellipse is tangent to the ellipse of a neighboring pillar's FCD, while maintaining edge-pinning of the hyperbolic defect. Based on the dimensions presented for Fig. 4.14a, this geometric model predicts an eccentricity, $e = 0.12$, which agrees reasonably well with a separate estimate $e = 0.08$, based on the AFM data in Fig. 4.16c,d (see Sec. 4.3.5). Furthermore, nonzero eccentricity can decrease the elastic energy by bending the hyperbolic focal curve toward the pillar center, thus hiding more of the FCD's high-curvature central region inside the pillar.

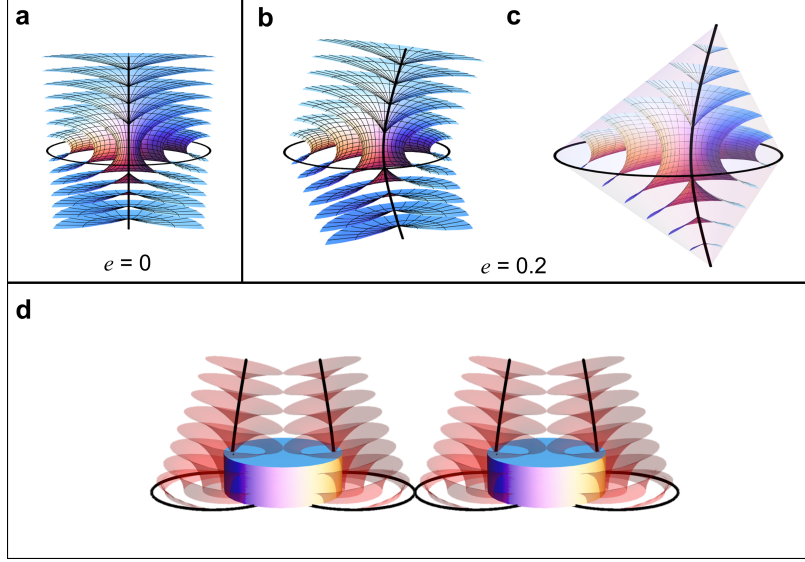


Figure 4.17: Schematic illustration of internal structures of FCDs with zero (a) and nonzero (0.2) (b and c) eccentricity in regions bounded by a cylinder (a and b) or a cone configuration (c). (d) Representation of a possible arrangement of FCDs with nonzero eccentricity on circular pillars with the edge-pinning effect.

4.3.4 Filling the smectic regions between focal conic domains

The regular assembly of FCDs in groups of two to four poses an interesting problem as to how the LC molecules fill the interstices between the domains. For TFCDs, the interstices are filled by horizontal layers, onto which the layers of the TFCD match with continuous layer normals on a right cylinder containing the circular focal curve. FCDs of nonzero eccentricity oriented in different directions cannot be joined by planar layers. Instead, elliptic-hyperbolic FCDs typically assemble in groups with their hyperbolic focal curves, or their imagined extensions, all intersecting at a single point P , and with the elliptical focal curves tangent to their neighbors, as prescribed by the law of corresponding cones. Friedel [40] showed that FCDs associated in this way can be joined, with continuous layer position and normal direction, across bounding surfaces in the form of right circular cones that have apices at P and that include the elliptical

focal curves.

It is geometrically possible for smectic layers to fill the space immediately outside of these “corresponding cones” with portions of spheres concentric about P , again without discontinuity in layer position or normal direction, as demonstrated by Sethna and Kléman [115]. In a model originally proposed by Bragg [16] and confirmed in experiments by Lavrentovich [75], the sample is divided into quasi-pyramidal regions, each filled by FCDs and spheres organized around a given point P , as well as wedges between the pyramids, which are filled by portions of still more FCDs. This construction fills a region entirely with layer configurations possessing only zero- and one-dimensional focal sets. In thin-film smectics, there is no energetic prohibition of more general layer configurations with 2D focal sets outside the FCDs, provided that the focal sets of these interstitial regions lie below or above the sample as “image cusps” that are not physically realized in the smectic. In this sense, confinement dramatically expands the range of possible layer geometries even in an ideal system.

To quantitatively estimate the effect of nonzero eccentricity on the free energy, we propose an ansatz configuration for the layers in the case of four FCDs around a circular pillar as in Fig. 4.14a. (We focus on this case for modeling because it enjoys the highest symmetry.) Our ansatz employs the conical bounding surfaces of Friedel [40] but not the concentric spheres of Sethna and Kléman [115] or Bragg’s pyramids [16]. First, we choose a point on the hyperbolic focal curve to serve as the apex of a right circular cone C that passes through all points on the elliptical focal curve. C provides a boundary separating the FCD on the inside from some other layer configuration on the outside (Fig. 4.18a).

However, how will we bridge the gaps between the cones? Because C consists of generators for the Dupin cyclides, the layers meet the cone at right angles. Generators are straight lines consisting of surface normals to parallel layers, which remain constant

from layer to layer in the normal direction and point toward the center of curvature. Consider a point E_u on the elliptical focal curve parameterized by $u \in [0, 2\pi)$ (see Sec. 4.3.5), and the subset of the FCD with one center of curvature at E_u , the other center lying on a variable point on the hyperbola (Fig. 4.18b). This subset consists of circular arcs concentric about E_u . Continuity of the layer normal across the bounding cone requires that the cone generator through E_u is also the generator of the layers just outside the cone. We must choose a new center of curvature along the same generator. A natural choice is the intersection I_u of the cone generator with the corresponding generator of the neighboring FCD's bounding cone. This intersection lies somewhere below the sample. The simplest reasonable construction is to fill in the regions outside the bounding cones with circular arcs concentric about I_u , in the plane containing the cone generator through E_u and the cone normal direction along this generator. When the construction is repeated for all $u \in [0, 2\pi)$, we obtain a set of parallel surfaces that matches the FCD layers along the boundary cone and bridges the space between FCDs in a manner compatible with the observed fourfold symmetry (Fig. 4.18c). Using this construction, we can produce simulated AFM data for the topmost layer that agrees reasonably well with the experimental data (compare Figures 4.18d and 4.16c). In combination with the structure of the FCD itself, this ansatz provides a family of space-filling smectic layer geometries parameterized by the eccentricity. We numerically evaluate the elastic- and surface-energy integrals for these geometries and plot the total ΔF as a function of e in Fig. 4.18e. This plot shows that ΔF for eccentricity $e \lesssim 0.04$ is comparable to that at $e = 0$, whereas ΔF increases nearly monotonically for larger e . This result is consistent with the experimental observation of stability of nonzero eccentricity on the order of 0.1. Adding a core defect energy for the hyperbolic focal curve would decrease the free energy at $e \gtrsim 0.1$ relative to that at $e = 0$, due to a portion of the hyperbola disappearing inside the pillar as discussed above.

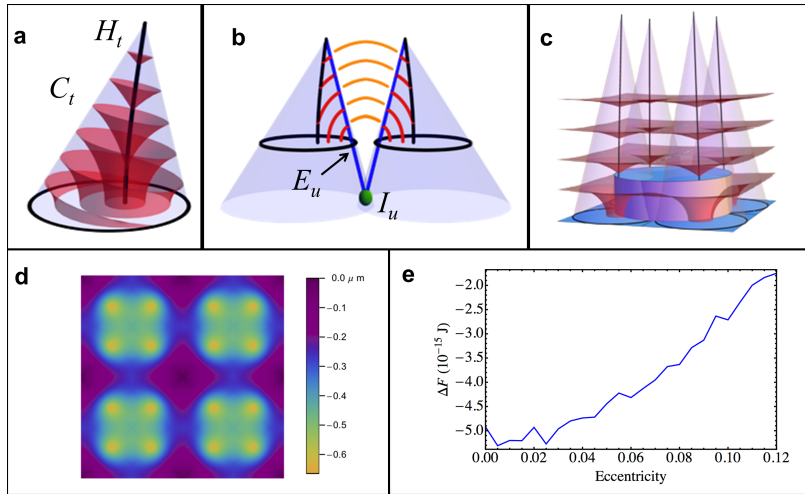


Figure 4.18: Schematic illustrations of (a) a single FCD bounded by a cone, (b) a smectic layer construction bridging between two bounding cones with circular arcs concentric about I_u , in the plane containing the cone generator through E_u and the cone normal direction along this generator, and (c) a complete layer construction of four FCDs surrounding a pillar for all $u \in [0, 2\pi)$ based on B. (d) A 2D map of the top-most surface of (c) with a color representation of surface height. (e) A plot of the total free energy of the LC geometry in C as a function of the eccentricity of the FCDs. [51]

Could this system alternatively be modeled by the pyramids and wedges construction of Bragg? In the case of four FCDs around a circular pillar, we could imagine constructing an indented square pyramid around each pillar, containing four FCDs whose hyperbolae intersect at the pyramid's apex, along with portions of concentric spheres (Fig. 4.19a). A roughly tetrahedral wedge containing a portion of an FCD is inserted between every pair of neighboring pyramids (Fig. 4.19b,c). Finally, each four-corner meeting point of the pyramids' bases on the substrate also serves as the apex of an inverted square pyramid filled only with concave-down portions of spherical layers (Fig. 4.19d), forming the purple regions in Fig. 4.16c. The resulting structure is illustrated for a single layer in Fig. 4.19e. This model predicts a concave-up region above the center of every pillar, where the layers would form portions of spheres concentric about a point above the sample. It is possible that the slight depression in the middle of the smaller arc of Fig. 4.16d is evidence of such a concave-up region. However, the concave-up regions in the AFM data are no more than $1\text{ }\mu\text{m}$ in width, implying that the ellipse eccentricity exceeds 0.7, far greater than our estimate $e \approx 0.080$ based on calculations independent of our model for the interstices (see Sec. 4.3.5). Furthermore, similar slight depressions are arguably visible in Fig. 4.16h, for the case of two FCDs around elliptical pillars, but are not expected in a model using Sethna-Kléman filling with concentric spheres [115]: If the bounding cones of FCDs are tangent to those of their neighbors, then the white dashed line in Fig. 4.16g passes from one FCD to the next without going through a region of spherical layers over the pillars. With maximum parsimony in mind, we propose our model, which fits the geometry and eccentricity more readily.

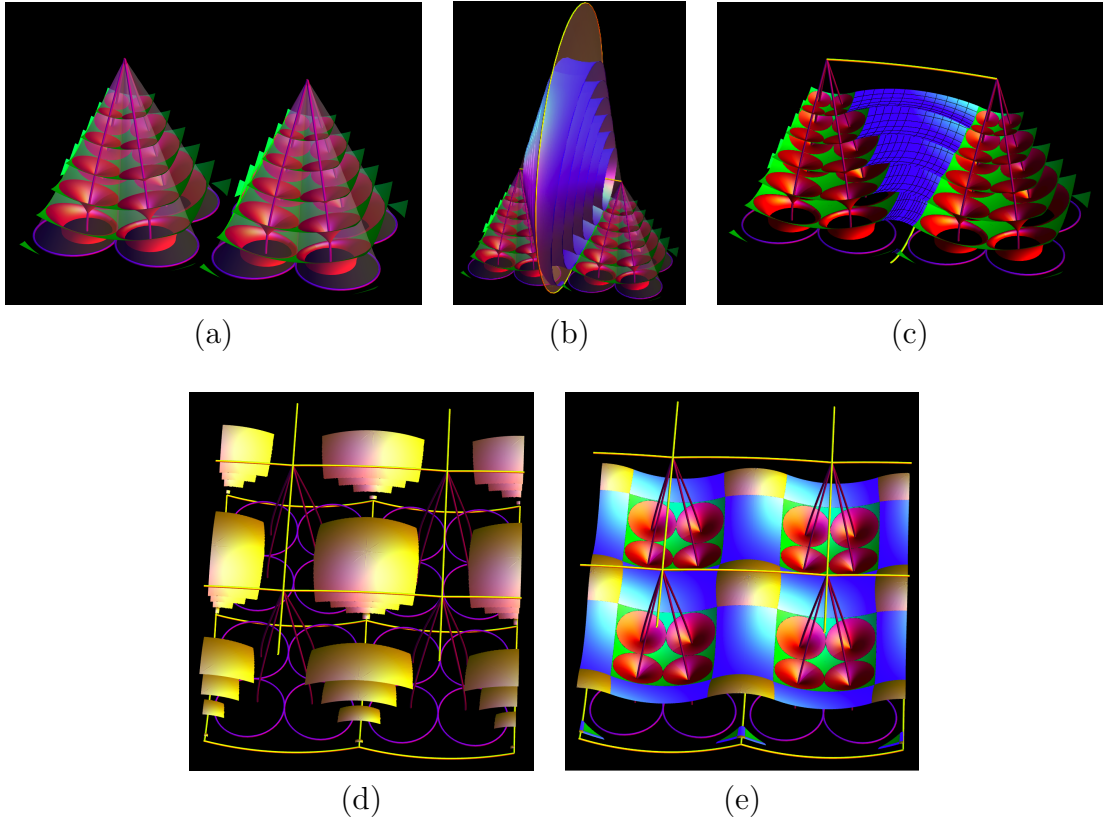


Figure 4.19: A “classical” model for the filling of smectic layers between FCDs in the geometry of Fig. 4.14 a, based on the theories of Bragg [16], Sethna and Kléman [115], and Lavrentovich [75]. (a) Four FCDs (red surfaces) assembled around a micropillar self-organize according to the law of corresponding cones, with their ellipses (magenta) tangent to those of their neighbors and their hyperbolic focal curves (red) converging at a point above the pillar’s center. The intersection of their hyperbolae serves as the center of a family of (portions of) spherical layers that join together the four FCDs to form a “pyramid”. (b) We construct another FCD (blue surfaces) whose focal sets (yellow curves) lie in vertical planes, the ellipse in the mid-plane between two neighboring pyramids and the hyperbola bridging between the apices of the two pyramids. The new FCD, mirror symmetric through the plane of its ellipse, joins together the portions of spherical layers of the two pyramids. (c) We excise from the blue FCD all regions generated by the portions of the ellipse lying within the sample, as the yellow ellipse is not observed experimentally. (d) The sample is now divided into roughly pyramidal and tetrahedral cells by a scaffolding of the new FCDs’ focal sets (yellow curves). The inverted “pyramids” are filled with portions of spherical layers, concentric about the intersections of the yellow ellipses on the substrate, which math smoothly onto the blue FCDs of (c). (e) The entire structure for a single layer, composed only of portions of FCDs (red and blue surfaces) and portions of spheres (green and yellow surfaces).

4.3.5 Details of calculations

Numerically integrated free energy

All calculations for the free energy of a smectic layer configuration are taken relative to a reference state where all of the layers are horizontal planes with equal spacing. The free energy is a sum of three terms,

$$\Delta F = \Delta F_{\text{el}} + \Delta F_{\text{air}} + \Delta F_{\text{subs}}.$$

The first term is the elastic energy,

$$\Delta F_{\text{el}} = \int dV \left[2K_1 H^2 + \frac{1}{2} \bar{K} G \right],$$

where H is the layer mean curvature, G is the layer Gaussian curvature, and K_1 and \bar{K} are associated elastic moduli. The second term is the surface tension energy associated with the dimple-like deformation in the topmost layer,

$$\Delta F_{\text{air}} = \sigma_{\perp}^{\text{air}} \int dA \left[\sqrt{1 + (\nabla h)^2} - 1 \right],$$

where $\sigma_{\perp}^{\text{air}}$ is the surface tension associated with homeotropic anchoring at the air interface and $h(x, y)$ is the height function describing the topmost layer. The third term represents the preference for degenerate planar anchoring on the substrate. For the horizontal substrate surfaces on pillar top and between pillars, it has the form

$$\Delta F_{\text{subs}} = \Delta \sigma^{\text{subs}} \int dA \left[1 - (\hat{\rho} \cdot \hat{z})^2 \right],$$

where $\hat{\rho}$ is the smectic layer's unit normal vector at the substrate, \hat{z} is the unit vector in the vertical direction, and $\Delta\sigma^{\text{subs}} = \sigma_{\parallel}^{\text{subs}} - \sigma_{\perp}^{\text{subs}} < 0$ is the relative energy per unit area of degenerate planar vs. homeotropic anchoring. The anchoring potential is of the commonly used Rapini-Papoulier form. For the pillar side surfaces,

$$\Delta F_{\text{subs}} = \Delta\sigma^{\text{subs}} \int dA [-(\hat{\rho} \cdot \hat{\nu})^2],$$

where $\hat{\nu}$ is the unit normal vector on the pillar side. Numerical integration is performed using Mathematica 7.0 and 8.0. We make the assumption $\bar{K} = K_1$. (The choice of the value of \bar{K} turns out not to strongly affect the results so long as \bar{K} is on the same order as K_1). All other material constants are the same as in Sec. 4.2.

We now describe the calculation of each energy component in more detail. To calculate the elastic free energy, we use expressions for the curvature energy adapted from Kléman and Lavrentovich [67]:

$$\begin{aligned} \Delta F_{\text{el}} &= W_1 + W_2 \\ W_i &= W_{i,I} + W_{i,II}, \quad i = 1, 2 \\ W_{i,I} &= \int_0^{2\pi} du \int_0^{\arccos(\frac{a}{\Phi})} dt \int_{e \cos u + \rho_c}^{\sec t - \rho_c} d\rho \Theta(u, t, \rho) w_i(u, t, \rho) \\ W_{i,II} &= \int_0^{2\pi} du \int_{\arccos(\frac{a}{\Phi})}^T dt \int_{e \cos u + \rho_c}^{\frac{\Phi}{a} - \rho_c} d\rho \Theta(u, t, \rho) w_i(u, t, \rho) \\ w_1(u, t, \rho) &= -\frac{1}{2} K_1 (1 - e^2) a \frac{1}{(e \cos u - \rho)(1 - \rho \cos t)} \\ w_2(u, t, \rho) &= -\Lambda (1 - e^2) a \frac{\cos t}{(1 - e \cos u \cos t)^2}. \end{aligned}$$

Here, a is the focal conic domain semi major axis length; e is the FCD eccentricity, K_1 is the splay (mean curvature) elastic modulus, $\Lambda \equiv \bar{K} + 2K_1$, where \bar{K} is the Gaussian

curvature modulus; u parameterizes the elliptical focal curve; t parameterizes the hyperbolic focal curve; ρ parameterizes the layers, measuring distance in the layer normal direction divided by a ; Φ measures the maximum value of $\rho \times a$ at the air interface and is comparable to the LC thickness; T determines the t -value giving the point on the hyperbola that serves as the apex of the bounding cone; region I corresponds to generators that terminate on the hyperbola; region II corresponds to generators that terminate at the air interface; $\Theta(u, t, \rho)$ is a unit step function whose value is zero inside of the pillar (where there is no LC) and one outside of the pillar. Whereas Kléman and Lavrentovich [67] obtain an elegant analytic result for the integrated elastic free energy by assuming that the hyperbolic focal curve extends to infinity, here the nontrivial boundaries at the pillars and the air interface require us to compute ΔF_{el} numerically.

Because the boundary of the pillar is more naturally expressed in Cartesian coordinates than in the FCD coordinates (u, t, ρ) , we use the following transformation to calculate $\Theta(u, t, \rho)$ for an FCD with its hyperbola in the xz plane:

$$\begin{pmatrix} x \\ y \\ z \end{pmatrix} = \frac{1}{1 - e \cos u \cos t} \begin{pmatrix} \rho a(e - \cos u \cos t) + a(1 - e^2) \cos u \\ a\sqrt{1 - e^2} \sin u(1 - \rho \cos t) \\ a\sqrt{1 - e^2} \sin t(\rho - e \cos u) \end{pmatrix}. \quad (4.11)$$

To calculate ΔF_{air} , we use the area measure of the smectic layer at $\rho = \Phi/a$, again adapted from Ref. [67]:

$$\Delta F_{\text{air}} = \sigma_{\perp}^{\text{air}} a^2 (1 - e^2) \int_0^{2\pi} \int_{\arccos(\frac{a}{\Phi})}^T dt \left| \frac{(1 - (\frac{\Phi}{a}) \cos t) (e \cos u - (\frac{\Phi}{a}))}{(1 - e \cos u \cos t)^2} \right|. \quad (4.12)$$

To calculate the substrate interface energy ΔF_{subs} , we need the smectic layers' normal direction $\hat{\rho}$ as a function of x, y, z . In the region of the substrate that is enclosed

by the elliptical focal curve and outside of the pillar, $\hat{\rho}$ has no z -component, so the energy per unit area is simply $\Delta\sigma^{\text{subs}}$. However, for the pillar top and side surfaces, we are required to compute $\hat{\rho}$. In the FCD coordinates, we have the analytic expression

$$\hat{\rho}(u, t) = \begin{pmatrix} \hat{\rho}_x \\ \hat{\rho}_y \\ \hat{\rho}_z \end{pmatrix} = \frac{1}{1 - e \cos u \cos t} \begin{pmatrix} e - \cos u \cos t \\ -\sqrt{1 - e^2} \sin u \cos t \\ \sqrt{1 - e^2} \sin t \end{pmatrix}. \quad (4.13)$$

We then need (u, t) as functions of (x, y, z) , i.e., the inverse of transformation 4.11. Though no analytic relation for this transformation is available for arbitrary eccentricity e , at $e = 0$ (TFCD case), we can readily write

$$u = \arctan\left(\frac{y}{x}\right) \quad (4.14)$$

$$t = \arctan\left(\frac{z}{b - \sqrt{x^2 + y^2}}\right) \quad (4.15)$$

$$\phi \equiv b\rho = \sqrt{\left(b - \sqrt{x^2 + y^2}\right)^2 + z^2}, \quad (4.16)$$

where b is the domain radius. Remarkably, it has been shown that the FCD coordinates at arbitrary e are related to those of a TFCD by a Lorentz transformation [4]:

$$x' = \gamma(x - \beta\phi), \quad \phi' = \gamma(\phi - \beta x), \quad y' = y, \quad z' = z. \quad (4.17)$$

This transformation maps each point on a TFCD in the unprimed system to a corresponding point on an FCD of arbitrary eccentricity having the same values of u and t in the primed system. Here we make the identifications $\beta \equiv -e$, $\gamma \equiv (1 - \beta^2)^{-\frac{1}{2}}$, and $\phi' \equiv \rho'a$, where a is the semi major axis length in the primed system. The semi minor axis length $b = a\sqrt{1 - e^2}$ in the primed system equals the TFCD radius in the

unprimed system, so $\phi = \rho b$ as defined above. By substituting Eqn. 4.16 into the transformation 4.17, we obtain a quartic equation in x whose coefficients depend on (x', y', z') and e :

$$\begin{aligned} 0 = & [\gamma^{-4}]x^4 - [4x'\gamma^{-3}]x^3 \\ & + [4x'^2\gamma^{-2} + 2(x'^2y^{-2} - \beta^2(b^2 + y'^2 + z'^2))\gamma^{-2} - 4\beta^4b^2]x^2 \\ & - [4x'\gamma^{-1}(x'^2\gamma^{-2} - \beta^2(b^2 + y'^2 + z'^2))]x \\ & + [(x'^2\gamma^{-2} - \beta^2(b^2 + y'^2 + z'^2))^2 - 4\beta^4b^2y'^2]. \end{aligned} \quad (4.18)$$

Equation 4.18 is solved numerically for x , from which u and t are obtained via Equations 4.14 and 4.15. Finally, we can compute $\hat{\rho}(u, t)$ as in Eqn. 4.13 at the Cartesian coordinates (x', y', z') corresponding to the pillar boundaries.

For our geometric ansatz connecting the smectic layers between neighboring FCDs, the energetic contribution of the regions outside the FCDs is calculated from an explicit expression for the height of the topmost layer $h(x, y)$ constructed from a union of circular arcs as described above. The height function gives the topmost layer's principal curvatures k_1^0 and k_2^0 , reciprocal to radii of curvature R_1^0 and R_2^0 , as well as the unit normal direction $\hat{\rho}$. From each point (x, y) on the topmost layer, a generator is constructed by traveling downward along $\hat{\rho}$ until reaching the substrate, and the generator is parameterized by ϕ , which has units of length and equals zero at the topmost layer. Along the generator, the assumption of parallel layers implies that the principal radii of curvature are $R_i(\phi) = R_i^0 + \phi$ for $i = 1, 2$, and thus the area measure on a layer varies as

$$dA(\phi) = dx dy \sqrt{1 + (\nabla h)^2} \left(\frac{R_1^0 + \phi}{R_1^0} \right) \left(\frac{R_2^0 + \phi}{R_2^0} \right).$$

These expressions allow us to integrate the mean and Gaussian curvatures over ϕ along each generator, and then integrate over all generators parameterized by their values (x, y) at the air interface, weighted by the appropriate area measure. Implicit in these calculations is the assumption that no focal sets exist in the sample outside the FCDs. The contribution of ΔF_{air} is similarly calculated from $h(x, y)$ and the area measure. Additionally, the contribution of ΔF_{subs} on the horizontal substrate surfaces is calculated from $h(x, y)$ by finding the value ϕ^* of ϕ where a given generator intersects the substrate, setting $\hat{\rho} \cdot \hat{z} = [1 + (\nabla h)^2]^{-\frac{1}{2}}$, and integrating over generators using the area measure $dA(\phi^*)$. For the contribution to ΔF_{subs} on the pillar sides, we approximate the layer normal direction at (x, y, z) to be the same as the normal direction of the topmost layer at the same (x, y) , which is valid in the limit of slowly varying $h(x, y)$.

The ansatz requires us to choose a value of T , which marks the point on the hyperbola that serves as the apex of the FCD's bounding cone. Because the bounding cone apex is expected to be located above the LC/air interface, a lower bound for T is provided by $T_{\min} = \arccos(a/\Phi)$, corresponding to the termination of the hyperbolic focal curve at the air interface. An upper bound for T is provided by $T_{\max} = \arccos(c/a)$, which corresponds to the point on the imaginarily extended hyperbola positioned directly over the point on the ellipse at $u = 0$. If $T > T_{\max}$, then the layer normal would be vertical at some point within the FCD, which is not observed in the atomic force microscopy (AFM) data. Generally, we find that the choice of T in the interval $[T_{\min}, T_{\max}]$ has little effect on the calculation result or on agreement with the AFM data. We therefore choose $T = \frac{1}{2}(T_{\min} + T_{\max})$ for the results presented here.

Estimation of FCD eccentricity

The FCD eccentricity is estimated from the AFM data by the following procedure. First we recall the standard parameterization 4.11 for the FCD layers, where the plane of the hyperbolic focal curve is chosen to be the xz plane. We let $b = a\sqrt{1 - e^2}$, $c = \sqrt{a^2 - b^2} = ae$, and $\phi = \rho a$, while Φ equals the value of ϕ at the topmost layer. We also recall that $T_{\min} = \arccos(a/\Phi)$ is the value of t where the hyperbola terminates at the air interface. The hyperbola is given by $\vec{H}(t) = (c \sec t, 0, b \tan t)$. It follows that, for two FCDs with hyperbolic focal curves oriented toward each other, the distance between their ellipse foci (where the hyperbolae meet the xy plane at $t = 0$) is

$$d_f = \delta x + 2c(\sec T_{\min} - 1) = \delta x + 2c(\Phi/a - 1), \quad (4.19)$$

where δx is the horizontal distance between the two cusps in the AFM data.

Now consider the geometry observed in Fig. 4.14a, with four FCDs per pillar on a square array of pillars with circular cross-section. We assume that each FCD is tangent at four points to a square with one vertex at the center of the pillar, with side length equal to half of the center-to-center spacing W of nearest-neighbor pillars, and whose sides are aligned with the substrate patterning lattice directions (Fig. 4.20).

This geometry requires that

$$\sqrt{\frac{a^2 + b^2}{2}} = W/4.$$

Replacing b^2 with $a^2 - c^2$, we obtain the relation

$$a = \sqrt{\frac{1}{2} \left(\frac{W^2}{8} + c^2 \right)}. \quad (4.20)$$

The distance from the ellipse center to the ellipse focus is simply c . Furthermore, the

distance from the pillar center to the ellipse center is $\sqrt{a^2 + b^2} = \sqrt{2}W/4$. We thus obtain another expression for the distance between the ellipse foci of two FCDs facing each other,

$$d_f = 2 \left(\frac{\sqrt{2}W}{4} - c \right). \quad (4.21)$$

Equating the two expressions 4.19 and 4.21 for d_f yields

$$\Phi = \frac{a}{c} \left(\frac{\sqrt{2}W}{4} - \frac{\delta x}{2} \right). \quad (4.22)$$

To obtain an expression for the cusp angle α_c , as measured along the ellipse's major axis in the AFM data (Fig. 4.16d,h), we compute the two layer normal vectors

$$\partial_\phi \vec{X}|_{(u,t,\phi)=(0,\arccos(a/\Phi),\Phi)}, \quad \partial_\phi \vec{X}|_{(u,t,\phi)=(\pi,\arccos(a/\Phi),\Phi)},$$

normalize them, and equate their dot product to $\cos(\pi - \alpha_c) = -\cos \alpha_c$. The general form of the unit normal vector is

$$\hat{N} = \frac{\partial_\phi \vec{X}}{|\partial_\phi \vec{X}|} = \frac{(c - a \cos u \cos t, -b \sin u \cos t, b \sin t)}{a - c \cos u \cos t}.$$

After some algebraic simplification, we find

$$-\cos \alpha_c = \frac{\Phi^2 - a^2 - b^2}{\Phi^2 - c^2} = \frac{\Phi^2 - 2a^2 + c^2}{\Phi^2 - c^2}. \quad (4.23)$$

We substitute for a and Φ the functions of c given by Eqns. 4.20 and 4.22. The result is an equation relating c , α_c , δx , and W (implicitly through a). The latter three are measured quantitates from the AFM data. For the samples in Fig. 4.14a, we measure $\alpha_c \approx 147^\circ$, $\delta x \approx 4.8 \mu\text{m}$, and $W \approx 8.5 \mu\text{m}$. Using these values in Eqn. 4.23 gives

$c \approx 0.17 \mu\text{m}$, $a \approx 2.1 \mu\text{m}$, and $\Phi \approx 7.5 \mu\text{m}$. Dividing c by a gives the eccentricity, $e \approx 0.080$. The value of Φ obtained by this method is in good agreement with the liquid crystal thickness, $h \approx 7 \mu\text{m}$.

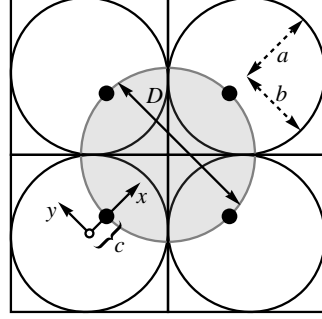


Figure 4.20: Schematic diagram of the FCD arrangement assumed for the pillar topography of Fig. 4.14a, viewed from above. The circular pillar, of diameter D , is represented in gray. The elliptical focal curves of four FCDs, assumed to lie in the plane of the substrate, are each tangent at four points to squares comprising one fourth of the unit cell. The solid black circles are the ellipse foci as well as the intersections of the hyperbolic focal curves with the plane; these lie at the pillar edge. The open circle is the center of one ellipse. The x - and y -axes of the coordinates used in Eqn. 4.11 are as shown in the diagram. From the Supporting Information to [51].

We can follow a similar calculation for the geometry in Fig. 4.14c. Here, we assume that each FCD is tangent to two neighbors, with both points of tangency lying along the major axis. The FCD semi major axis is then related to the diagonal center-to-center separation S of next-nearest-neighbor pillars by

$$a = S/4 \quad (4.24)$$

in place of Eqn. 4.20. Equation 4.21 is replaced with $d_f = 2(a - c)$. Equating this to the right side of Eqn. 4.19 gives

$$\Phi = \frac{a}{2c}(2a - \delta x) \quad (4.25)$$

in place of Eqn. 4.22. As before, Eqns. 4.24 and 4.25 are substituted into Eqn. 4.23, allowing us to solve for c . For the samples in Fig. 4.14c, we measure $\alpha_c \approx 163^\circ$, $\delta x \approx 4.7 \mu\text{m}$, and $S \approx 13.0 \mu\text{m}$. Using these values in Eqn. 4.23 gives $c \approx 0.13 \mu\text{m}$, $a \approx 3.3 \mu\text{m}$, and $\Phi \approx 22.0 \mu\text{m}$. Dividing c by a gives the eccentricity $e \approx 0.041$. Returning to the geometry of Fig. 4.14a, we consider the prediction of an alternative model for the interstices between FCDs, in which the spherical layers of Sethna and Kléman [115] fill the space between FCDs over the pillars. The cones bounding the FCDs around a given pillar all have a common apex above the pillar center, where the extensions of the four hyperbolic focal curves meet. Therefore, each bounding cone has in its interior a vertical generator line connecting the point on the ellipse at $u = 0$ to the point on the hyperbola directly above. Where this generator meets the topmost layer, the height profile in Fig. 4.16d would form a local maximum, with tangent passing through the horizontal. The distance δm between the two local maxima in Fig. 4.16d, which is at least as great as the width of the concave-up region, equals the minimum distance between ellipses on opposite sides of the pillar. Referring to the geometry of Fig. 4.20, this means

$$\frac{1}{2}\delta m = \frac{\sqrt{2}}{4}W - \sqrt{\frac{1}{2}\left(\frac{W^2}{8} + c^2\right)}.$$

Solving for $e = c/a$.

$$e = \frac{\sqrt{-\frac{1}{8} + 2\left(\frac{\delta m}{W} - \frac{\sqrt{2}}{4}\right)^2}}{\frac{\sqrt{2}}{4} - \frac{\delta m}{W}}.$$

Substituting $\delta m = 1 \mu\text{m}$ and $W = 8.5 \mu\text{m}$ gives $e \sim 0.75$.

4.3.6 Conclusion

In conclusion, we have shown that using micropillar arrays of variable dimension and geometry (height, shape, and spacing) as topographical templates, we can introduce hierarchical assembly of FCDs and tune their eccentricity in a SmA LC assembly. By decreasing the micropillar height, we observe a transition from confinement of isolated domains to the hierarchical growth of FCDs, tangent to their neighbors, with their hyperbolic focal lines pinned near the pillar edges. The size and shape of the pillars can be used to control the type of hierarchical FCD arrangement; the anisotropy of the pillar shape allows us to reliably predict the locations of FCDs relative to the substrate patterning due to the effective attraction of FCDs to pillar corners. The nontrivial, but apparently smooth, matching of smectic layers between neighboring FCDs on a nonuniform substrate presents an intriguing theoretical problem for which we have suggested a geometric ansatz. These topographic tools significantly enrich the library of possible FCD arrays, making it possible to create more complex 3D structured soft systems beyond trivial assembly.

4.4 Focal conic flower textures in smectic liquid crystals with curved boundaries

4.4.1 Introduction

A common theme in much research on self-assembly in LCs is the sensitive dependence of the assembly behavior on non-trivial boundary geometry, such as colloid shape [34, 44, 74, 114] and substrate topography [24, 51, 52, 62]. While the defects produced by anchoring on colloidal surfaces have been extensively studied in the nematic LC phase, relatively little is known about how smectic defects, including FCDs, assemble

in response to such inclusions, especially in confined geometries [12, 28, 80, 110, 113].

Even when not organized in a lattice, FCDs exhibit a high level of geometric organization as seen in the arrangement of their focal curve pairs, which are conjugate conic sections: an ellipse and a hyperbola (or two parabolae, a case that we will not study here). Typically, groups of FCDs spontaneously assemble into the so-called fan texture, with the hyperbolae all intersecting at a single point. Friedel [40], in a theory supplemented by later authors [16, 68, 75, 115], explained the fan texture by positing the *law of corresponding cones* (LCC), in which the smectic layers smoothly join together neighboring FCDs across conical boundary surfaces. These geometrical rules suggest a route to targeted assembly of FCDs with vastly increased sophistication as a result of nonzero eccentricity of the ellipse in the conjugate pair [51, 99, 142].

A supreme example of FCD self-organization with nonzero eccentricity is the “flower texture” in a smectic droplet reported in Ref. [87]. There, many FCDs pack with their ellipse long axes oriented radially from a common point P . However, the foci of the ellipses that are pierced by the hyperbolae, seen easily in bright field microscopy, are on the “far side” of the ellipse—unlike in the fan texture where the hyperbolae converge, in the flower they diverge away from P with no obvious intersection, apparently violating Friedel’s LCC.

In this section, we show that such packings of FCDs with diverging hyperbolae can be obtained by designing hybrid anchoring conditions such that one boundary is (approximately) a surface of revolution with negative slope in the radial outward direction. More generally, we demonstrate that curved interfaces provide a way to promote spatially varying FCD eccentricity, leading to complex patterns which could guide the assembly of technologically important materials, such as colloids, nanoparticles, and quantum dots, for novel metamaterials, sensors, optoelectronic devices, and solar cells [41, 79, 124, 133]. Further, thanks to the lensing properties of individual

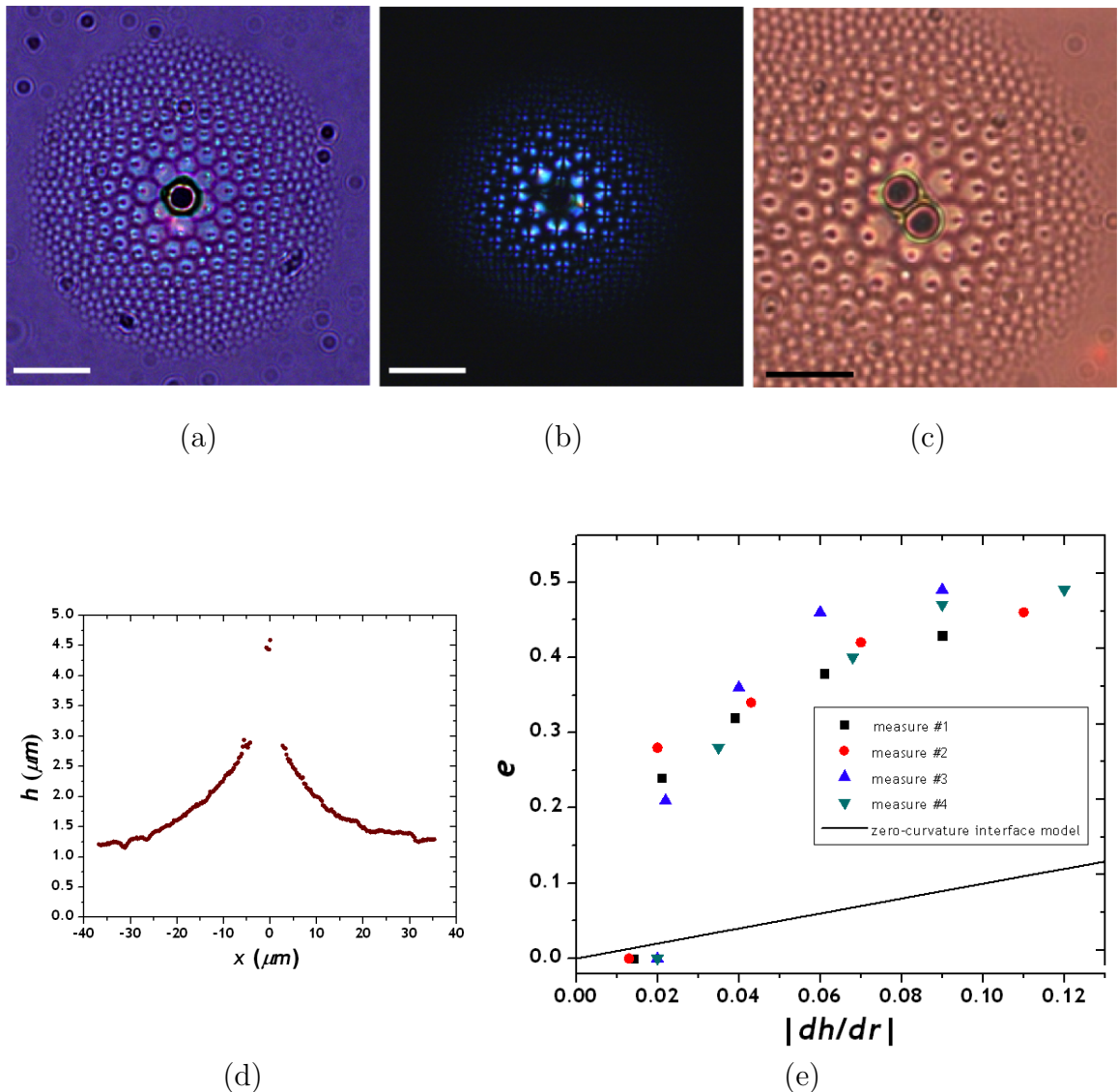


Figure 4.21: System A. (a-b) Smectic flower texture organized around a single colloid with homeotropic anchoring in response to the distortion of the LC-air interface produced by pinning at the colloid boundary. (a) Bright field. (b) Polarized optical microscopy. (c) Flower texture organized around a colloidal dimer. (d) Interferometric measurement of the LC-air interface profile around one colloid: smectic film thickness as a function of distance from the colloid center. (e) FCD eccentricity vs. magnitude of local slope of the smectic-air interface in the radial direction, measured above the middle of ellipses in four different radial directions. Solid line is the eccentricity given in Equation 4.26 corresponding to the limit of zero interfacial curvature. All scale bars are 10 μm . [10]

FCDs [61], arrays of FCDs organized radially as in the flower texture could efficiently focus light toward a central point, where the *virtual* (unphysical) branches of the hyperbolae intersect, for optical and photovoltaic applications.

We study two experimental examples of smectic flower textures obtained from different material systems. In System A (Fig. 4.21), the smectic-air interface is deformed by pinning at the boundary of a large colloidal inclusion, resulting in a flower texture with FCDs organized radially around the colloid. In System B, a SmA LC is placed on a substrate promoting degenerate planar anchoring, and the air interface, which imposes homeotropic anchoring, is partly replaced by a fluorosilane modified layer of SiO₂ nanoparticles that instead impose degenerate planar anchoring on the LC (Fig. 4.22a). The smectic layers tilt toward the boundary between the nanoparticle-covered and nanoparticle-depleted regions, and FCDs of varying eccentricity interpose between these tilted layers and the nanoparticle interface. In both systems, the key geometric feature is a mismatch in orientation between the interface with degenerate planar anchoring and the smectic layers at the opposite boundary. Finally, we provide a theoretical model applying the LCC to the flower texture. By geometrically constructing a “background texture” that approximates an arbitrary homeotropic interface profile, we show that FCDs of nonzero eccentricity can be smoothly embedded such that their hyperbolae extend radially outward, without violating the LCC.

4.4.2 Experimental results

In both System A and System B, smectic flower textures are observed in thin smectic films subjected to (effectively) hybrid anchoring conditions. Figure 4.21 shows an example of such a texture in System A, in which flower textures assemble around a large colloidal inclusion. The average smectic thickness is smaller than the critical

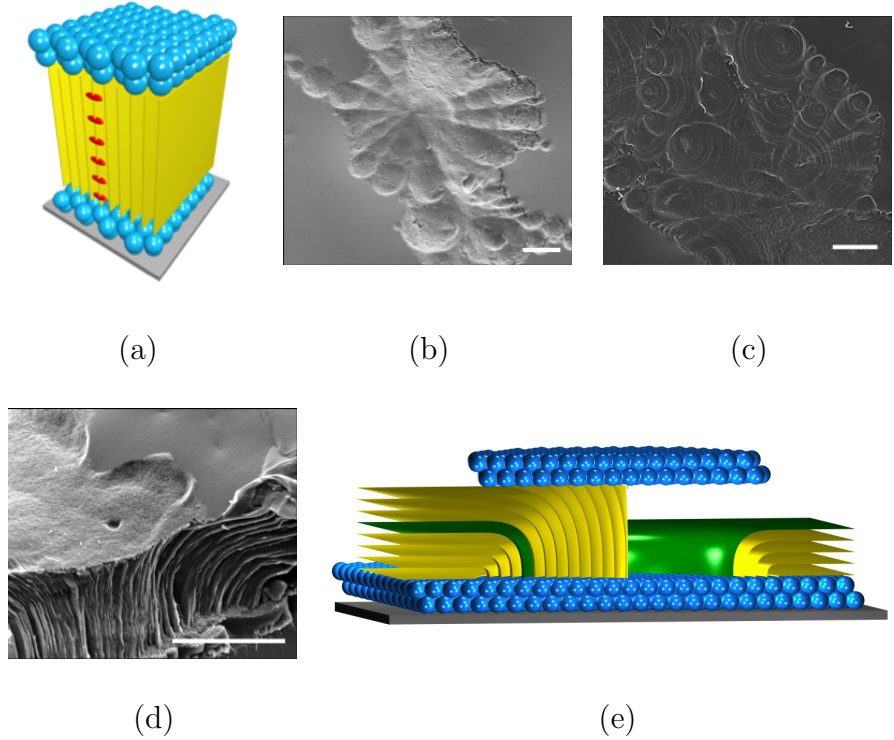


Figure 4.22: System B. (a) Schematic illustration of smectic phase (yellow layers, with representative rod-like molecules in red) between two interfaces covered with silica nanoparticles, shown in blue. (b) Smectic flower texture in a nanoparticle-covered region surrounded by a nanoparticle-depleted region. (c) A less equilibrated smectic flower texture. The smectic layer arrangement at the top interface is visible in the arrangement of the nanoparticles. (d) Cross-section of smectic liquid crystal at the boundary between a nanoparticle-covered region and a nanoparticle-depleted region. (e) Schematic illustration of the geometry of (d), with an arbitrarily chosen bent layer colored green to represent the analog of System A's curved homeotropic interface. All scale bars are $10 \mu\text{m}$. [10]

thickness h_c below which FCDs cost greater energy than homeotropically-aligned layers [62]. However, pinning of the LC-air interface at the colloid increases the thickness locally above h_c , so that FCDs form near the colloid. The film thickness, and thus the typical domain size, decrease with increasing distance from the colloid. Under bright field microscopy (Fig. 4.21a), the nonzero eccentricity of the FCDs is apparent both from the elongation of the ellipses and from the off-center dots marking the termination of the hyperbolae. As in Ref. [87], the hyperbolae are oriented radially outward from the center, in contrast to typical fan textures where the hyperbolae converge to a central point. This organization is confirmed by polarized optical microscopy (Fig. 4.21b), which reveals dark crosses shifted off of the ellipse centers away from the colloid. The interfacial deformation created by the colloid leads to capillary attraction between nearby colloids to minimize the excess free energy caused by the overlap of deformations in the LC-air interface. Figure (4.21c) shows a colloidal dimer with nearby FCDs.

Nonzero eccentricity is correlated with nonzero slope of the LC/air interface due to surface pinning at the colloid, which satisfies wetting conditions at particle surfaces as described by the Young equation [37]. The slope in the radial outward direction decreases from a maximum at the colloid to zero asymptotically, as shown in Fig. 4.21d, where the profile of the LC/air interface around the inclusion, measured using scanning white-light interferometry (SWLI), is represented. Accordingly, the FCDs nearest to the colloid have the highest eccentricity, while those far away have nearly zero eccentricity (Fig. 4.21e). Thus, FCD eccentricity is controlled by the orientation mismatch between the horizontal substrate, which imposes degenerate planar anchoring, and the locally tilted LC/air interface, which imposes homeotropic anchoring.

In addition to the substrate and air interfaces, we might expect that anchoring on the colloid would also affect FCD formation. However, when the colloids were treated with polyvinyl alcohol (PVA) to replace homeotropic anchoring with strong degenerate

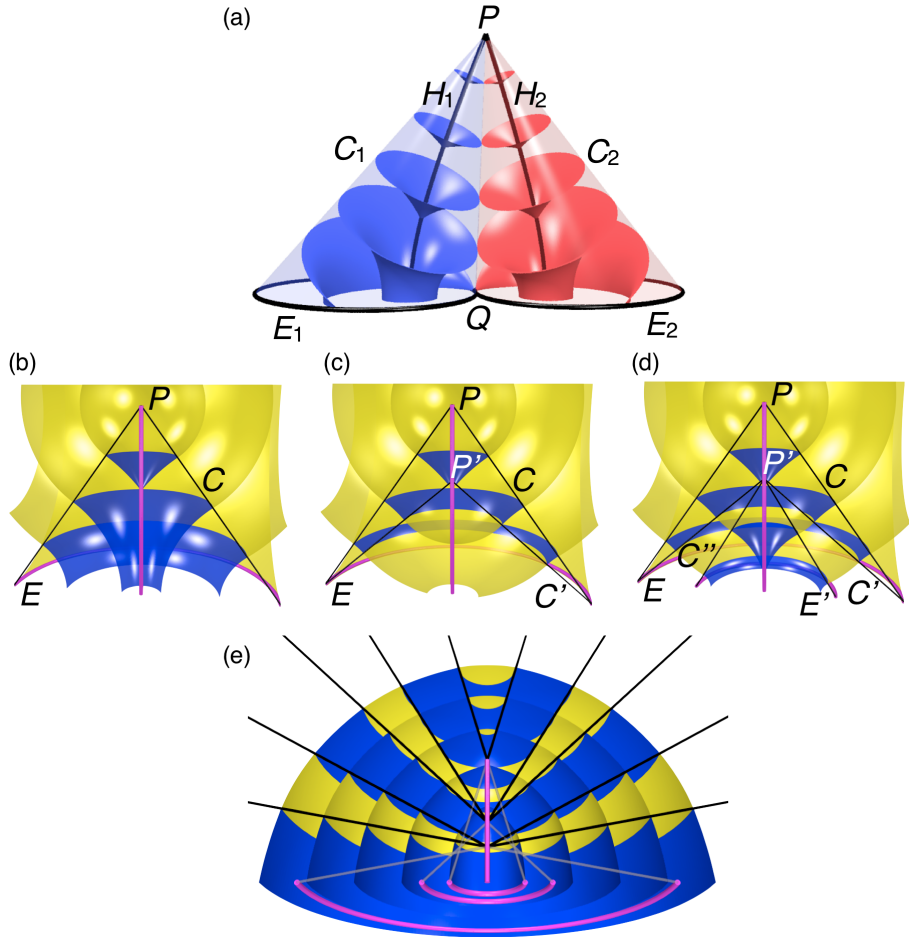


Figure 4.23: Geometric construction of a background texture. (a) The law of corresponding cones (LCC) in the traditional case of converging hyperbolae, with focal curves in black. (b-e) Construction of a complex background texture for the flower texture in accordance with the LCC. TFCDS are shown in blue, while concentric spherical regions are shown in yellow. Focal curves are shown in magenta. Black lines outline boundary cones between TFCDS and spheres. (b) One TFCD bounded by a right circular cone C with apex P and base E . (c) The TFCD now occupies the space between two cones C and C' , both containing the circular focal curve E but with different apices P, P' . Two different families of concentric spherical regions are centered at P, P' , respectively. (d) A smaller circle E' defines the base of a third cone C'' as well as the focal curve of a second TFCD bounded by this cone. (e) This construction works also with Type-II FCDs. Black lines outlining boundary cones are continued past the cone apex to the focal circles. [10]

planar anchoring on their surfaces, qualitatively similar flower textures were observed. We therefore conclude that the importance of the colloid in producing the flower texture lies in the colloid's wetting chemistry that deforms the LC-air interface, *not* the liquid crystalline anchoring on the colloid surface.

In System B, flowers textures also form in small planar-aligned islands covered by perfluorosilane treated SiO_2 nanoparticles surrounded by hybrid-aligned, nanoparticle-depleted regions, as shown in Figure 4.22b. Here, the elliptical focal curves are visible at the top interface; the hyperbolae extend downward. Figure 4.22c shows a less well-ordered flower texture, with striations in the nanoparticle arrangement revealing the arrangement of smectic layers. The ellipse focus of each FCD, where the hyperbola meets the LC-nanoparticle interface, is clearly visible as the center of a set of concentric circles in this plane. The hyperbolae are consistently oriented outward from the center of the planar-aligned region, toward the boundary with the hybrid aligned region.

The cause of the flower texture in this system is made clear by a cross-sectional scanning electron microscopy (SEM) image of the smectic layers (Fig. 4.22d). Layers in the planar-aligned region bend outward toward the hybrid-aligned region. Consequently, the layer geometry as viewed from above consists of a planar-anchoring horizontal surface at the top and what can be thought of as a tilted homeotropic surface below, created by the bent layers. This is the geometry that produced a flower texture in Fig. 4.21, only upside-down! To see this connection more clearly, we illustrate the geometry of System B schematically in Fig. 4.22e. There, an arbitrarily selected bent layer, colored green, conceptually plays the same role as the curved homeotropic interface of System A. A slight difference between the two experiments is that as distance from the center of the flower texture increases, the typical domain size increases in System B whereas it decreases in System A.

4.4.3 Geometric model

Can these flower textures be described by the law of corresponding cones? In Ref. [87], the authors suggest that the *virtual* branches of the hyperbolae meet at a common point above the center of the flower, rather than the physical hyperbolae as in fan textures under the LCC. We put forth a geometric construction that applies the LCC to hybrid-aligned smectics where the homeotropic interface is a surface of revolution, while the degenerate planar interface is flat. We then compare the predictions of this model to the data.

We begin by recalling that the law of corresponding cones describes how families of adjacent FCDs can be smoothly joined together by orienting such that their hyperbolic focal curves intersect at a common point, which also serves as the apex of a right circular cone containing the elliptical focal curve which bounds the FCD (Fig. 4.23a). Similarly, an FCD with bounding cone apex at P may be joined smoothly onto a family of concentric spheres centered at P (Fig. 4.23b) [115]. This is fortunate because concentric spheres, like FCDs, have a focal set of dimension less than two, avoiding energetically costly cusp wall defects.

In the case of tilt grain boundaries split into FCDs, the cone apex P is moved off to infinity along H so that in place of a “background” texture of concentric spheres, the FCD matches smoothly onto a background texture of planes whose normal direction matches the hyperbola’s asymptotic direction [68]. The bounding cone C has become a bounding cylinder.

Exactly the same reasoning would apply in a hybrid-aligned smectic if the homeotropic interface were a tilted plane, with the degenerate planar interface replacing the tilt grain boundary. Thus, if the homeotropic interface is gently curved, it is reasonable to expect the eccentricity to increase with the slope of the interface, which is indeed

the case as seen in Fig. 4.21. Quantitatively, however, the tilt grain boundary model disagrees with the FCD eccentricities e in our System A: For a (local) homeotropic interface slope of dh/dr , the formula given in Ref. [68] predicts

$$e^2 = \frac{(dh/dr)^2}{1 + (dh/dr)^2} \quad (4.26)$$

which does not fit our data (Fig. 4.21e). The curvature of the interface is therefore an important factor. But with a curved interface, what is the background geometry into which we are to imagine placing FCDs?

We construct such a background texture as follows. First consider a single toric FCD (TFCD), bounded by a right circular cone C with apex P , whose base E (the circular focal curve of the TFCD) has radius a . As already noted, the layers of the TFCD join smoothly onto a family of spheres concentric about P that exist outside of C (Fig 4.23b). But we can also bound a TFCD inside the space between two cones C and C' , with the same base but with different apices P and P' , respectively. Then, the TFCD also matches smoothly onto spherical layers concentric about P' that exist only inside of C' (Fig 4.23c). But once we have this second family of concentric spheres, it is straightforward to cut out from these spheres a cone C'' sharing the apex P' with C' but with circular base E' of radius $a' < a$, and then fill in this cone with a second TFCD (Fig 4.23d). We could continue in this fashion, dividing a region into arbitrarily many nested alternating concentric sphere families and TFCDs, separated by conical bounding surfaces that alternately share a common base or a common apex with the next cone. By construction, axial symmetry is preserved.

Now, by turning the picture upside down, we see that an arbitrary surface of revolution can be approximated by an outermost layer of this alternating set of TFCDs and concentric spheres (Fig. 4.24a). Thus, if the homeotropic interface is a surface of

revolution, this construction generates a smectic layer that approximates that surface, as well as a family of parallel, equally spaced layers below. If the homeotropic interface is planar at large radius, then the background TFCD of largest radius can be made to match smoothly onto planar layers by moving the apex of the largest bounding cone off to infinity, turning the cone into a cylinder. This is the case in Fig. 4.24. Finally, in each family of concentric spheres bounded between two cones with common apex P_i , we can place a ring of FCDs with nonzero eccentricity, all bounded by smaller cones with common apex at P_i (Fig. 4.24b). These FCDs obey the LCC and match smoothly onto the background texture. Furthermore, because the FCDs' bounding cones have apex below the degenerate planar interface rather than above the homeotropic interface, all of the hyperbolic focal curves will be oriented radially outward (Fig 4.24c)! The virtual branches of the hyperbolae, meanwhile, intersect at the common apex P_i below the center of the flower for all FCDs in the same ring. Thus the defining feature of the smectic flower texture can be brought into accordance with the LCC using this construction.

Note that there is no requirement that the circular focal curves sit at the same height, though we have made this choice in Figures 4.23 and 4.24 for simplicity. A reasonable, though not unique, alternative is to position each circle at the local center of curvature of the interface's profile. Also, an analogous geometric construction employs Type-II FCDs (Fig 4.23e), which produce an interface of purely positive Gaussian curvature [13, 14], i.e., the tilt angle increases with increasing radius. In this case, the picture does not need to be inverted to produce a flower texture, as the cones bounding the concentric spherical regions open upward in Fig 4.23e. Finally, we note that this model naturally extends a previous model for polygonal domains, in which the FCDs visible in the experiment are grouped inside background textures of concentric spheres, the various sphere families being glued together by portions of other FCDs whose

focal curves lie outside the sample [16, 75].

4.4.4 Comparison and discussion of theoretical and experimental results

Does this geometric construction describe the experimental results? While we have successfully captured the radial divergence of hyperbolic focal curves within the LCC, we pause to note some other implications of the model. First, while FCDs within each ring are tangent to their neighbors, the FCDs in different rings must have some space between their ellipses, where the background TFCD interposes between concentric sphere families. This gap is also present in the previously mentioned model for polygonal domains [16, 75]. While such a gap is not visible in the experimental images, it can be made small in the model by appropriate choices of bounding cones, to squeeze the background TFCDs into very small angles.

Second, a corollary of the previous point is that FCDs are predicted to pack within each ring but not to show any consistent organization from one ring to the next. This is plausibly consistent with the results in System A (Fig. 4.21), provided that the radius of the ring is given some leeway to vary so as to allow for compromise with the quasi-hexagonal packing of ellipses preferred by the degenerate planar substrate. However, System B appears to show FCDs grouped into radial wedges rather than concentric rings (Fig. 4.22), contrary to our expectation from the LCC. Instead, it is possible that each wedge of FCDs in System B has a background texture with no curvature in the azimuthal direction, this curvature being concentrated instead into small-angle tilt grain boundaries between neighboring wedges.

Thin-film smectics need not precisely obey the LCC because more general layer structures, other than spheres and FCDs, don't incur prohibitive energy penalties if

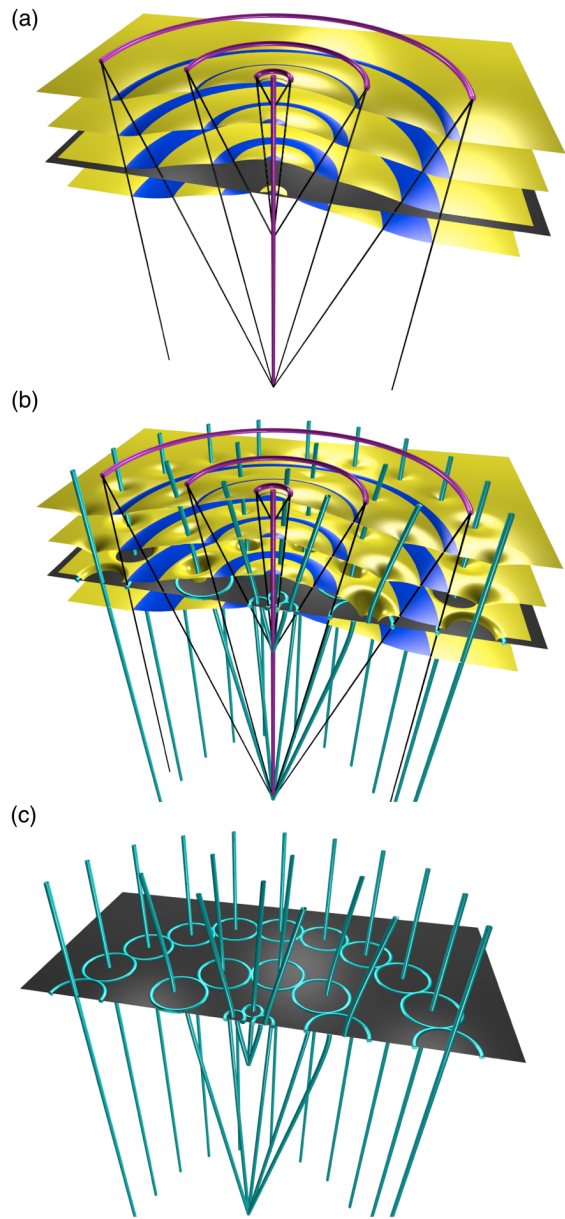


Figure 4.24: Flower texture in the LCC. (a) Background texture approximating a curved homeotropic interface and its parallel layers by alternating TFCDs (blue) and concentric spheres or planes (yellow). TFCD focal curves are in magenta. The gray plane, arbitrarily placed, schematically represents the degenerate planar interface, below which there is no smectic physically. (b) FCDs of radially varying eccentricity punctuate the concentric spherical and planar regions. The focal curves of these FCDs are shown in cyan. Focal hyperbolae are physical above the substrate and virtual below. (c) The focal curves of the smectic flower geometry in (b). [10]

they are generated by virtual focal sets lying outside the sample, i.e., their geometry does not require cusps in the smectic [51]. The model presented here demonstrates that the LCC is flexible enough to account for the basic features of the smectic flower but probably not capable of quantitatively describing the textures we observe.

4.4.5 Conclusion

We have demonstrated that control over the orientation mismatch between the hybrid aligning interfaces of a smectic thin film provides control over the FCD eccentricity and, thus, over complex patterns of self-organization in a liquid crystal. In particular, we have studied similar smectic flower textures produced in two different experiments: one in which the LC-air interface is curved by pinning at the surface of a colloidal inclusion, the other in which the boundary between a planar-aligned region covered by SiO_2 nanoparticles and a hybrid-aligned region exposed to air creates effective tilted hybrid anchoring. The radial outward orientation of the focal hyperbolae, unique to the flower texture, is deduced to arise from the outward tilt of the homeotropic interface's normal vector. We have extended previous LCC-based models by proposing a geometric model for hybrid-aligned smectics in the case that the homeotropic interface is a surface of revolution. The resulting nested system of background TFCDs and concentric spheres naturally allows for FCDs with their hyperbolae oriented radially outward, as in the flower texture. Comparing the implications of this model with the experimental results shows that the LCC can accommodate the arrangement of FCDs in a flower texture but does not describe the details of their packing behavior. The findings presented here will open the door to crafting highly sophisticated self-assembled patterns in smectic liquid crystals, for use in guiding functional materials such as colloids and nanoparticles into technologically useful arrangements, by clever preparation of the

boundaries.

Chapter 5

Conclusion

The assembly of defects in liquid crystals can be directed to a great extent by geometry of the boundaries, colloidal inclusions, and substrates, as we have demonstrated in several new and often surprising ways. In 3D nematic LCs, numerical modeling reveals that disclination loops cause anisotropic colloidal particles to change their orientations and interactions in ways sensitive to their shape parameters. The kinked disclination configurations lead to mirror-symmetric ground state colloidal orientations, snap-through disclination rearrangements, and tunable shape-dependent interparticle potentials, all of which may now be examined in experiment. Future numerical work in this area will include the study of 2D lattices of anisotropic colloidal particles and investigations of mixtures of different colloidal shapes. For nematics in micropost confining environments, we have found that disclination rings around microposts depend sensitively on the winding of the director field at the sharp corners where the micropost meets the substrate and air interfaces. The disclination ring, in turn, remotely guides the assembly of complex colloidal patterns at the air/LC interfaces through an elasticity-mediated attraction elucidated by the numerical modeling. A recurring theme in these results is the startling effects of sharp edges; one must exercise caution even when discussing topological charge due to the ambiguities that sharp edges introduce, but such edges can also be utilized for guiding disclinations along desired paths. It is possible that disclination “wires” with many turns and possibly

multistable configurations could be designed by this principle; similar ideas are being explored currently in the study of knots in nematic director fields [83, 84].

In 2D smectic liquid crystals, curvature of the substrate together with an imposed point disclination gives rise to a cusp grain-boundary line, and above a threshold curvature a pair of ± 1 -index point disclinations appears, as well. This generically complicated problem was studied in analytically tractable cases where the substrate is shaped as a cone, a plane, or intersections of the two types of objects. By concentrating the Gaussian curvature in points and lines, we gain insight not only into the defects we can expect in smectics on more general curved substrate shapes but also into the peculiar effects on smectic layers of sharp edges and conical points in the substrate—in other words, the relationship between defects in a metric and defects in a field defined on that space. It would be interesting to determine whether the strain induced in the smectic can in turn affect the shape of the substrate, which could have important implications for designing surfaces of programmable shape.

In 3D smectic liquid crystals, focal conic domains offer a route to self-assembled micropatterned functional materials, and we have demonstrated methods by which nontrivial boundary shape can guide FCD self-assembly into a number of otherwise inaccessible patterns. In the “confinement” regime, substrates topographically patterned with regular arrays of micropillars allow sensitive control over the size, spacing, and lattice symmetry of a regular array of toric focal conic domains. Patterning at the substrate controls the self-assembly through a relatively large bulk thickness, for reasons elucidated by analysis of the balance of bulk and surface energies. In a newly discovered “edge-pinning” regime, smaller micropillars direct FCDs into hierarchical assemblies with higher density and possibly different lattice symmetries than the substrate patterning. Our model of the smectic layer structure and accompanying energetic analysis suggest that tuning the relative size scales of micropillar arrays

offers a route to controlling not only FCD positions but also their eccentricities and nonuniform orientations. The latter goal is taken a step further in our work on the smectic flower texture, where curvature of the LC/air interface is shown to control the domain eccentricities and orientations in groupings of many FCDs in an unconventional radial pattern. There, we have shown that the dependence of FCD properties on boundary orientation mismatch is not purely a local problem, but instead forms a component of a sophisticated packing problem strongly constrained by the energetic preference for avoiding 2D tilt grain boundaries in the sample. Whereas the flower texture would at first seem to contradict the canonical law of corresponding cones, we have extended the LCC in an iterative fashion to capture the qualitative features of the flower texture, suggesting that the classical theory may still be used as a starting point for higher-order theories aiming to quantitatively predict the structure of such radial FCD assemblies, whose resemblance of insect eyes suggests novel optical applications [43].

All of these findings point to new principles for directing the spontaneous assembly of liquid crystalline defects into new and useful configurations. There is substantial room for extending these investigations into situations of greater complexity, both from an engineering standpoint through the study of new shape and size-scale combinations adapted for device interface, and from a physics perspective through the addition of chirality (of the liquid crystal and/or of the colloidal particles), applied electric or magnetic fields, and higher-genus topology, for example. By developing such an expanded toolkit for controlling defects, we hope to promote defects into building blocks and colloid-guiding tools for the self-assembly of new materials far more sophisticated than the liquid crystal phases on which they are based. Far from being unwanted obstructions to a homogenous ground state, liquid crystalline defects will, we hope, offer a route to new technological applications beyond electronic displays. As Robert

Browning put it when writing about something completely different, “So may a glory from defect arise” [18].

Appendix A

Relations between LdG elastic constants L_i and Frank elastic constants K_i

Here we find expressions for the Frank coefficients K_i in terms of the Landau-de Gennes coefficients L_j . We are now going to equate the distortion energy in the Landau-de Gennes theory (Equation 2.10),

$$f_d = \frac{L_1}{2}(\nabla \times \mathbf{Q} + 2q_0\mathbf{Q})^2 + \frac{L_2}{2}(\nabla \cdot \mathbf{Q})^2, \quad (\text{A.1})$$

to the free energy density of Frank elasticity,

$$f_{\text{Frank}} = \frac{K_1}{2}(\nabla \cdot \vec{n})^2 + \frac{K_2}{2}(\vec{n} \cdot (\nabla \times \vec{n}))^2 + \frac{K_3}{2}((\vec{n} \cdot \nabla) \vec{n})^2, \quad (\text{A.2})$$

where K_1 , K_2 , and K_3 are respectively the splay, twist, and bend elastic moduli. We work in the uniaxial limit, where

$$Q_{\alpha\beta} = \frac{3}{2}S(n_\alpha n_\beta - \frac{1}{3}\delta_{\alpha\beta}). \quad (\text{A.3})$$

In terms of \vec{n} , the L_1 term in Equation (A.1) becomes

$$\begin{aligned}
(\nabla \times \mathbf{Q} + 2q_0 \mathbf{Q})^2 &= [(\epsilon_{\alpha\beta\gamma} \partial_\beta Q_{\gamma\delta} + 2q_0 Q_{\alpha\delta}) (\epsilon_{\alpha\mu\nu} \partial_\mu Q_{\nu\delta} + 2q_0 Q_{\alpha\delta})] \\
&= \frac{9}{4} S^2 [\epsilon_{\alpha\beta\gamma} (n_\delta \partial_\beta n_\gamma + n_\gamma \partial_\beta n_\delta) + 2q_0 (n_\alpha n_\delta - \frac{1}{3} \delta_{\alpha\delta})] \\
&\quad \times [\epsilon_{\alpha\mu\nu} (n_\delta \partial_\mu n_\nu + n_\nu \partial_\mu n_\delta) + 2q_0 (n_\alpha n_\delta - \frac{1}{3} \delta_{\alpha\delta})] \\
&= \frac{9}{4} S^2 [\epsilon_{\alpha\beta\gamma} \epsilon_{\alpha\mu\nu} (n_\delta \partial_\beta n_\gamma + n_\gamma \partial_\beta n_\delta) (n_\delta \partial_\mu n_\nu + n_\nu \partial_\mu n_\delta) \\
&\quad + 4q_0 (\epsilon_{\alpha\beta\gamma} (n_\delta \partial_\beta n_\gamma + n_\gamma \partial_\beta n_\delta) (n_\alpha n_\delta - \frac{1}{3} \delta_{\alpha\delta})) \\
&\quad + 4q_0^2 (n_\alpha n_\alpha n_\delta n_\delta - \frac{2}{3} n_\alpha n_\delta \delta_{\alpha\delta} + \frac{1}{9} \delta_{\alpha\delta} \delta_{\alpha\delta})] \\
&= \frac{9}{4} S^2 [(\delta_{\beta\mu} \delta_{\gamma\nu} - \delta_{\beta\nu} \delta_{\gamma\mu}) (n_\delta \partial_\beta n_\gamma + n_\gamma \partial_\beta n_\delta) (n_\delta \partial_\mu n_\nu + n_\nu \partial_\mu n_\delta) \\
&\quad + 4q_0 ((\vec{n} \cdot \vec{n}) (\vec{n} \cdot (\nabla \times \vec{n})) - \frac{1}{2} \vec{n} \cdot (\vec{n} \times \nabla) (\vec{n} \cdot \vec{n}) \\
&\quad - \frac{1}{3} (\vec{n} \cdot (\nabla \times \vec{n}) + \epsilon_{\alpha\beta\gamma} n_\gamma \delta_\beta n_\alpha)) + 4q_0^2 (1 - \frac{2}{3} + \frac{1}{3})] \\
&= \frac{9}{4} S^2 [(n_\delta \partial_\beta n_\gamma + n_\gamma \partial_\beta n_\delta) (n_\delta \partial_\beta n_\gamma + n_\gamma \partial_\beta n_\delta) - (n_\delta \partial_\gamma n_\beta \\
&\quad + n_\beta \partial_\gamma n_\delta)) + 4q_0 (\frac{2}{3} \vec{n} \cdot (\nabla \times \vec{n}) - \frac{1}{3} \epsilon_{\alpha\beta\gamma} n_\gamma \delta_\beta n_\alpha) + \frac{8}{3} q_0^2] \\
&= \frac{9}{4} S^2 [2(\nabla \vec{n})^2 + 2 \cdot (\frac{1}{2} \nabla (\vec{n} \cdot \vec{n}))^2 - (\partial_\beta n_\gamma \partial_\gamma n_\beta) \\
&\quad - \frac{1}{2} n_\beta \partial_\beta n_\gamma \partial_\gamma (\vec{n} \cdot \vec{n}) - \frac{1}{2} n_\gamma \partial_\gamma n_\beta \partial_\beta (\vec{n} \cdot \vec{n}) - ((\vec{n} \cdot \nabla) \vec{n})^2 \\
&\quad + 4q_0 (\frac{2}{3} \vec{n} \cdot (\nabla \times \vec{n}) - \frac{1}{3} (\epsilon_{\alpha\beta\gamma} (\partial_\beta (n_\gamma n_\alpha)) - \vec{n} \cdot (\nabla \times \vec{n}))) + \frac{8}{3} q_0^2] \\
&= \frac{9}{4} S^2 [2(\nabla \times \vec{n})^2 + (\nabla \cdot \vec{n})^2 - ((\vec{n} \cdot \nabla) \vec{n})^2 \\
&\quad + 2q_0 (2\vec{n} \cdot (\nabla \times \vec{n}) + q_0) + \frac{2}{3} q_0^2]
\end{aligned}$$

Here and throughout, we use the convention of summation over repeated indices. We have made use of the fact that \vec{n} is a unit vector, so any derivative of $\vec{n} \cdot \vec{n}$ vanishes. In the last line, we have used the following:

$$(\nabla \vec{n})^2 = \partial_\alpha n_\beta \partial_\beta n_\alpha + (\nabla \times \vec{n})^2$$

$$\begin{aligned}
\partial_\alpha n_\beta \partial_\beta n_\alpha &= \partial_\alpha \partial_\beta (n_\beta n_\alpha) - \partial_\alpha n_\alpha \partial_\beta n_\beta - n_\alpha \partial_\alpha \partial_\beta n_\beta - n_\beta \partial_\alpha \partial_\beta n_\alpha \\
&= \partial_\alpha \partial_\beta (n_\beta n_\alpha) - \partial_\alpha n_\alpha \partial_\beta n_\beta - 2\partial_\alpha (n_\alpha \partial_\beta n_\beta) + 2\partial_\alpha n_\alpha \partial_\beta n_\beta \\
&= \partial_\alpha \partial_\beta (n_\beta n_\alpha) + (\nabla \cdot \vec{n})^2 \\
\Rightarrow 2(\nabla \vec{n})^2 - \partial_\alpha n_\beta \partial_\beta n_\alpha &= 2(\nabla \times \vec{n})^2 + (\nabla \cdot \vec{n})^2,
\end{aligned}$$

dropping a total derivative in the last line. Now recall that

$$(\nabla \times \vec{n})^2 = (\vec{n} \cdot (\nabla \times \vec{n}))^2 + (\vec{n} \times (\nabla \times \vec{n}))^2 = (\vec{n} \cdot (\nabla \times \vec{n}))^2 + ((\vec{n} \cdot \nabla) \vec{n})^2$$

since $\hat{\mathbf{v}} \times \nabla \times \hat{\mathbf{v}} = -(\hat{\mathbf{v}} \cdot \nabla) \hat{\mathbf{v}}$ for unit vectors $\hat{\mathbf{v}}$. Thus we obtain

$$(\nabla \times \mathbf{Q} + 2q_0 \mathbf{Q})^2 = \frac{9}{4} S^2 [(\nabla \cdot \vec{n})^2 + 2(\vec{n} \cdot (\nabla \times \vec{n}) + q_0)^2 + ((\vec{n} \cdot \nabla) \vec{n})^2 + \frac{2}{3} q_0^2].$$

The second term in f_d is easier.

$$\begin{aligned}
(\nabla \cdot \mathbf{Q})^2 &= \partial_\alpha Q_{\alpha\gamma} \partial_\beta Q_{\beta\gamma} \\
&= \frac{9}{4} S^2 [(\nabla \cdot \vec{n}) n_\gamma + (\vec{n} \cdot \nabla) n_\gamma] [(\nabla \cdot \vec{n}) n_\gamma + (\vec{n} \cdot \nabla) n_\gamma] \\
&= \frac{9}{4} S^2 [(\nabla \cdot \vec{n})^2 + ((\vec{n} \cdot \nabla) \vec{n})^2 + 2(\nabla \cdot \vec{n}) n_\gamma (\vec{n} \cdot \nabla) n_\gamma] \\
&= \frac{9}{4} S^2 [(\nabla \cdot \vec{n})^2 + ((\vec{n} \cdot \nabla) \vec{n})^2]
\end{aligned}$$

Therefore,

$$\begin{aligned}
f_d &= \frac{L_1}{2} (\nabla \times \mathbf{Q} + 2q_0 \mathbf{Q})^2 + \frac{L_2}{2} (\nabla \cdot \mathbf{Q})^2 \\
&= \frac{9}{8} S^2 [(L_1 + L_2)(\nabla \cdot \vec{n})^2 + 2L_1 (\vec{n} \cdot (\nabla \times \vec{n}) + q_0)^2 \\
&\quad + (L_1 + L_2)((\vec{n} \cdot \nabla) \vec{n})^2 + \frac{2}{3} L_1 q_0^2].
\end{aligned} \tag{A.4}$$

Comparing this to the Frank free energy density (A.2), we obtain result 2.12

$$K_1 = \frac{9}{4}S^2(L_1 + L_2), \quad K_2 = \frac{9}{2}S^2L_1, \quad K_3 = \frac{9}{4}S^2(L_1 + L_2). \quad (\text{A.5})$$

For the one-constant form of the LdG distortion energy, the uniaxial limit gives

$$\begin{aligned} f_d &= \frac{L_1}{2} \frac{\partial Q_{\alpha\beta}}{\partial x_i} \frac{\partial Q_{\alpha\beta}}{\partial x_i} \\ &= \frac{L_1}{2} \frac{9}{4} S^2 \left(n_\alpha \frac{\partial}{\partial x_i} n_\beta + n_\beta \frac{\partial}{\partial x_i} n_\alpha \right) \left(n_\alpha \frac{\partial}{\partial x_i} n_\beta + n_\beta \frac{\partial}{\partial x_i} n_\alpha \right) \\ &= \frac{9}{4} L_1 S^2 \left(\frac{\partial n_\alpha}{\partial x_i} \frac{\partial n_\alpha}{\partial x_i} \right) \end{aligned}$$

Comparing this to the equal-constants form of the Frank free energy, $f_{\text{Frank}} = \frac{K}{2} \frac{\partial n_\alpha}{\partial x_i} \frac{\partial n_\alpha}{\partial x_i}$, we see that $L_1 = (2/9)S^2K$.

For the three-constant form of the LdG distortion energy, the uniaxial limit gives

$$\begin{aligned} f_d &= \frac{1}{2} L_1 \frac{\partial Q_{ij}}{\partial x_k} \frac{\partial Q_{ij}}{\partial x_k} + \frac{1}{2} L_2 \frac{\partial Q_{ij}}{\partial x_j} \frac{\partial Q_{ik}}{\partial x_k} + \frac{1}{2} L_3 Q_{ij} \frac{\partial Q_{kl}}{\partial x_i} \frac{\partial Q_{kl}}{\partial x_j} \\ &= \frac{9S^2}{8} \left\{ 2L_1 \left[\frac{\partial n_\alpha}{\partial x_i} \frac{\partial n_\alpha}{\partial x_i} \right] + L_2 \left[(\nabla \cdot \vec{n})^2 + ((\vec{n} \cdot \nabla) \vec{n})^2 \right] \right. \\ &\quad \left. + 3SL_3 \left[((\vec{n} \cdot \nabla) \vec{n})^2 - \frac{1}{3} \left(\frac{\partial n_\alpha}{\partial x_i} \frac{\partial n_\alpha}{\partial x_i} \right) \right] \right\} \\ &= \frac{9S^2}{8} \left\{ (\nabla \cdot \vec{n})^2 [2L_1 + L_2 - SL_3] + (\vec{n} \cdot \nabla \times \vec{n})^2 [2L_1 - SL_3] \right. \\ &\quad \left. + ((\vec{n} \cdot \nabla) \vec{n})^2 [2L_1 + L_2 + 2SL_3] \right\} \end{aligned}$$

Equating this result to the Frank free energy density

$$f_{\text{Frank}} = \frac{1}{2} K_1 (\nabla \cdot \vec{n})^2 + \frac{1}{2} K_2 (\vec{n} \cdot \nabla \times \vec{n})^2 + \frac{1}{3} K_3 ((\vec{n} \cdot \nabla) \vec{n})^2,$$

we obtain $L_1 = (2/3)(-K_1 + 3K_2 + K_3)/9S^2$, $L_2 = 4(K_1 - K_2)/9S^2$, and $L_3 = 4(K_3 - K_1)/27S^3$.

Bibliography

- [1] M.-F. Achard, M. Kleman, Yu. A. Nastishin, and H.-T. Nguyen, The European Physical Journal E **16**, 37 (2005).
- [2] Ofer Aharony, Steven S. Gubser, Juan Maldacena, Hirosi Ooguri, and Yaron Oz, Physics Reports **323**, 183 (2000).
- [3] Gareth P. Alexander. *Liquid crystalline blue phases and swimmer hydrodynamics*. Ph.D. thesis, University of Oxford (2008).
- [4] Gareth P. Alexander, Bryan Gin-ge Chen, Elisabetta A. Matsumoto, and Randall D. Kamien, Physical Review Letters **104**, 257802 (2010).
- [5] Gareth P. Alexander, Bryan Gin-ge Chen, Elisabetta A. Matsumoto, and Randall D. Kamien, Reviews of Modern Physics **84**, 497 (2012).
- [6] Gareth P. Alexander, Randall Kamien, and Ricardo Mosna, Physical Review E **85**, 05070 (2012).
- [7] Gareth P. Alexander, Randall D. Kamien, and Christian D. Santangelo, Physical Review Letters **108**, 47802 (2012).
- [8] Hitesh Arora, Phong Du, Kwan W. Tan, Jerome K. Hyun, John Grazul, Huolin L. Xin, David A. Muller, Michael O. Thompson, and Ulrich Wiesner, Science **330**, 214 (2010).
- [9] A.R. Bausch, M.J. Bowick, A. Cacciuto, A.D. Dinsmore, M.F. Hsu, D.R. Nelson, M.G. Nikolaides, A. Travesset, and D.A. Weitz, Science **299**, 1716 (2003).

- [10] Daniel A. Beller, Mohamed A. Gharbi, Apiradee Honglawan, Kathleen J. Stebe, Shu Yang, and Randall D. Kamien, Physical Review X **3**, 041026 (2013).
- [11] Ion Bita, Joel K.W. Yang, Yeon Sik Jung, Caroline A. Ross, Edwin L. Thomas, and Karl K. Berggren, Science **321**, 939 (2008).
- [12] C. Blanc and M. Kleman, The European Physical Journal E **4**, 241 (2001).
- [13] Ph. Boltenhagen, O.D. Lavrentovich, and M. Kleman, Physical Review A **46**, R1743 (1992).
- [14] Yves Bouligand, Journal de Physique **33**, 525 (1972).
- [15] Mark J. Bowick, David R. Nelson, and Alex Travesset, Physical Review B **62**, 8738 (2000).
- [16] William Bragg, Nature **133**, 445 (1934).
- [17] Jeffrey M. Brake, Maren K. Daschner, Yan-Yeung Luk, and Nicholas L. Abbott, Science **302**, 2094 (2003).
- [18] Robert Browning, *The Works of Robert Browning* (Wordsworth Editions, 1994).
- [19] Marcello Cavallaro, Mohamed A. Gharbi, Daniel A. Beller, Simon Čopar, Zheng Shi, Tobias Baumgart, Shu Yang, Randall D. Kamien, and Kathleen J. Stebe, Proceedings of the National Academy of Sciences **110**, 18804 (2013).
- [20] Marcello Cavallaro, Jr., Lorenzo Botto, Eric P. Lewandowski, Marisa Wang, and Kathleen J. Stebe, Proceedings of the National Academy of Sciences **108**, 20923 (2011).

- [21] Marcello Cavallaro Jr., Mohamed A. Gharbi, Daniel A. Beller, Simon Čopar, Zheng Shi, Randall D. Kamien, Shu Yang, Tobias Baumgart, and Kathleen J. Stebe, *Soft Matter* **9**, 9099 (2013).
- [22] Paul M. Chaikin and Tom C. Lubensky, *Principles of condensed matter physics* volume 1. (Cambridge Univ Press, 2000).
- [23] Bryan Gin-ge Chen, Gareth P. Alexander, and Randall D. Kamien, *Proceedings of the National Academy of Sciences* **106**, 15577 (2009).
- [24] Myung Chul Choi, Thomas Pfohl, Zhiyu Wen, Youli Li, Mahn Won Kim, Jacob N. Israelachvili, and Cyrus R. Safinya, *Proceedings of the National Academy of Sciences* **101**, 17340 (2004).
- [25] Trirup Dutta Choudhury, Nandiraju V.S. Rao, Robert Tenent, Jeffrey Blackburn, Brian Gregg, and Ivan I. Smalyukh, *The Journal of Physical Chemistry B* **115**, 609 (2011).
- [26] Vivian P. Chuang, Jessica Gwyther, Rafal A. Mickiewicz, Ian Manners, and Caroline A. Ross, *Nano Letters* **9**, 4364 (2009).
- [27] Harry J. Coles and Mikhail N. Pivnenko, *Nature* **436**, 997 (2005).
- [28] Marjetka Conradi, Primož Ziherl, Andreja Šarlah, and Igor Muševič, *The European Physical Journal E* **20**, 231 (2006).
- [29] Simon Čopar and Slobodan Žumer, *Physical Review Letters* **106**, 177801 (2011).
- [30] P. G. de Gennes and J. Prost, *The Physics of Liquid Crystals* (Clarendon Press, 1993), second edition.

- [31] Erik D. Demaine, Martin L. Demaine, Duks Koschitz, and Tomohiro Tachi, *Graphics and Combinatorics* **27**, 377 (2011).
- [32] B.A. DiDonna and Randall D. Kamien, *Physical Review E* **68**, 041703 (2003).
- [33] B.A. DiDonna and R.D. Kamien, *Physical Review Letters* **89**, 215504 (2002).
- [34] Jayasri Dontabhaktuni, Miha Ravnik, and Slobodan Žumer, *Soft Matter* **8**, 1657 (2012).
- [35] Charles P. Dupin, *Applications de Géométrie et de Méchanique la Marine, aux Ponts et Chaussées, etc* (Bachelier, Paris, 1822).
- [36] Erik W. Edwards, Martha F. Montague, Harun H. Solak, Craig J. Hawker, and Paul F. Nealey, *Advanced Materials* **16**, 1315 (2004).
- [37] Jennifer Fiegel, Fang Jin, Justin Hanes, and Kathleen Stebe, *Journal of Colloid and Interface Science* **291**, 507 (2005).
- [38] Jean-Baptiste Fleury, David Pires, and Yves Galerne, *Physical Review Letters* **103**, 267801 (2009).
- [39] J.-B. Fournier and P. Galatola, *EPL (Europhysics Letters)* **72**, 403 (2005).
- [40] Georges Friedel, *Annales de Physique* **18**, 273 (1922).
- [41] Pedro D. García, Álvaro Blanco, Alexey Shavel, Nikolai Gaponik, Alexander Eychmüller, Benito Rodríguez-González, Luis M. Liz-Marzán, and Cefe López, *Advanced Materials* **18**, 2768 (2006).
- [42] D.J. Gardiner and H.J. Coles, *Journal of Physics D: Applied Physics* **39**, 4948 (2006).

- [43] Mohamed A. Gharbi, Daniel A. Beller, Apiradee Honglawan, Kathleen J. Stebe, Shu Yang, and Randall D. Kamien. SPIE Newsroom. Controlling liquid crystal defects. <http://spie.org/x106389.xml?pf=true&ArticleID=x106389> (2014).
- [44] Mohamed Amine Gharbi, Marcello Cavallaro Jr., Gaoxiang Wu, Daniel A. Beller, Randall D. Kamien, Shu Yang, and Kathleen J. Stebe, *Liquid Crystals* **40**, 1619 (2013).
- [45] Mohamed Amine Gharbi, Maurizio Nobili, Martin In, Guillaume Prévot, Paolo Galatola, Jean-Baptiste Fournier, and Christophe Blanc, *Soft Matter* **7**, 1467 (2011).
- [46] Mohamed Amine Gharbi, Maurizio Nobili, Martin In, Guillaume Prévot, Paolo Galatola, Jean-Baptiste Fournier, and Christophe Blanc, *Soft Matter* **7**, 1467 (2011).
- [47] Mohamed Amine Gharbi, David Seč, Teresa Lopez-Leon, Maurizio Nobili, Miha Ravnik, Slobodan Žumer, and Christophe Blanc, *Soft Matter* (2013).
- [48] Wei Guo and Christian Bahr, *Physical Review E* **79**, 011707 (2009).
- [49] Wei Guo, Stephan Herminghaus, and Christian Bahr, *Langmuir* **24**, 8174 (2008).
- [50] B.I. Halperin and David R. Nelson, *Physical Review Letters* **41**, 121 (1978).
- [51] A. Honglawan, D.A. Beller, M. Cavallaro, R.D. Kamien, K.J. Stebe, and S. Yang, *Proceedings of the National Academy of Sciences* **110**, 34 (2013).
- [52] Apiradee Honglawan, Daniel A. Beller, Marcello Cavallaro, Randall D. Kamien, Kathleen J. Stebe, and Shu Yang, *Advanced Materials* **23**, 5519 (2011).
- [53] F.R. Hung and S. Bale, *Molecular Simulation* **35**, 822 (2009).

- [54] Francisco R. Hung, Physical Review E **79**, 021705 (2009).
- [55] Klaus Jänich, Acta Applicandae Mathematica **8**, 65 (1987).
- [56] Lin Jia, Amin Cao, Daniel Lévy, Bing Xu, Pierre-Antoine Albouy, Xiangjun Xing, Mark J. Bowick, and Min-Hui Li, Soft Matter **5**, 3446 (2009).
- [57] Randall D. Kamien, David R. Nelson, Christian D. Santangelo, and Vincenzo Vitelli, Physical Review E **80**, 051703 (2009).
- [58] Daeseung Kang, Joseph E. Maclennan, Noel A. Clark, Anvar A. Zakhidov, and Ray H. Baughman, Physical Review Letters **86**, 4052 (2001).
- [59] Dong Ki Yoon, Rajdeep Deb, Dong Chen, Eva Körblova, Renfan Shao, Ken Ishikawa, Nandiraju V.S. Rao, David M. Walba, Ivan I. Smalyukh, and Noel A. Clark, Proceedings of the National Academy of Sciences **107**, 21311 (2010).
- [60] Sang Ouk Kim, Harun H. Solak, Mark P. Stoykovich, Nicola J. Ferrier, Juan J. de Pablo, and Paul F. Nealey, Nature **424**, 411 (2003).
- [61] Yun Ho Kim, Hyeon Su Jeong, Jung Hyun Kim, Eun Kyoung Yoon, Dong Ki Yoon, and Hee-Tae Jung, Journal of Materials Chemistry **20**, 6557 (2010).
- [62] Yun Ho Kim, Dong Ki Yoon, MC Choi, Hyeon Su Jeong, Mahn Won Kim, Oleg D. Lavrentovich, and Hee-Tae Jung, Langmuir **25**, 1685 (2009).
- [63] Yun Ho Kim, Dong Ki Yoon, Hyeon Su Jeong, and Hee-Tae Jung, Soft Matter **6**, 1426 (2010).
- [64] Yun Ho Kim, Dong Ki Yoon, Hyeon Su Jeong, Jung Hyun Kim, Eun Kyoung Yoon, and Hee-Tae Jung, Advanced Functional Materials **19**, 3008 (2009).

- [65] S.C. Kitson and A.D. Geisow, Molecular Crystals and Liquid Crystals **412**, 153 (2004).
- [66] Stephen Kitson and Adrian Geisow, Applied Physics Letters **80**, 3635 (2002).
- [67] M. Kleman and O.D. Lavrentovich, Physical Review E **61**, 1574 (2000).
- [68] M. Kleman and OD Lavrentovich, The European Physical Journal E: Soft Matter and Biological Physics **2**, 47 (2000).
- [69] Maurice Kléman, *Points, lines and walls: in liquid crystals, magnetic systems and various ordered media* (J. Wiley New York, 1983).
- [70] Maurice Kléman and Oleg D Laverntovich, *Soft matter physics: an introduction* (Springer, 2002).
- [71] Gary M. Koenig, I-Hsin Lin, and Nicholas L. Abbott, Proceedings of the National Academy of Sciences **107**, 3998 (2010).
- [72] John Michael Kosterlitz and David James Thouless, Journal of Physics C: Solid State Physics **6**, 1181 (1973).
- [73] Robert J. Lang, pages 98–105. (ACM, 1996) (1996).
- [74] Clayton P. Lapointe, Thomas G. Mason, and Ivan I. Smalyukh, Science **326**, 1083 (2009).
- [75] O.D. Lavrentovich, Sov. Phys. JETP **91**, 1666 (1986).
- [76] OD Lavrentovich and Yu A Nastishin, EPL (Europhysics Letters) **12**, 135 (1990).
- [77] Oleg D. Lavrentovich, Israel Lazo, and Oleg P. Pishnyak, Nature **467**, 947 (2010).
- [78] Baek-woon Lee and Noel A. Clark, Science **291**, 2576 (2001).

- [79] Seung-Wuk Lee, Chuanbin Mao, Christine E. Flynn, and Angela M. Belcher, *Science* **296**, 892 (2002).
- [80] G. Liao, I.I. Smalyukh, J.R. Kelly, O.D. Lavrentovich, and A. Jákli, *Physical Review E* **72**, 031704 (2005).
- [81] T.C. Lubensky, D. Pettey, N. Currier, and H. Stark, *Physical Review E* **57**, 610 (1998).
- [82] Chong Luo, Apala Majumdar, and Radek Erban, *Physical Review E* **85**, 061702 (2012).
- [83] Thomas Machon and Gareth P. Alexander, *Proceedings of the National Academy of Sciences* **110**, 14174 (2013).
- [84] Angel Martinez, Miha Ravnik, Brice Lucero, Rayshan Visvanathan, Slobodan Žumer, and Ivan I. Smalyukh, *Nature Materials* (2014).
- [85] L.J. Martínez-Miranda and Lynn K. Kurihara, *Journal of Applied Physics* **105**, 084305 (2009).
- [86] N. David Mermin, *Reviews of Modern Physics* **51**, 591 (1979).
- [87] C. Meyer, L. Le Cunff, M. Belloul, and G. Foyart, *Materials* **2**, 499 (2009).
- [88] Robert B. Meyer, *Philosophical Magazine* **27**, 405 (1973).
- [89] Jonathan Milette, Sabrina Relaix, Cyrille Lavigne, Violeta Toader, Stephen J. Cowling, Isabel M. Saez, R. Bruce Lennox, John W. Goodby, and Linda Reven, *Soft Matter* **8**, 6593 (2012).
- [90] Daigo Miyajima, Fumito Araoka, Hideo Takezoe, Jungeun Kim, Kenichi Kato, Masaki Takata, and Takuzo Aida, *Science* **336**, 209 (2012).

- [91] J.A. Moreno-Razo, E.J. Sambriski, N.L. Abbott, J.P. Hernandez-Ortiz, and J.J. de Pablo, *Nature* **485**, 86 (2012).
- [92] R.A. Mosna, D.A. Beller, and R.D. Kamien, *Physical Review E* **86**, 011707 (2012).
- [93] Nigel Mottram and Chris Newton. Introduction to Q-tensor theory. http://www.mathstat.strath.ac.uk/downloads/publications/introduction_to_q-tensor_theory.pdf (2004).
- [94] I. Muševič, M. Škarabot, U. Tkalec, M. Ravnik, and S. Žumer, *Science* **313**, 954 (2006).
- [95] David R. Nelson and B.I. Halperin, *Physical Review B* **19**, 2457 (1979).
- [96] A. Nych, U. Ognysta, M. Škarabot, M. Ravnik, S. Žumer, and I. Muševič, *Nature Communications* **4**, 1489 (2013).
- [97] A.B. Nych, U.M. Ognysta, V.M. Pergamenshchik, B.I. Lev, V.G. Nazarenko, I. Muševič, M. Škarabot, and O.D. Lavrentovich, *Physical Review Letters* **98**, 057801 (2007).
- [98] M. Oettel, A. Domínguez, M. Tasinkevych, and S. Dietrich, *The European Physical Journal E* **28**, 99 (2009).
- [99] Takuya Ohzono, Yoshiko Takenaka, and Jun-ichi Fukuda, *Soft Matter* **8**, 6438 (2012).
- [100] Mary O'Neill and Stephen M Kelly, *Advanced Materials* **15**, 1135 (2003).
- [101] Jeongman Park, T.C. Lubensky, and F.C. MacKintosh, *EPL (Europhysics Letters)* **20**, 279 (1992).

- [102] S.V. Pasechnik, V.G. Chigrinov, and D.V. Shmeliova, *Liquid crystals: viscous and elastic properties in theory and applications* (Wiley-VCH, 2009).
- [103] David Pires, Jean-Baptiste Fleury, and Yves Galerne, Physical Review Letters **98**, 247801 (2007).
- [104] Philippe Poulin, Holger Stark, T.C. Lubensky, and D.A. Weitz, Science **275**, 1770 (1997).
- [105] R. Pratibha, W. Park, and I.I. Smalyukh, Journal of Applied Physics **107**, 063511 (2010).
- [106] M. Ravnik, M. Škarabot, S. Žumer, U. Tkalec, I. Poberaj, D. Babič, N. Osterman, and I. Mušević, Physical Review Letters **99**, 247801 (2007).
- [107] Miha Ravnik, Gareth P. Alexander, Julia M. Yeomans, and Slobodan Žumer, Proceedings of the National Academy of Sciences **108**, 5188 (2011).
- [108] Miha Ravnik and Slobodan Žumer, Liquid Crystals **36**, 1201 (2009).
- [109] Mitya Reznikov, Bentley Wall, Mark A. Handschy, and Philip J. Bos, Journal of Applied Physics **104**, 044902 (2008).
- [110] C.D. Santangelo and Randall D. Kamien, Physical Review Letters **91**, 045506 (2003).
- [111] Christian D. Santangelo, Vincenzo Vitelli, Randall D. Kamien, and David R. Nelson, Physical Review Letters **99**, 017801 (2007).
- [112] Rachel A. Segalman, Hideaki Yokoyama, and Edward J. Kramer, Advanced Materials **13**, 1152 (2001).

- [113] P. Sens, M.S. Turner, and P. Pincus, Physical Review E **55**, 4394 (1997).
- [114] B. Senyuk, Q. Liu, S. He, R.D. Kamien, R.B. Kusner, T.C. Lubensky, and I.I. Smalyukh, Nature **493**, 200 (2012).
- [115] James P. Sethna and Maurice Kléman, Physical Review A **26**, 3037 (1982).
- [116] Jonathan Richard Shewchuk. An introduction to the conjugate gradient method without the agonizing pain. <http://www.cs.cmu.edu/~quake-papers/painless-conjugate-gradient.pdf> (1994).
- [117] Karen A. Simon, Erik A. Burton, Fei Cheng, Nisha Varghese, Eric R. Falcone, Lei Wu, and Yan-Yeung Luk, Chemistry of Materials **22**, 2434 (2010).
- [118] M. Škarabot, M. Ravnik, S. Žumer, U. Tkalec, I. Poberaj, D. Babič, N. Osterman, and I. Muševič, Physical Review E **77**, 031705 (2008).
- [119] Miha Škarabot, Miha Ravnik, Slobodan Žumer, Uroš Tkalec, Igor Poberaj, Dušan Babič, and Igor Muševič, Physical Review E **77**, 061706 (2008).
- [120] I.I. Smalyukh, S. Chernyshuk, B.I. Lev, A.B. Nych, U. Ognysta, V.G. Nazarenko, and O.D. Lavrentovich, Physical Review Letters **93**, 117801 (2004).
- [121] Ivan I. Smalyukh, Yves Lansac, Noel A. Clark, and Rahul P. Trivedi, Nature Materials **9**, 139 (2010).
- [122] Holger Stark. Physics of inhomogeneous nematic liquid crystals: Colloidal dispersions and multiple scattering of light. Habilitation thesis: University of Stuttgart (1999).
- [123] Holger Stark, Physics Reports **351**, 387 (2001).

- [124] Kathleen J. Stebe, Eric Lewandowski, and Moniraj Ghosh, *Science* **325**, 159 (2009).
- [125] Mark P. Stoykovich, Marcus Müller, Sang Ouk Kim, Harun H. Solak, Erik W. Edwards, Juan J. de Pablo, and Paul F. Nealey, *Science* **308**, 1442 (2005).
- [126] Chuanbing Tang, Joona Bang, Gila E. Stein, Glenn H. Fredrickson, Craig J. Hawker, Edward J. Kramer, Michael Sprung, and Jin Wang, *Macromolecules* **41**, 4328 (2008).
- [127] Chuanbing Tang, Erin M. Lennon, Glenn H. Fredrickson, Edward J. Kramer, and Craig J. Hawker, *Science* **322**, 429 (2008).
- [128] M. Tasinkevych, N.M. Silvestre, and M.M. Telo da Gama, *New Journal of Physics* **14**, 073030 (2012).
- [129] E.M. Terentjev, *Physical Review E* **51**, 1330 (1995).
- [130] D.J. Thouless, M. Kohmoto, M.P. Nightingale, and M. Den Nijs, *Physical Review Letters* **49**, 405 (1982).
- [131] U. Tkalec, M. Škarabot, and I. Muševič, *Soft Matter* **4**, 2402 (2008).
- [132] Uroš Tkalec, Miha Ravnik, Simon Čopar, Slobodan Žumer, and Igor Muševič, *Science* **333**, 62 (2011).
- [133] Tito Trindade, Paul O'Brien, and Nigel L Pickett, *Chemistry of Materials* **13**, 3843 (2001).
- [134] C. Tsakonas, A.J. Davidson, C.V. Brown, and N.J. Mottram, *Applied Physics Letters* **90**, 111913 (2007).

- [135] Vincenzo Vitelli, Julius B. Lucks, and David R. Nelson, Proceedings of the National Academy of Sciences **103**, 12323 (2006).
- [136] G. Wulff, Z. Kristallogr **34**, 449 (1901).
- [137] Xiangjun Xing, Journal of Statistical Physics **134**, 487 (2009).
- [138] D.K. Yoon, MC Choi, Y.H. Kim, M.W. Kim, O.D. Lavrentovich, and H.T. Jung, Nature Materials **6**, 866 (2007).
- [139] Dong Ki Yoon, Rajdeep Deb, Dong Chen, Eva Körblova, Renfan Shao, Ken Ishikawa, Nandiraju V.S. Rao, David M. Walba, Ivan I. Smalyukh, and Noel A. Clark, Proceedings of the National Academy of Sciences **107**, 21311 (2010).
- [140] Bruno Zappone and Emmanuelle Lacaze, Physical Review E **78**, 061704 (2008).
- [141] Bruno Zappone, Emmanuelle Lacaze, Habib Hayeb, Michel Goldmann, Nathalie Boudet, Philippe Barois, and Michel Alba, Soft Matter **7**, 1161 (2011).
- [142] Bruno Zappone, Claire Meyer, Leonardo Bruno, and Emmanuelle Lacaze, Soft Matter **8**, 4318 (2012).